LIGHTNING BEHAVIOR AS A DIAGNOSTIC TOOL TO QUANTIFY THE STRENGTH AND EVOLUTION OF PRECIPITATION PROCESSES DURING TROPICAL CONVECTIVE EVENTS OVER SOUTHEAST TEXAS

A Thesis

by

SYDNEY NICOLE BUTLER

Submitted to the Graduate and Professional School of
Texas A&M University
in partial fulfillment of the requirements for the degree of

MASTER OF SCIENCE

Chair of Committee,	Timothy Logan
Committee Members,	John Nielsen-Gammon
	Zhe Zhang
Head of Department,	Ramalingam Saravanan

May 2023

Major Subject: Atmospheric Sciences

ABSTRACT

Although Hurricanes Harvey (2017) and Nicholas (2021) both rapidly intensified before making landfall in the populous and highly convective region of southeast Texas, the tropical systems exhibited different lightning-precipitation characteristics. Given the inherent connection between lightning and precipitation, the utility of total lightning observations to diagnose the magnitude and evolution of precipitation processes during tropical convective events impacting southeast Texas is demonstrated. The continental outer rainbands of Harvey and the oceanic outer rainbands of Nicholas are studied for their lightning-precipitation microphysics using data from the Houston Lightning Mapping Array (HLMA) and the National Lightning Detection Network (NLDN) in synergy with radar, satellite, and other traditional products.

The behavior of the lightning activity discerned the state of the tropical convection and thus revealed how precipitation would occur, as electrified deep convective clouds feature brief periods of intense rainfall while less-electrified shallow clouds contain lower rainfall rates that are prolonged. Strengthening updrafts were also denoted by higher-altitude lightning and surges in flash rate. The peak flash extent and source densities were spatially correlated with the largest precipitation rates for the deep convection within Harvey and Nicholas, yet the shallow convection portrayed these maxima to be offset. There was a temporal lag between the highest flash and rainfall rates, with lightning (~300 fl min^{-1}) preceding precipitation (9 mm hr^{-1}) by 5.5 hours during Harvey and precipitation (6.5 mm hr^{-1}) preceding lightning (~28 fl min^{-1}) by 2.8

hours during Nicholas. The majority of lightning activity occurred after landfall during Harvey and before landfall during Nicholas. Lightning measurements collected during Harvey were about two orders of magnitude greater than those of Nicholas with maximum flash extent densities (fl km^{-2} min^{-1}) at ~900 versus ~14, largest VHF source densities (src km^{-1} $\{5\ min\}^{-1}$) at 56.7 versus 1.4, and highest VHF source rates (src $\{5\ min\}^{-1}$) at 177,472 versus 3,250. Harvey's continental convection was more powerful and organized than Nicholas's oceanic convection with widespread lightning-precipitation spatial and temporal coverage, inverted tripole charge layers located at higher heights, and larger Z_H (55-63 dBZ), Z_{DR} (> 1.5-2 dB), and K_{DP} (> 2.5-3 deg km^{-1}) values surpassing the melting level.

ACKNOWLEDGEMENTS

I would like to thank my committee chair, Dr. Logan, for his continuous guidance and support throughout the course of this research. He has always been around to answer my many questions, taken our research group to impromptu Pluckers trips for wings after productive days, and remained enthusiastic about the exciting results we have uncovered in this research.

Thank you to my committee members, Dr. Nielsen-Gammon and Dr. Zhang, for their counsel regarding my research. Special thanks to Dr. Nielsen-Gammon for his assistance with handling the HCFCD rain gauge data as well as providing a Python script to produce individual station files and storm total files.

Thanks also to Dr. Homeyer at the University of Oklahoma (Boomer Sooner!) for providing the GridRad radar files and to Ismael Cisneros at the HCFCD for supplying the rain gauge data from Hurricane Harvey.

Finally, thank you to my friends, colleagues, and family for their love and encouragement during graduate school, especially when times got tough. You helped me stay positive and kept my life fun!!

CONTRIBUTORS AND FUNDING SOURCES

Contributors

This work was supervised by a thesis committee consisting of Professor Timothy Logan, Professor John Nielsen-Gammon of the Department of Atmospheric Sciences, and Professor Zhe Zhang of the Department of Geography.

The open-source LMA analysis Python package known as “lmatools”, along with multiple scripts to manipulate the HLMA lightning data, was provided by Professor Eric Bruning from Texas Tech University.

All other work conducted for the thesis was completed by the student independently.

Funding Sources

This work was made possible in part by the National Oceanic and Atmospheric Administration (NOAA) under Grant Number NA16OAR4320115. Its contents are solely the responsibility of the author and do not necessarily represent the official views of NOAA.

NOMENCLATURE

CG	Cloud-to-ground
GPM	Global Precipitation Measurement
GridRad	Gridded NEXRAD WSR-88D Radar
HCFCD	Harris County Flood Control District
HLMA	Houston Lightning Mapping Array
IC	Intracloud
KDE	Kernel Density Estimation
LMA	Lightning Mapping Array
MUCAPE	Most Unstable Convective Available Potential Energy
NEXRAD	Next Generation Weather Radar
NIC	Non-Inductive Charging
NLDN	National Lightning Detection Network
RAP	Rapid Refresh
SHARPpy	Sounding and Hodograph Analysis and Research Program in Python
VHF	Very High Frequency
VLF	Very Low Frequency
WSR-88D	Weather Surveillance Radar – 1988 Doppler edition

TABLE OF CONTENTS

Page

LIST OF FIGURES

Page

LIST OF TABLES

Page

1. INTRODUCTION

1.1. Background and Motivation

Southeast Texas encompasses various urban and industrialized regions and attracts commercial and recreational interests from around the world. Specifically, the Houston metropolitan area is ranked as the fourth most populous in the United States and continues to grow. Additionally, the marine and petrochemical industries have a vast presence in southeast Texas because of its proximity to the Gulf of Mexico and abundance of land. For example, approximately 40% of the nation's petrochemical capacity is supplied by the network of over 400 refineries that span the region (Pan et al. 2020). Given that the Texas Gulf Coast is prone to several weather phenomena throughout the year including frontal passages, air mass thunderstorms, and tropical systems (Cullen 2013; Fridlind et al. 2019; Logan 2021; Orville et al. 2001), detrimental impacts on society and infrastructure can plague the area. Therefore, special attention should be paid to southeast Texas in an effort to not only investigate and analyze multiple types of convection, but also to minimize the risks associated with these potentially disastrous events.

In August 2017, Hurricane Harvey devastated southeast Texas with powerful winds, heavy flooding, and intense lightning activity. To illustrate, during the two-day period from 26 August to 27 August, over 700 mm of rainfall and nearly 300,000 lightning flashes were recorded by the Global Precipitation Measurement (GPM) satellite and the Houston Lightning Mapping Array (HLMA) network, respectively

(Logan 2021). The Houston metropolitan area has been characterized as a “hot spot” for lightning activity due to a combination of the enhanced convergence from the urban heat island effect and the altered microphysical processes spurred from anthropogenic pollution (Orville et al. 2001; Pan et al. 2020). Furthermore, Houston frequently suffers from flooding induced by tropical systems, which demands for the establishment of cost-effective disaster prevention, mitigation strategies, and emergency management measures including the availability of meteorological data at high spatiotemporal resolutions (Habibi et al. 2021). A climatological analysis of radar observations from the Houston/Galveston area (KHGX) revealed that convective initiation occurs in this region on roughly 40 to 55 percent of days year-round, with convective events strongly peaking during the months of June through September (Fridlind et al. 2019). As a result, the Department of Energy (DOE) funded Tracking Aerosol Convection interactions Experiment (TRACER) in conjunction with the National Science Foundation (NSF) funded Experiment in Sea Breeze Convection, Aerosols, Precipitation, and Environment (ESCAPE) research efforts commenced in October 2021 with the goal of acquiring more knowledge on cloud and aerosol interactions in deep convection over the populous yet polluted and highly convective environment of southeast Texas.

The established relationship between the mixed-phase microphysics, cloud kinematics, and storm electrification has prompted the exploration into the connection between lightning and precipitation. Lightning can serve as an indicator of intense convection because electrically-active deep convective clouds contain stronger turbulent updrafts that enable the production of higher precipitation ice content via mixed-phase

processes such as depositional growth, ice-ice collisions, and heterogeneous freezing (Carey and Rutledge 2000; Petersen and Rutledge 2001; Solorzano et al. 2018). The melting of ice particles will subsequently result in heavy rain at the surface, and therefore, a significant positive correlation between lightning frequency and convective precipitation should be expected (Xu et al. 2013). Xu et al. (2013) found that lightning frequency and flash rate aid in identifying clouds with convective cores. The study further revealed that storms with flash rates of 1 fl min^{-1} have a 95% probability of being associated with convective rainfall, while flash rates exceeding 5 fl min^{-1} denote heavily precipitating storms (> 40 dBZ radar reflectivity).

Strong evidence suggests that the predominant method for generating charge in thunderclouds is the non-inductive charging (NIC) mechanism, which features rebounding collisions between graupel and smaller ice crystals in the presence of supercooled liquid water (Saunders 1993; Takahashi 1978; Williams et al. 1991) found in the mixed-phase region of a storm updraft (0°C to -40°C). Both the magnitude and sign of the charge acquired by the particles are influenced by the temperature and supercooled liquid water content of the environment. In general, warmer/moist areas of the cloud tend to charge graupel positively and ice crystals negatively, while colder/drier areas of the cloud will reverse polarity and charge graupel negatively and ice crystals positively (Chmielewski et al. 2018; Fuchs and Rutledge 2018; Medina et al. 2021; Saunders 1993; Takahashi 1978; Williams et al. 1991). The storm-scale separation of charged particles is achieved through the force of gravity and updrafts, with the lighter ice crystals being transported to the upper levels of the cloud and the heavier graupel

particles falling to the mid-levels, forming the two main charge regions characterized by the mature stage of thunderstorms (Williams 1985). However, while charge structures are typically simplified as dipoles or tripoles, they can become quite complex as the storm undergoes different phases of development (Calhoun et al. 2013; Stolzenburg and Marshall 2008; Wiens et al. 2005; Zheng et al. 2019). As charge continues to build over time, the breakdown magnitude of the electric field is reached and lightning results (Ren et al. 2018; Schultz et al. 2009). It should be noted that while the electrification process outlined here applies only to deep convective clouds exhibiting cold rain processes, Saunders (1993) has proposed that warm clouds can also become electrified if the shallow convection is long-lived, which is a common feature within the feeder bands of tropical cyclones such as with the case of Hurricane Harvey (Brauer et al. 2020; DeMaria et al. 2012; Logan 2021).

Numerous lightning measurement platforms, including ground-based and space-based networks, have been developed to study the behavior of electrified storms. One of the earliest ground-based detection systems, the National Lightning Detection Network (NLDN), has been providing real-time data since the 1980s. The NLDN consists of over 100 sensors scattered throughout the United States that detect very low frequency (VLF) electromagnetic energy emitted through lightning discharges. The NLDN reports the time, location, polarity, and peak current of intracloud (IC) and cloud-to-ground (CG) lightning strikes (Cummins and Murphy 2009; DeMaria et al. 2012; Logan 2018; Pan et al. 2020; Wiens et al. 2005). Similarly, the Vaisala Global Lightning Dataset 360 (GLD360) measures VLF atmospheric radio signals (sferics) generated by lightning at

long ranges (~4000 km), allowing for information on CG strokes over the open ocean to be retrieved (Rudlosky et al. 2017; Stolz et al. 2014). Additional ground-based global lightning detection networks that discern VLF lightning sferics include the Earth Networks Total Lightning Network (ENTLN) and the World Wide Lightning Location Network (WWLLN; operated by the University of Washington). The key space-based detection platforms are the Geostationary Lightning Mapper (GLM) onboard the Geostationary Operational Environmental Satellite (GOES)-R, S, and T versions, and the Lightning Imaging Sensor (LIS) onboard the International Space Station (ISS), which both identify lightning flashes by their associated optical pulses but lack the ability to distinguish between CG and IC flashes (Blakeslee et al. 2020; Bruning et al. 2019). Lastly, lightning mapping arrays (LMAs), the more autonomous successor of the Lightning Detection and Ranging (LDAR) network (e.g., Koshak et al. 2007), involve ground-based stations that passively detect and group individual very high frequency (VHF; 60-66 MHz) electromagnetic pulses in 3D space and time (Chmielewski and Bruning 2016; Cullen 2013; Fuchs et al. 2016; Logan 2021; Rison et al. 1999; Thomas et al. 2004; Schultz et al. 2009; Wiens et al. 2005). LMAs have an advantage over the other networks because of their ability to essentially analyze total lightning and charge layers within electrified deep convective clouds in four dimensions.

Strong correlations among updraft volume, updraft mass flux, and flash rate have been observed (Calhoun et al. 2013; Carey and Rutledge 2000; DiGangi et al. 2016; Schultz et al. 2015; Wiens et al. 2005). Moreover, trends in lightning activity can provide evidence on the state of the updraft. In particular, periods of storm

intensification (e.g., increased updraft strength) are often marked by a simultaneous surge in lightning flash rate (Calhoun et al. 2013; DiGangi et al. 2016; Logan 2018; Wiens et al. 2005). The robustness of the updraft is further exemplified by higher-altitude lightning such as in the overshooting top, a common occurrence in supercell storms (Calhoun et al. 2013; DiGangi et al. 2016; Wiens et al. 2005).

Considering the association of lightning behavior with the strength of the mixed-phase updraft, it seems reasonable to suspect that lightning may be related to thunderstorm severity as well. Several studies have shown that rapid increases in total lightning activity (i.e., both IC and CG observations) occur tens of minutes prior to the onset of severe weather manifestation at the surface (e.g., Borque et al. 2020; Calhoun et al. 2013; Logan 2018; Schultz et al. 2009, 2015; Stano et al. 2014; Wiens et al. 2005; Williams et al. 1999). These abrupt surges in total flash rate, also termed "lightning jumps" (Williams et al. 1999), are precursors pertaining to all forms of severe weather. Williams et al. (1999), Calhoun et al. (2013), and Logan (2018) interpreted the updraft to be causal to both the remarkable lightning rates and the physical origin aloft of the severe weather at the ground. These studies observed explosive vertical development of the radar echo during the period of the dramatic jump in flash rates preceding events of hail, tornadoes, and severe wind. In addition, a tendency for the peak rainfall near the surface to lag the maximum lightning flash rate has been documented (Carey and Rutledge 2000; Logan 2021; Solimine et al. 2022). Carey and Rutledge (2000) attributed this lightning-precipitation temporal lag to the gravitational settling time of the precipitation mass from the electrified mixed-phase levels of the cloud to the surface.

In environments comprised of both stratiform and convective regimes (i.e., mesoscale convective systems and outer rainbands of tropical cyclones), the timing of the highest flash rates and extreme rainfall rates could be offset due to the longer amount of time it takes stratiform precipitation to develop (Logan 2021; Tian et al. 2020). After the deep convective regions heavily precipitate, the ice particles from the convective cores are detrained to the stratiform regions with depositional growth, which allows for these larger ice particles to fall into dry layers and eventually melt to raindrops that will serve as the stratiform precipitation (Tian et al. 2020). Given the utility of lightning observations in assessing storm intensification, total lightning data has been implemented into lightning jump algorithms to predict severe weather potential, which allows forecasters to provide more timely and accurate warnings in conjunction with other readily available observations such as radar, satellite, and environmental information (Schultz et al. 2009, 2015; Stano et al. 2014).

Since tropical precipitation systems (both hurricane and non-hurricane) are generally dominated by weaker, stratiform convection (Carey and Rutledge 2000; Cecil et al. 2002), lightning flash rates are generally small. However, lightning flash rates exceeding 5 fl min^{-1} have been detected in many tropical cyclones, especially in the outer rainband region that normally begins at a 150-200 km radius from the cyclone center (Cecil et al. 2002; Fierro et al. 2015; Hu et al. 2020; Solorzano et al. 2018). Cecil et al. (2002) analyzed radar reflectivity values, passive microwave ice scattering magnitudes, and total lightning data for 45 tropical events observed by the Tropical Rainfall Measuring Mission (TRMM) satellite and discovered that the lightning flash

densities, when normalized by the area occupied by convection, were greatest in the outer rainband region, yet these flash densities were still more than a factor of 10 less than continental flash densities. The study postulated that the heightened lightning activity in the outer rainbands could indicate that more supercooled liquid water droplets from the stronger updrafts are present compared to the eyewall region, inner rainband region, or elsewhere over the tropical oceans.

Fierro et al. (2015) inspected cloud microphysics simulations within a tropical environment resembling Hurricane Isaac (2012) along with total lightning observations from the ENTLN network. The study determined that there were larger radar reflectivities and deeper echo tops in the outer rainbands while the eyewall was mainly composed of stratiform regimes with smaller reflectivities and lower lightning activity. The inner rainband region has also been shown to rarely produce high enough reflectivities needed for intense convection and thus typically lacks electrified clouds (Cecil et al. 2002; DeHart and Bell 2020). Hu et al. (2020) examined the microphysical patterns of Hurricanes Harvey (2017) and Florence (2018) in both the outer rainband and eyewall regions through the combined usage of satellite products, radar retrievals, and LMA data. The results of the study allowed for the interpretation that the microphysical variability between the eyewall and outer rainbands is likely caused by the differences in the strength of the vertical wind shear. That is, strong vertical wind shear in the eyewall significantly weakens vertical motions and precipitation is dominated by warm-rain processes, while weak vertical wind shear in the outer rainbands favors deep convective development and initiates the mixed-phase precipitation processes needed for cloud

electrification. In terms of intensification, higher flash densities in the outer rainbands have consistently been a signal of strengthening tropical systems and increased flash densities in the eyewall denote weakening systems (e.g., DeMaria et al. 2012; Fierro et al. 2015; Stevenson et al. 2014; Xu et al. 2017).

The outer rainbands of tropical systems exhibit varying modes of convection throughout their lifetimes. Logan (2021) calculated a weak correlation coefficient (R-value) of 0.14 between the lightning flash and precipitation rates during Hurricane Harvey (2017) by utilizing LMA observations, radar reflectivity and dual-polarization products, and precipitation measurements. The study suggested that this likely stemmed from the feeder bands transitioning between deep and shallow convection. Deep convective systems (high lightning and heavy rainfall) have strong lightning-precipitation correlations while shallow convective systems (low lightning and heavy rainfall) display weak correlations (Carey and Rutledge 2000; Solimine et al. 2022; Tapia et al. 1998; Xu et al. 2013). DeHart and Bell (2020) explored the intermittent nature of the extreme precipitation associated with Hurricanes Harvey (2017) and Florence (2018) by looking at polarimetric radar and rain gauge data and revealed that the outer rainbands of both hurricanes featured diverse microphysics spatially and temporally coincident with embedded deep convection within broader stratiform convection. Yang et al. (2019) also studied Hurricane Harvey's extraordinary rainfall through the synchronous use of polarimetric radar observations, high-resolution Weather Research and Forecasting (WRF) model simulations, and rain gauge measurements over Harris County, Texas. The study further confirmed that the heavy precipitation during

Hurricane Harvey was closely tied to the structure and evolution of the outer rainbands that portrayed large spatial variability. Observational studies have shown that the azimuthal distribution of convection within tropical cyclones is greatly influenced by the direction and magnitude of the deep-layer (850-200 mb) environmental vertical wind shear as well as storm motion. Convective rainfall and lightning activity are most prevalent in the downshear right quadrant for the outer rainbands and in the downshear left quadrant for the eyewall under moderate-to-strong shear regimes (Chen et al. 2006; Corbosiero and Molinari 2002, 2003; Didlake and Kumjian 2017; Homeyer et al. 2021; Rogers et al. 2003; Stevenson et al. 2015; Yang et al. 2019).

Few studies have investigated transitional continental/marine convective environments by utilizing total lightning observations synergistically with radar, satellite, and other ancillary products to examine microphysical processes in rainfall and lightning activity within the outer rainbands. This research presents a unique opportunity of evaluating the lightning-precipitation relationship in tropical cyclones that have passed directly within the confines of a lightning mapping array which can provide not only total lightning data but information about charge layer location and height as well. Therefore, the proposed study builds upon the methods of Logan (2021) and takes a more detailed, real-time approach with the goal of demonstrating how lightning behavior can help diagnose the magnitude and evolution of precipitation processes during tropical convective events in southeast Texas. The following scientific questions will be addressed:

1. How can lightning activity obtained from the HLMA quantify the strength and evolution of tropical convection with respect to its flooding potential?
2. What is the relationship between lightning and precipitation during the two selected tropical convective events (i.e., Harvey (2017) and Nicholas (2021)) in southeast Texas?
3. How does the lightning-precipitation behavior differ between tropical continental convection and tropical oceanic convection?

The outer rainbands of two tropical cyclones (Harvey and Nicholas) that caused significant precipitation amounts and flooding in southeast Texas will be examined using total lightning data combined with other traditional methods to determine the association of lightning and precipitation throughout the storm's progression. The microphysical trends in the continental feeder bands of Hurricane Harvey will be further compared to the microphysical tendencies of the oceanic feeder bands of Hurricane Nicholas. Ideally, the newly acquired knowledge on the link between lightning and precipitation in tropical cyclones can enable forecasters to track these storms more efficiently, and thus provide an earlier indication of intense rainfall potential.

1.2. Hypotheses

The following hypotheses will be tested in this study:

1. Lightning behavior can serve as a diagnostic tool to quantify the strength and evolution of tropical convection with respect to its potential for extreme precipitation and flooding.
2. There are discernable spatial and temporal relationships between lightning and precipitation in tropical cyclones that have impacted southeast Texas.
3. The oceanic tropical convection in Hurricane Nicholas will be comparatively weaker in terms of lightning and precipitation than the continental tropical convection in Hurricane Harvey.

2. DATA AND METHODS

2.1. Houston Lightning Mapping Array (HLMA)

Total lightning data can give insight into storm charge structure and provide rapid temporal updates on changes in a thunderstorm's updraft at sub-radar volume-scan times (Calhoun et al. 2013; Stano et al. 2014). The Houston Lightning Mapping Array (HLMA) is a three-dimensional (3D) total lightning mapping system surrounding the Houston metropolitan area that detects the impulses of radiation that are emitted during the breakdown and channel propagation process in electrified storms (Cullen 2013). Established in April 2012, the self-sufficient HLMA sensors were installed at the same sites and operated at the same unused television channel frequency of 60 to 66 MHz as its predecessor the Lightning Detection and Ranging (LDAR)-II network (Cullen 2013). The sensors are designed to be operated independently in that wired power or internet connection are not required. The HLMA network is currently composed of ten active sensors that encompass southeast Texas, with two additional sensors on loan from Texas Tech University (PI Dr. Eric Bruning) located in Winnie and Angleton (Figure 1; Table 1). The additional sensors were temporarily installed for the research purposes of the TRACER/ESCAPE field campaigns. Note that Houston is the center of the HLMA network with nearly 100% 3D detection efficiency of anything within 100 km of Houston, which creates the 100-km radius circle of detection in Figure 1.

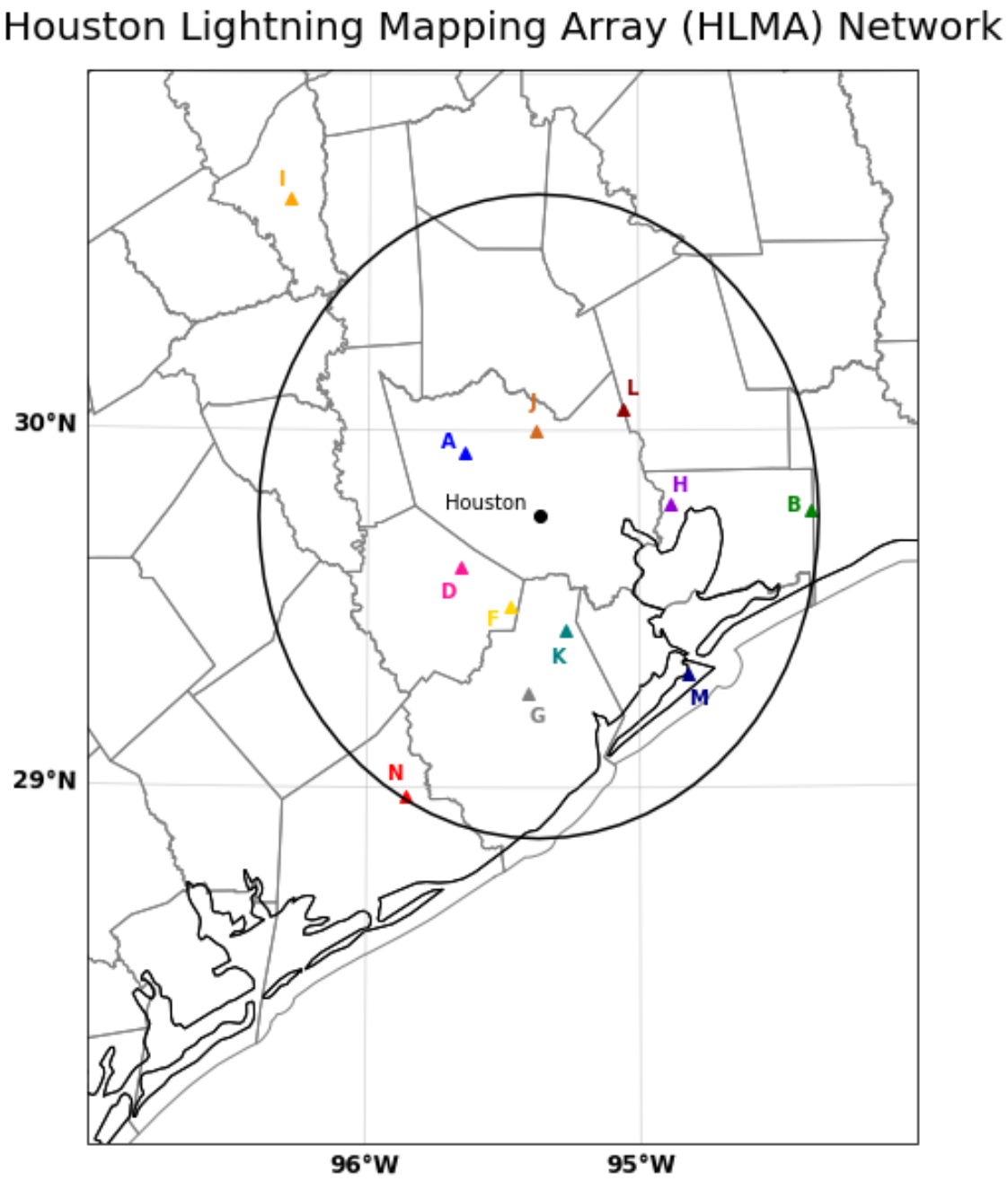

Figure 1: Map of sensors in the HLMA network.

Station	Location	Latitude	Longitude
A	Cy-Fair ISD (Cypress, TX)	29.939	-95.646
B	Winnie (ESCAPE sensor)	29.772	-94.367
D	Sugar Land Regional Airport (Sugar Land, TX)	29.619	-95.658
N	Bay City Regional Airport (Bay City, TX)	28.974	-95.861
F	Houston Southwest Airport (Arcola, TX)	29.505	-95.476
G	Angleton (ESCAPE sensor)	29.262	-95.413
H	Royal Purple Raceway (Baytown, TX)	29.791	-94.883

I	Texas A&M University (College Station, TX)	30.646	-96.298
J	Lone Star College-North Harris (Houston, TX)	30.002	-95.384
K	Alvin ISD (Alvin, TX)	29.441	-95.273
L	May Community Center (Huffman, TX)	30.058	-95.061
M	Texas A&M-Galveston (Galveston, TX)	29.316	-94.822

Table 1: List of each HLMA sensor station with each of its respective location, latitude, and longitude.

Similar to other LMA networks, the HLMA utilizes technology developed by New Mexico Tech featuring a global positioning system (GPS) that utilizes a time-of-arrival (TOA) technique to measure the time at which a very high frequency (VHF) electromagnetic signal produced by a developing lightning channel arrives at each station, enabling the latitude, longitude, altitude, and time of origin of the VHF source to be computed through a system of equations (Cullen 2013; Rison et al. 1999; Thomas et

al. 2004). For this study, VHF sources that had reduced chi-squared values greater than 1, had fewer than 6 contributing stations, or had source heights above 20 km were excluded to reduce noise and maintain a reliable dataset. The detection efficiency and data quality decrease at a proportion to the inverse square of the range (Cullen 2013), so only the most powerful sources can be detected at the edge of the range of detection. Although Hurricane Nicholas's sources were located outside the 100-km radius circle of detection, these lightning observations were still meaningful with at least 95% detection efficiency (Logan 2021).

The HLMA sources can be resolved into flashes and flash extent by using flash-clustering algorithms outlined in the Bruning (2013), DiGangi et al. (2016), Fuchs et al. (2015, 2016), Fuchs and Rutledge (2018), and Ren et al. (2018) studies. The algorithm, which is integrated into an open-source LMA analysis package known as "lmatools" (Bruning 2013), applies spatial and temporal criteria (3 km and 150 ms) between adjoining source points to group each of the VHF sources into a given flash with at least 10 sources required per flash. Supplementary products, such as flash extent density and flash rate, are further derived by the script and projected onto a two-dimensional grid. Note that these products can be utilized to delineate between different modes of convection, as the inverse flash rate-extent relationship hypothesizes that the regions of the storm with the highest (lowest) flash rates and smallest (largest) flash extents portray the strongest, most turbulent (weakest) updrafts (Calhoun et al. 2013; Logan 2021; Fuchs and Rutledge 2018; Schultz et al. 2015). Although the spatial resolution (0.0103° × 0.0103°) and 1-min temporal resolution of the flash products supplied by "lmatools"

algorithm differ from the other datasets in this study, the lightning data were scaled accordingly for the direct comparison to radar and precipitation variables in space and time. The lightning data were also filtered to only contain the sources within the rainbands of focus through the use of the IDL (Interactive Data Language) xlma program's "Polygon" tool to limit the data selection to within the polygon drawn. Only sources over land and only sources over ocean were included for Hurricane Harvey and Hurricane Nicholas, respectively.

Using the inferred charge identification technique (e.g., Calhoun et al. 2013; Chmielewksi et al. 2018; Cullen 2013; Fuchs and Rutledge 2018; Wiens et al. 2005), the crude vertical charge structure of each storm from the spatiotemporal distribution of HLMA sources contained within the individual lightning flashes was analyzed. This method follows from the bidirectional lightning propagation model (Kasemir 1960; Mazur and Ruhnke 1993), which states that lightning is initiated between regions of strong opposite charge and subsequently propagates into regions of opposite charge with the negative (positive) leader traveling toward and through regions of positive (negative) charge in order to neutralize charge buildup. Rison et al. (1999) demonstrated that negative polarity breakdown (i.e., negative leaders) is inherently noisier than positive leaders at the radio frequencies used by LMA, resulting in negative leaders producing more VHF radiation than positive leaders. In essence, since negative (positive) leaders propagate into positive (negative) charge regions, the positive charge region is more illuminated than the negative charge region. Therefore, this asymmetry is beneficial when viewing source animations to deduce charge polarity on a flash-by-flash basis by

classifying the first several LMA sources and highest VHF source density areas as positive charge. While most thunderstorms possess a “normal” tripole charge structure (i.e., negative charge at mid-levels situated between regions of upper and lower positive charge), some storms exhibit “inverted” or “anomalous” charge structures characterized by positive charge at the mid-levels surrounded by regions of upper and lower negative charge (Fuchs et al. 2015; Fuchs and Rutledge 2018; Wiens et al. 2005). Only the largest (or “big”) flashes were examined for each tropical cyclone. The criteria for a big flash versus a medium flash differed for each tropical cyclone case. That is, Hurricane Harvey had higher big/medium flash thresholds ranging from 75-1000 source points, while Hurricane Nicholas had a lower big/medium flash threshold of 75 source points due to less frequent lightning activity overall.

Lightning data from the National Lightning Detection Network (NLDN) were used in combination with the HLMA observations to determine what fraction of the total flash count were intracloud (IC) or cloud-to-ground (CG) flashes, as well as the location, polarity, and peak current of each flash. CG strokes with an absolute value of 10 kA for peak current threshold were not used in this study because they can often be mistaken for IC lightning. The NLDN detects over 95% of CG flashes with a median location accuracy of 250 m or better over the contiguous United States. Moreover, NLDN data are merely point measurements and the three-dimensional nature of the storm cannot be retrieved as with LMA (Cullen 2013; Cummins and Murphy 2009; Logan 2018). However, there are limitations of an LMA-only dataset including: (a) LMAs cannot distinguish between CG and IC flashes, (b) the polarity and magnitude of the lightning

flash are not readily available, and (c) the uncertainty of the data increases with the range of the sources which limits the data quality after roughly 100 km away from the LMA center (Cullen 2013; Ren et al. 2018).

2.2. Next Generation Weather Radar (NEXRAD)

Radar observations from the operational Next Generation Weather Radar (NEXRAD) Weather Surveillance Radar – 1988 Doppler edition (WSR-88D) network (Crum and Alberty 1993) were used to quantify the microphysical behavior that influences the lightning-precipitation interactions in the selected tropical cyclones. The WSR-88D platform, which includes 160 radars across the contiguous United States (CONUS), was fully upgraded to dual-polarization capabilities in June 2013. Each of the WSR-88D polarimetric radars retrieve data with a range resolution of 250 m, a temporal resolution of approximately 5 minutes on a polar grid, and an azimuthal resolution of 0.5° in the lowest three to five elevations with 1.0° aloft (Brauer et al. 2020; Homeyer et al. 2021; Crum and Alberty 1993). The new polarimetric variables observed by the upgraded NEXRAD WSR-88D system improves the ability to not only discriminate between meteorological and nonmeteorological scatterers, but also discern between various precipitation types by providing information on the size, shape, phase, and concentration of scatterers (Homeyer et al. 2021). These NEXRAD variables were further processed using the Gridded NEXRAD WSR-88D Radar (GridRad) software (Bowman and Homeyer 2017). GridRad performs numerous quality-control techniques and merges data from multiple radars onto a grid with 0.02° x 0.02° spatial resolution

(and 0.5 km vertical grid spacing below an altitude of 7 km with 1 km aloft) and 5-min temporal resolution, enabling the creation of plan and cross-section views of radar variables. North-South (N-S) and West-East (W-E) cross-sections were drawn through the regions of strongest convection in each rainband of focus for each case study.

The NEXRAD products employed in this study include reflectivity (Z_H), differential reflectivity (Z_{DR}), specific differential phase (K_{DP}), and correlation coefficient (ρ_{HV}). The Z_H is dependent on hydrometeor concentration and size due to its proportionality to the integration of the diameter of scatterers raised to the sixth power (e.g., Homeyer et al. 2021; Kumjian 2013). High Z_H values located above the melting level (0°C) are indicative of supercooled liquid raindrops or large ice particles produced by substantial convective updrafts (Cecil et al. 2002). In fact, many studies adopt the 30 dBZ Z_H echo height as a proxy for lightning activity (e.g., Carey and Rutledge 2000; Logan 2018, 2021; Petersen and Rutledge 2001; Stolz et al. 2014). The Z_{DR}, defined as the logarithmic ratio of the reflectivity factors at horizontal and vertical polarizations, provides insight into the hydrometeor's size, shape, and orientation, while K_{DP} is dependent on the number concentration of scatterers and compares the phase shift differentials between the horizontal and vertical polarizations (e.g., Kumjian 2013). Elevated positive values of Z_{DR} and K_{DP} extending above the melting level (i.e., Z_{DR} and K_{DP} columns) suggest the presence of vigorous convective updrafts that feature intense rain and flash rates (Fridlind et al. 2019; Sharma et al. 2021; van Lier-Walqui et al. 2016). The ρ_{HV} indicates the homogeneity of particles within the sample volume irrespective of size, which translates to $\rho_{HV} < 0.96$ for irregular mixed-phased

precipitation and ρ_{HV} close to 1 (i.e., unity) for uniform scatterers such as raindrops (e.g., Brauer et al. 2020; Kumjian 2013). Given that strong electric fields in the mixed-phase regions of convective clouds can align ice crystals vertically, negative values of Z_{DR} and K_{DP} in conjunction with ρ_{HV} close to unity may denote areas of enhanced ice production and charge generation (e.g., Kumjian 2013; Logan 2021).

2.3. Precipitation Measurements

Precipitation was measured using data obtained from both the Global Precipitation Measurement (GPM) mission and the Harris County Flood Control District (HCFCD). The GPM, a joint project between the National Aeronautics and Space Administration (NASA) and the Japan Aerospace Exploration Agency (JAXA), consists of a core satellite equipped with sensors including microwave imagers and precipitation radars (Skofronick-Jackson et al. 2018). The gauge-calibrated product from the Integrated Multi-satellite Retrievals for GPM (IMERG), a uniformly gridded precipitation estimate with a spatial resolution of $0.1° \times 0.1°$ and temporal resolution of 30 minutes, was utilized in this study to quantify the connection between heavy rainfall or rain rates with respect to lightning behavior in space and time. The GPM data were filtered for land-only values within the spatial domain 98°W, 27°N, 93°W, 32°N for Hurricane Harvey, while ocean-only values within the spatial domain defined by the maximum/minimum latitude and longitude values of the rainbands of focus were incorporated for Hurricane Nicholas to avoid contamination in the datasets.

The HCFCD was created by the Texas Legislature in 1937 as a response to the devastating floods that continuously afflicted the region. Currently, the HCFCD collects data from 188 automated gauge stations that measure rainfall amounts and monitor water levels in bayous and major streams. This study used data with a temporal resolution of 15 minutes from 141 rain gauges available across Harris County during Hurricane Harvey. The combined use of both precipitation datasets is beneficial because ground-based conventional rain gauge measurements, though precise, are limited by their sparse distribution and unavailability in remote areas (Xu et al. 2013). Skofronick-Jackson et al. (2018) reported that uncertainties due to bias and random errors in GPM are sufficiently low, being less than 50% at 1 mm hr^{-1} and less than 25% at 10 mm hr^{-1}. The performance of the GPM IMERG product compared to the HCFCD rain gauges during Hurricane Harvey is assessed in Appendix A.

2.4. Environmental Data

The dynamic and thermodynamic environments of each of the tropical cyclones were assessed using a variety of resources. Forecast soundings from the Rapid Refresh (RAP) model were extracted from the Sounding and Hodograph Analysis and Research Program in Python (SHARPpy) software to visualize the conditions in which storms developed and deduce the approximate altitudes of the 0°C, -10°C, -20°C, -30°C, and -40°C isotherms so that the depth of the mixed-phase region important for cloud electrification could be incorporated in the results. RAP soundings were initialized for the site in southeast Texas closest to the area of interest at the time of each case study for

Hurricane Harvey, while RAP soundings were initialized at a buoy site offshore for the case study times in Hurricane Nicholas. Note that these soundings are likely less representative of the specific oceanic environment of the outer rainbands in Hurricane Nicholas. Best track data for the tropical cyclones were acquired from the hurricane database (HURDAT2; Landsea and Franklin 2013) with information collected at each point along the track including: date and time, latitude and longitude of the tropical cyclone center at that time, mean sea level pressure (mb) at the tropical cyclone center, intensity of the tropical cyclone, and storm type. Each data point has a 6-h temporal resolution representing the center of the tropical cyclone circulation. Surface charts were retrieved from the Weather Prediction Center's (WPC) surface analysis archive to characterize the general synoptic setup at the surface during each tropical storm. Lastly, tropical cyclone reports from the National Hurricane Center (NHC) Data Archive were referenced for additional background information on each of the tropical events.

2.5. Tropical Cyclone and Case Selections

The spatial domain of this study is defined as the rectangle bounded by 27°-32°N and 93°-98°W, which contains the entire Houston metropolitan area extending out over the Gulf of Mexico. The period of interest for Hurricane Harvey is 0000 UTC 25 August 2017 to 0000 UTC 30 August 2017, while Hurricane Nicholas was examined from 0000 UTC 14 September 2021 to 0900 UTC 14 September 2021. Note that the periods of focus were selected based on the tropical cyclone's close proximity to southeast Texas.

Within each of the tropical events, case studies were chosen based on their extreme lightning and flooding activity.

The cases occurring on 27 August 2017 during Hurricane Harvey are as follows:

- **Case 1 (0100-0200 UTC)**: a convective rainband exhibiting peak flash rates of the five-day period
- **Case 2 (0510-0545 UTC)**: an embedded supercell (Logan 2021) with heightened lightning activity
- **Case 3 (1100-1200 UTC)**: shallow convection containing lower flash rates but higher rain rates

The cases occurring on 14 September 2021 during Hurricane Nicholas are as follows:

- **Case 1 (0000-0215 UTC):** pre-landfall convective rainband with high lightning and precipitation activity
- **Case 2 (0715-0815 UTC):** post-landfall convective rainband with moderate lightning and overall lower precipitation activity

Within each of the case studies, 10-minute time windows that displayed notable lightning and precipitation characteristics were investigated for a more detailed evaluation of their polarimetric radar attributes and electrical charge structures.

3. RESULTS

3.1. Hurricane Harvey (2017)

3.1.1. Event Background and Environmental Conditions

Hurricane Harvey originated from a tropical wave that moved off the western African coast on 12 August 2017 (Blake and Zelinsky 2018). As the shear relaxed, the system became a tropical depression east of Barbados around 0600 UTC 17 August and was upgraded to a tropical storm nearly 12 hours later. Subsequently, it was downgraded to a tropical wave during its westward track over the central Caribbean Sea, and re-intensified on 23 August in the light-shear, warm-water environment present in the western Gulf of Mexico. While forecast guidance began to indicate on 24 August that Harvey would continue to rapidly intensify prior to landfall, none of the models correctly predicted the magnitude of this intensification. In a mere 48-hour period, Harvey transitioned from a tropical depression to a Category 4 hurricane by 0000 UTC 26 August. Hurricane Harvey made landfall as a Category 4 storm with maximum sustained winds of 59 m s^{-1} and a minimum central pressure of 937 mb on 0300 UTC 26 August near Rockport, Texas.

Harvey was downgraded to a tropical storm shortly after landfall at 1800 UTC 26 August and eventually proceeded to slowly drift southeastward in southeast Texas and the adjacent Gulf waters over the next few days due to Harvey's position between two high pressure systems (Figure 2; Figure 3). During this time, southeast Texas continued to suffer from catastrophic flooding within the outer rainbands as a stationary front

enhanced surface convergence and lifted warm and humid air originating from the tropical system over the Gulf. Historic amounts of rainfall of more than 1,524 mm (60 in) were recorded at seven stations throughout southeast Texas, while eighteen values exceeding 1,219.2 mm (48 in) were measured across the region. As a result, Hurricane Harvey remains the second-most costly hurricane in United States history at $125 billion, and at least 68 people died from the effects of the storm in Texas which is the largest number of direct deaths from a tropical cyclone in that state since 1919. On 30 August, Harvey made its final landfall as a tropical storm in southwestern Louisiana before gradually weakening from a tropical depression to an extratropical cyclone by 0600 UTC 1 September over the Tennessee Valley. The full progression of the tropical cyclone track is shown in Figure 4.

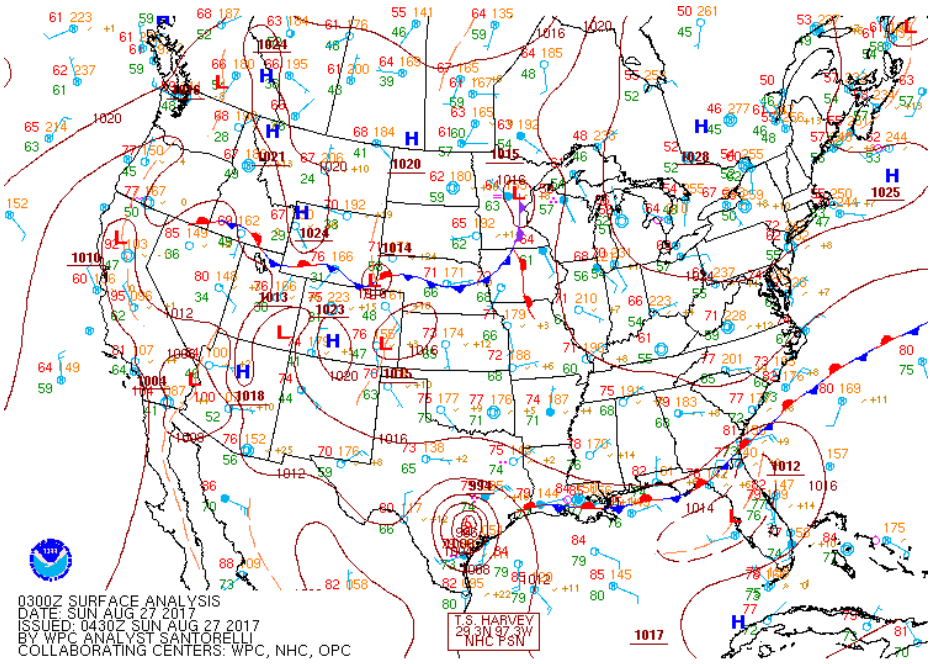

Figure 2: WPC surface analysis valid for 27 August 2017 at 0300 UTC.

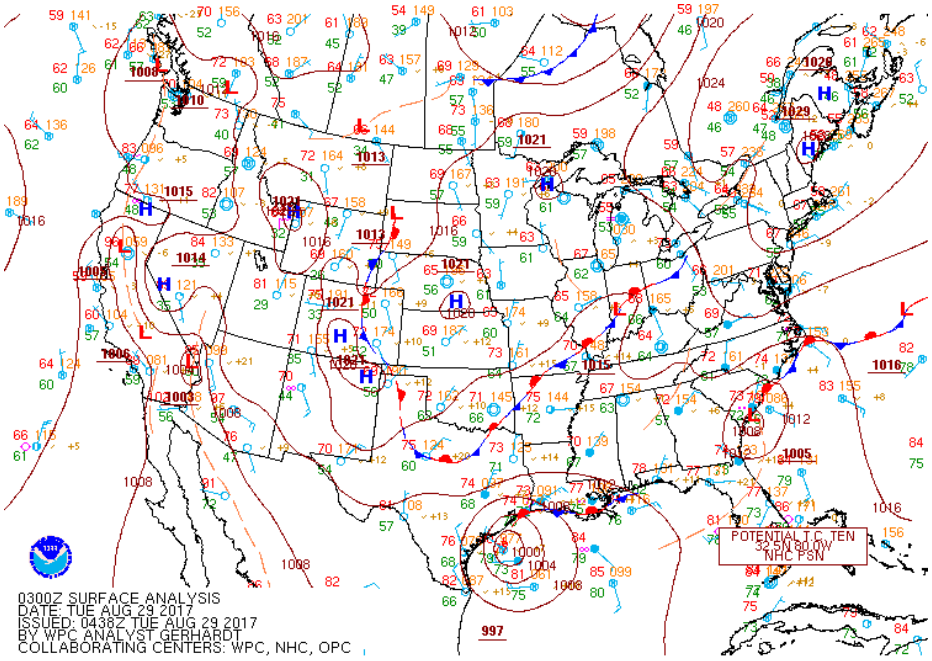

Figure 3: WPC surface analysis valid for 29 August 2017 at 0300 UTC.

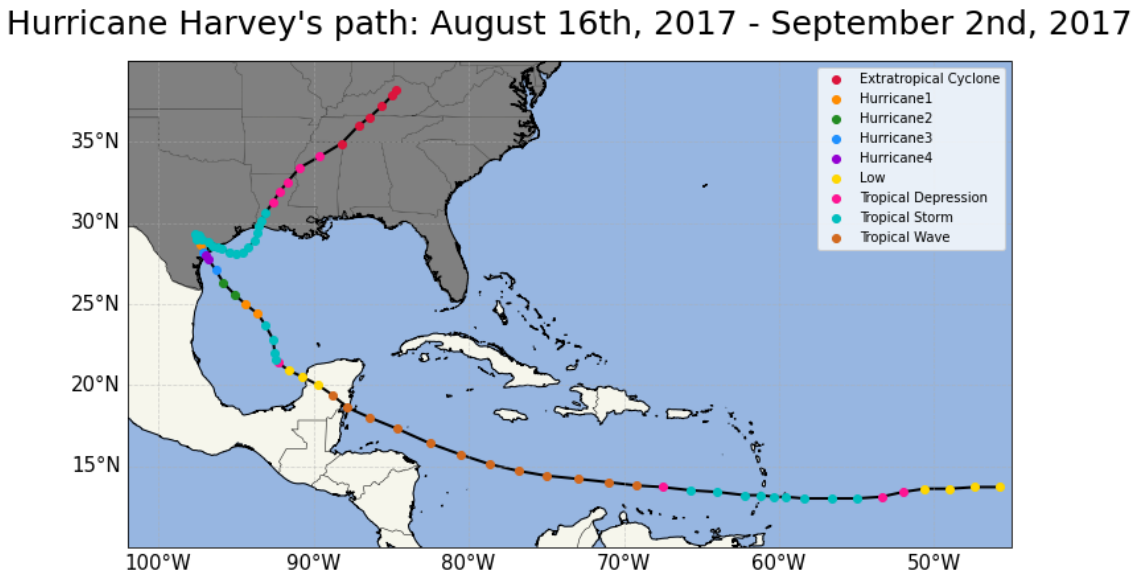

Figure 4: Hurricane database (HURDAT2) best track positions for Hurricane Harvey from 16 August 2017 to 2 September 2017 showing the temporal and categorical evolution of the tropical cyclone. Note that points are spaced in 6-h time increments.

3.1.2. Lightning and Precipitation Overview

Figure 5 presents the plan view of flash extent density with GPM precipitation rate contours overlaid for the outer rainbands during the five-day period of 0000 UTC 25 August to 0000 UTC 30 August, which featured Harvey's landfall and gradual exit from southeast Texas. The flash extent density can be defined as the total number of flashes that pass through a particular grid column (DiGangi et al. 2016). In comparison to the VHF source density, the implementation of flash extent density may be preferred because it produces a smoother profile and assigns equal weight to each grid box containing VHF sources, regardless of the actual quantity of sources within the grid box (Fuchs and Rutledge 2018). The peak time-averaged flash extent density of the study domain during the period was nearly 900 fl km^{-2} min^{-1}, while the peak time-averaged

rain rate reached 6.5 mm hr^{-1}. All three case studies, which remained within the 100-km radius of the centroid of the HLMA network (i.e., Downtown Houston), were visible in flash extent density maxima and were nearly spatially collocated with the highest precipitation rate contours (Figure 5). However, Case 3 (located to the far right of the 100-km radius HLMA circle in Chambers County) had its maximum flash extent density and rain rate values notably more offset than those of Case 1 and Case 2.

Figure 6 illustrates the time series of HLMA lightning flash rate and GPM precipitation rate for the outer rainbands during the five-day period of focus. As previously mentioned, the lightning flash rate was upscaled and the GPM rain rate was downscaled through interpolation to have a temporal resolution of 1 minute so that both datasets matched the same temporal scale, allowing for accurate comparisons between the two measurements. It is clear that the majority of lightning activity in the outer rainbands occurred on 27 August, which was about a day after Harvey made landfall. The peak spatially-averaged lightning flash rate during the time period was about 300 fl min^{-1}, which occurred at 0300 UTC 27 August around the time of Case 1. Meanwhile, the peak spatially-averaged rain rate of approximately 9 mm hr^{-1} occurred about 6 hours later at 0830 UTC around the same time as the last relative flash rate peak of 150 fl min^{-1}. The temporal lag between the highest lightning and precipitation rates is evident in Figure 6, which is consistent with results of previous studies (Carey and Rutledge 2000; Logan 2021; Solimine et al. 2022). The difference in times of the maxima in lightning and rain rate is postulated to be a result of the time it takes ice particles to undergo depositional growth and fall through the cloud to melt into raindrops. Similarities in the

lightning-precipitation behavior for Case 1 and Case 2 as seen in Figure 5 are also apparent in Figure 6 with those cases demonstrating extreme lightning activity and precipitation rates while Case 3, though having modest flash rates, also had extreme rainfall rates.

Given the importance of 27 August in terms of the lightning and precipitation yields during Hurricane Harvey, a closer look at that day is needed. Figure 7 provides various perspectives of the spatial and temporal features of lightning and precipitation in the outer rainbands on this day. A time-altitude series of HLMA VHF source rate with VHF source density contours overlaid can be viewed in Figure 7a. From 0000 UTC to 0900 UTC, which contains both Case 1 and Case 2, electrical activity at higher altitudes (greater than 15 km) was evident in the VHF source density product. Generally, lightning activity was observed around 10 km for the majority of deep convective cases in the Houston area, so Case 1 and Case 2 were noteworthy. From 0900 UTC to 1400 UTC, a time frame that consists of Case 3, VHF source points remained close to 10 km in altitude. In correspondence with the observations of the VHF source density for each case, the VHF source rates were considerably higher for Case 1 and Case 2 compared to Case 3. The highest VHF source rate for the day was at 0300 UTC with 177,472 src $(5\ \text{min})^{-1}$ and the largest VHF source density was 56.7 src km^{-1} $(5\ \text{min})^{-1}$. Figure 7b shows the charge altitude normalized histogram for all three cases on 27 August along with the mean altitude and cumulative density function. The mean altitude of Case 3 was noticeably lower than Case 1 and Case 2 at 7.8 km, while the Case 2 supercell displayed the highest source altitude heights overall with over 25% of the VHF source points

located above 11 km. Therefore, Figure 7a and Figure 7b suggest that Case 1 and Case 2 likely contained more powerful updrafts than the shallower convective Case 3.

Figure 7c presents a Hovmoeller diagram of VHF source density and GPM precipitation rate. Longitude values in the domain of interest were averaged to visualize the behavior of the lightning and precipitation hotspots as they propagate through time. The peak rainfall rate occurred around 0900 UTC at 33.2 mm hr^{-1} and was located at 29.5°N. As time progressed, the largest precipitation rates appeared to shift northward to around 30.5°N, yet the VHF source density maxima typically remained near the same latitudes. In fact, the first nine hours of the day had the highest lightning and precipitation regions spatially collocated, but the areas became offset during the time of Case 3. The plan view of VHF source density and GPM rain rate also demonstrates the peak lightning and precipitation areas to be collocated for Case 1 and Case 2, unlike Case 3 (Figure 7d). Indeed, the majority of the feeder bands seemed to consist of less intense, shallow convection with an embedded region of deep convection, concurrent with the observations of large spatial variability within the outer rainbands as discussed in the DeHart and Bell (2020) and Yang et al. (2019) studies. Further investigation of the lightning-precipitation microphysics for each individual case study is essential to discern the root of these discontinuities.

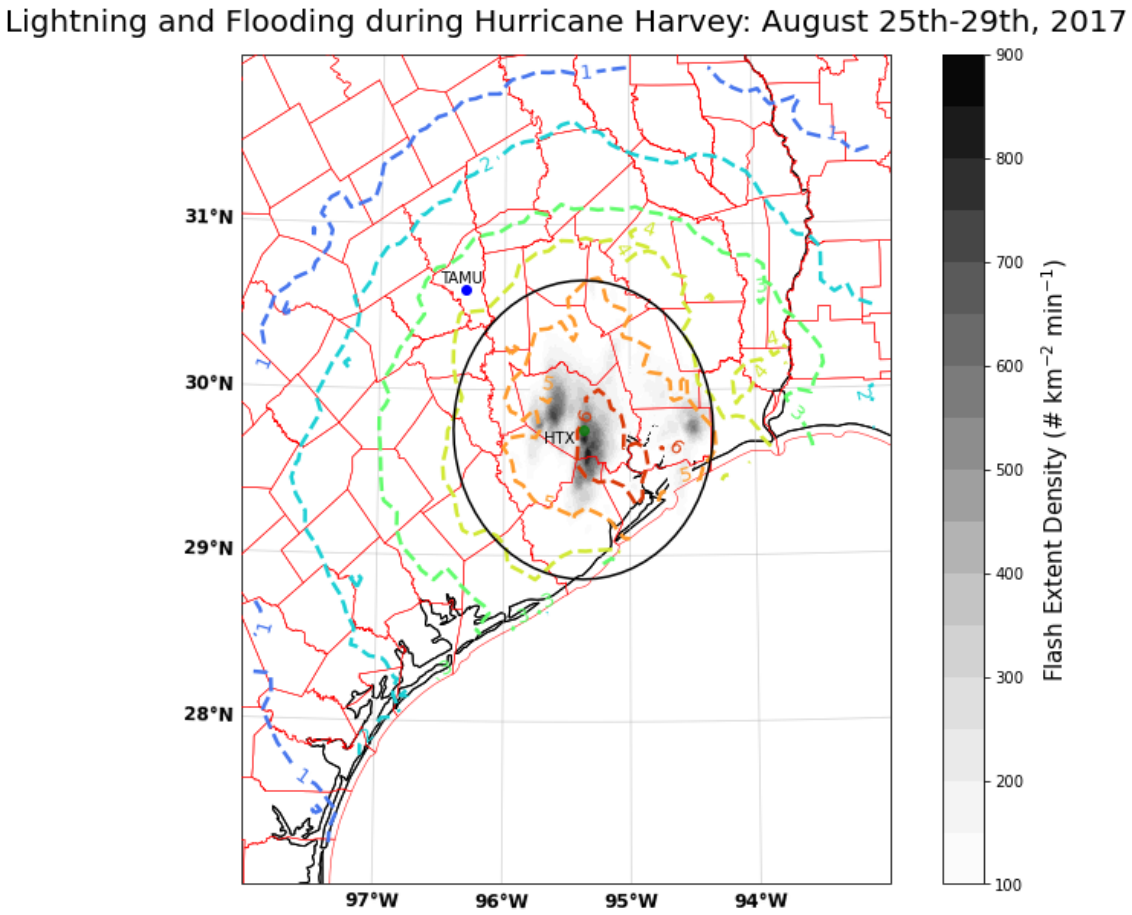

Figure 5: Plan view of flash extent density (black filled contours; # km^{-2} min^{-1}) with GPM precipitation rate (colored contours; mm hr^{-1}) overlaid for 0000 UTC 25 August 2017 to 0000 UTC 30 August 2017 during Hurricane Harvey. Note that the land-only values for lightning and precipitation are exhibited in an effort to only examine the outer rainbands. The flash extent density and GPM rain rate are averaged through time for the five-day period. The black circle illustrates the 100-km radius of detection of the HLMA network. Houston (HTX) and Texas A&M University (TAMU) are represented by the green and blue dots, respectively.

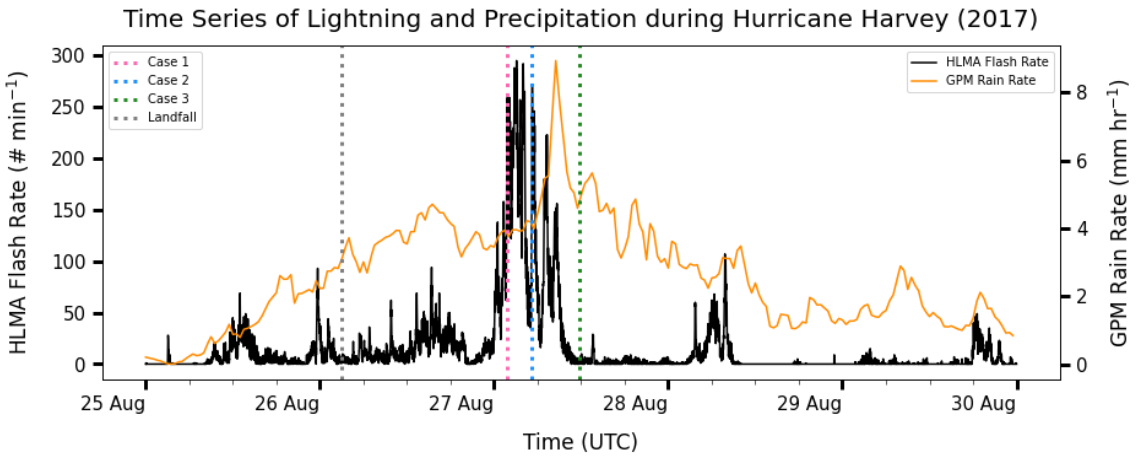

Figure 6: Time series of HLMA flash rate (# min^{-1}) denoted by the black line and GPM precipitation rate (mm hr^{-1}) denoted by the orange line from 0000 UTC 25 August 2017 to 0000 UTC 30 August 2017 during Hurricane Harvey. The times of the selected 10-minute case studies and landfall are marked by the dotted vertical lines. Note that the land-only values for lightning and precipitation are exhibited in an effort to only examine the outer rainbands. All flashes, big or small, are included in the HLMA lightning flash rate dataset. The HLMA flash rate and GPM rain rate was calculated for the spatially-averaged rectangular domain of 98°W, 27°N, 93°W, 32°N.

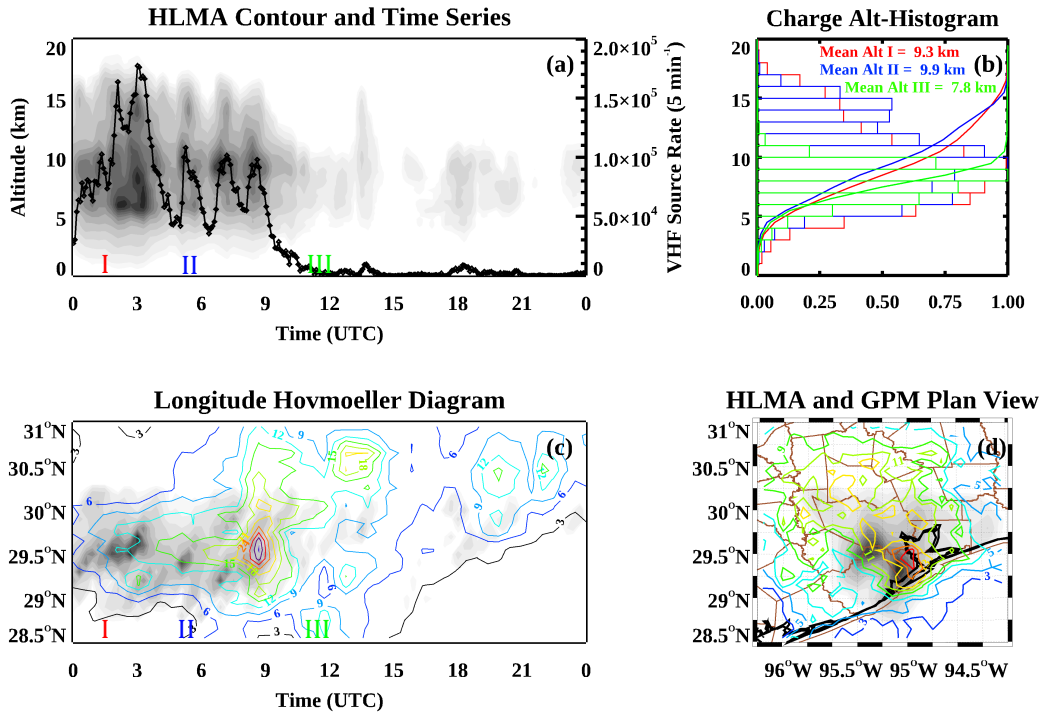

Figure 7: 27 August 2017 plots of (a) HLMA VHF source density (black filled contours) and VHF source rate (black line; # [5 min^{-1}]) time-altitude series, (b) charge altitude normalized histogram with mean altitude and cumulative distribution function line denoted for each case, (c) longitude-averaged Hovmoeller diagram of HLMA VHF source density (black filled contours) and GPM precipitation rate (colored contours; mm hr^{-1}), (d) plan view of HLMA VHF source density (black filled contours) and GPM precipitation rate (colored contours; mm hr^{-1}). Note that the land-only values for lightning and precipitation are exhibited in an effort to only examine the outer rainbands.

3.1.3. Case 1: 0100-0200 UTC 27 August 2017

A 0100 UTC forecast sounding from RAP at KHOU shows that the MUCAPE was at 1,253 J kg^{-1} and lower-tropospheric omega values were negative, implying that there was potential for the lifting of moist parcels in this unstable, tropical environment (Figure 8). The largest VHF source rate was 118,590 src (5 min^{-1}) and the largest VHF

source density was 39.7 src km^{-1} (5 min)$^{-1}$ during Case 1 (Figure 7a). The charge-altitude normalized histogram revealed that the mean altitude of the 1.1 million sources that transpired during Case 1 was 9.3 km, while greater than 25% of these sources were located above 10 km (Figure 7b). Additionally, the largest values of lightning and precipitation for the hour were observed from 0140 to 0200 UTC (Figure 7c). The peak rain rate of 49.5 mm hr^{-1} and peak VHF source density of 1,818.5 src km^{-2} during Case 1 (not shown) were both located within the region of deep convection.

The polarity of lightning flashes can aid in classifying the structure and behavior of a storm. While thunderstorms typically lower negative charge to the ground nearly 90% of the time (Rakov and Uman 2003), severe thunderstorms can generate higher amounts of +CGs (Carey and Rutledge 2003; Logan 2018; Sharma et al. 2021; Wiens et al. 2005). Moreover, storms with anomalous charge structures tend to favor the prevalence of not only +CGs but inverted cloud flashes (i.e., -ICs) as well, especially if the charge structure is an anomalous tripole with a lower negative charge layer (DiGangi et al. 2022; MacGorman et al. 2005; Wiens et al. 2005). Figure 9 shows a time series of the NLDN flash rate for each type and polarity of lightning with the corresponding charge analysis performed using both the HLMA and NLDN datasets overlaid during Case 1. The NLDN observed 13,258 flashes during Case 1, with roughly 19% being +CG and 13% being -IC. The total number of "big" flashes that were examined in the charge analysis during Case 1 was 162, but the HLMA detected 12,885 flashes throughout the hour. Overall, the spikes in flash rate coincided with increases in the altitudes of the charge layers. This trend was most notable from 0140 to 0150 UTC when

flash rates reached 558 fl min^{-1} and charge heights reached nearly 18 km, which indicates that the rainband was likely undergoing intensification. For this reason, the lightning and precipitation microphysics of this 10-minute period were studied in greater depth using polarimetric radar observations.

Figure 10 and Figure 11 show 5-minute timesteps of radar reflectivity (Z_H) and negative differential reflectivity (Z_{DR}) in both plan and cross-sectional views with the charge analysis overlaid during the 10-minute period from 0140 to 0150 UTC for Case 1. The zoomed vertical cross sections in Figure 10 and Figure 11 are shown in Figure 12. The structure and intensity of the rainband is evident in the plan views (Figure 10a; Figure 11a), with the vigor of this feeder band justified further in the cross-sectional views with the Z_H echo height exceeding 30 dBZ well above the melting level (Figure 10b,c; Figure 11b,c; Figure 12). Furthermore, the cross sections also show negative Z_{DR} values increasing aloft over time implying vertically-oriented ice particles, and this feature is paralleled by an increase in VHF sources and thus charging with time. The charge analysis performed for the highly-electrified deep convective rainband revealed an inverted tripole charge structure with a positive layer located at 6 km sandwiched between two negative layers at 4.1 km and 7.5 km (Figure 10d). The lower negative layer appeared to grow larger with time while the upper negative layer grew smaller, suggesting that the larger ice particles were falling through the cloud and building up the lower charge layer (Figure 11d), a process referred to as gravitational settling. However, all of the charge layers rose in height with time (roughly 0.3-0.4 km) due to the updraft

likely increasing in strength, which was indicated by the presence of elevated VHF sources at high heights.

Figure 13 displays vertical cross sections of differential reflectivity (Z_{DR}), specific differential phase (K_{DP}), and correlation coefficient (ρ_{HV}) with the approximate altitudes of each charge layer overlaid from 0140 to 0150 UTC within Case 1. While the highest Z_{DR} values (> 1.5 dB) and K_{DP} values (> 2.5 deg km^{-1}) denoted the presence of high concentrations of large raindrops below the melting layer, there were some elevated values aloft which suggests vigorous updrafts (Figure 13a,b,c,d). Nonetheless, Z_{DR} and K_{DP} were observed to be negative aloft (> 0°C or 4.6 km) above the convective area, which indicated that a strong electric field was present to orient the ice particles vertically. Therefore, the powerful updraft was likely facilitating collisions between these ice particles and thus potential charging could be occurring. Indeed, cloud electrification became apparent in that ρ_{HV} was typically close to unity aside from a notable decrease in regions coinciding with negative Z_{DR} and K_{DP} values, implying the existence of hydrometeors of varying size and shape such as ice and supercooled liquid water needed for the NIC mechanism (Figure 13e,f). The charge layers generally resided within the 0°C to -20°C isotherm levels, and the polarimetric variables verified that additional charging was occurring above this region with areas of negative Z_{DR} and K_{DP} collocated with decreased ρ_{HV}. Lower ρ_{HV} (<0.90) and elevated Z_{DR} values were also examined in the melting layer as a “bright band” signature (Kumjian 2013) in the regions with more stratiform convection, consistent with the sounding data (Figure 8).

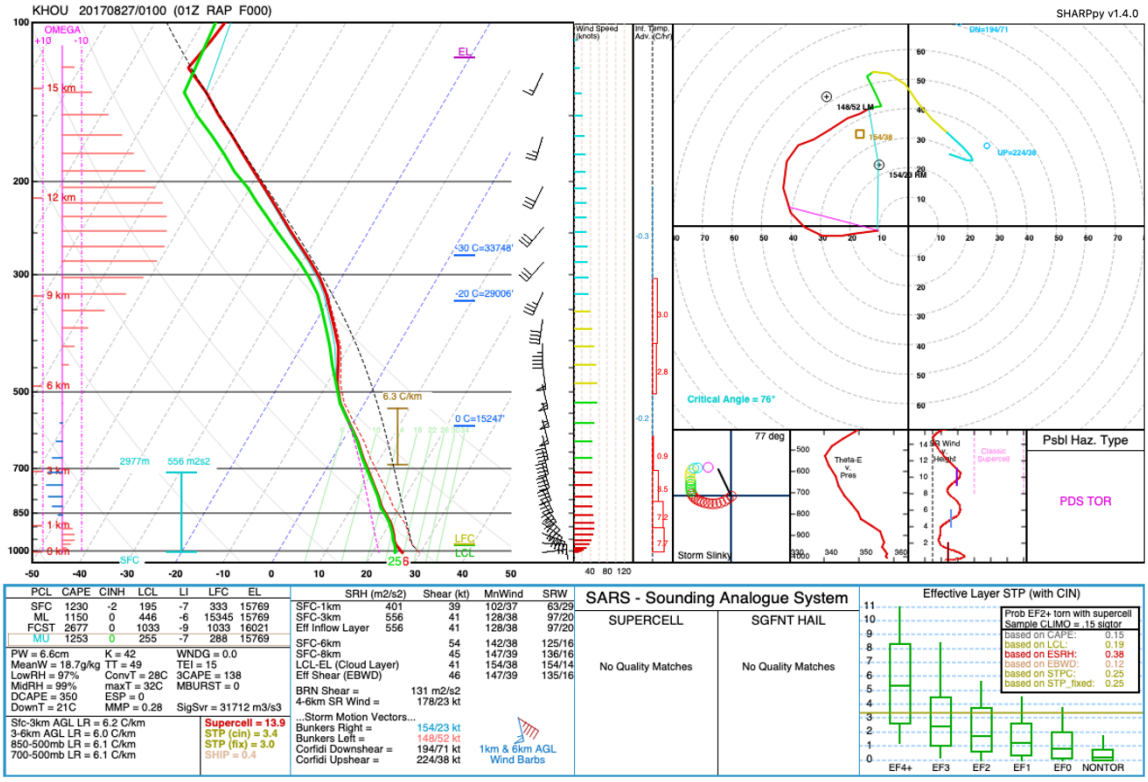

Figure 8: Forecast RAP sounding at 0100 UTC 27 August 2017 (initialized at 0100 UTC) at KHOU.

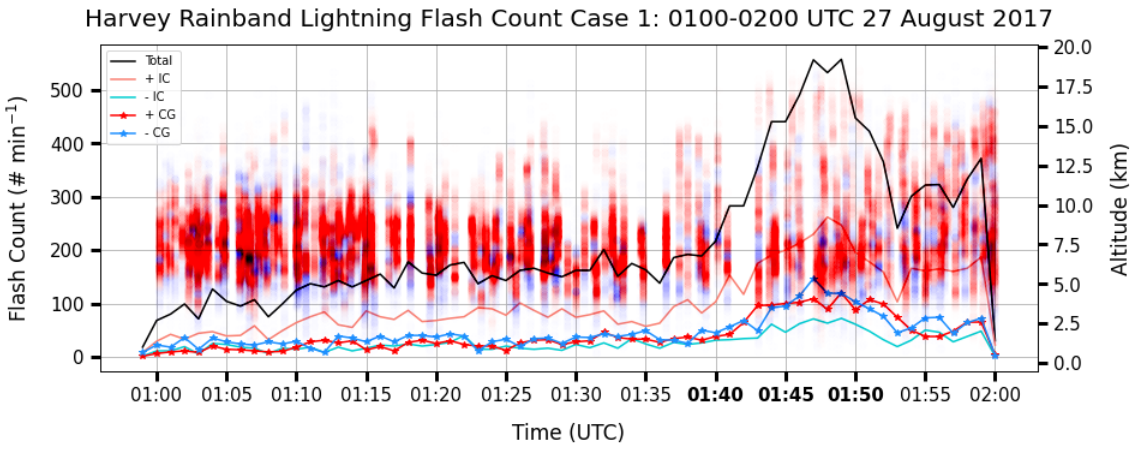

Figure 9: Hurricane Harvey Case 1 NLDN flash rate (# min^{-1}) time series with the corresponding charge analysis utilizing both HLMA and NLDN datasets overlaid. In addition to the total NLDN flash rate, the +IC, -IC, +CG, and -CG flash rates are displayed as well. The red dots represent the positive sources while the blue dots represent the negative sources within each lightning flash, and each source dot is plotted at the location of its respective altitude in km. Note that only the flashes and sources within the outer rainband of focus are included. The charge analysis only examines the "big" flashes with at least 1000 VHF source points for this particular case. The times of the 10-minute period that will be analyzed further using polarimetric radar observations are in bold.

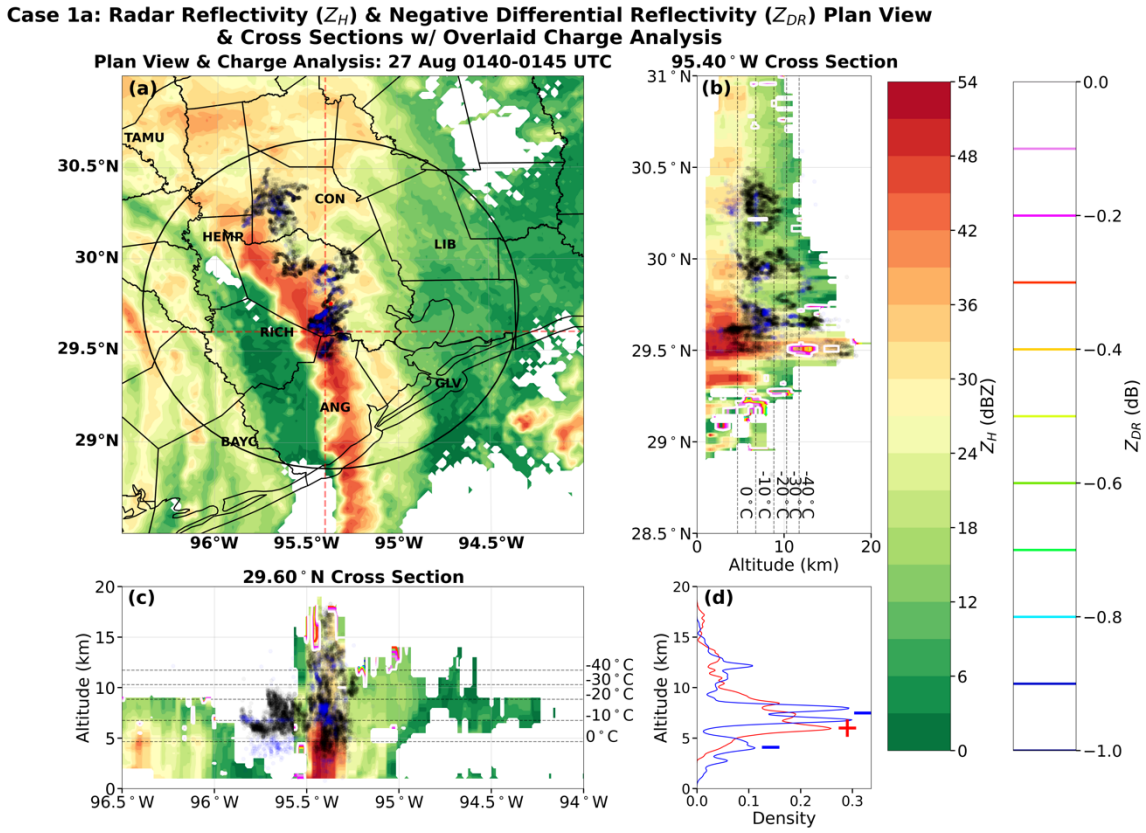

Figure 10: 0140-0145 UTC 27 August 2017 plots of (a) NEXRAD composite (column maximum) radar reflectivity (Z_H) plan view with overlaid charge analysis, (b) N-S 95.40°W longitude cross section with both negative Z_{DR} (colored contours) and charge analysis overlaid, (c) W-E 29.60°N latitude cross section with both negative Z_{DR} (colored contours) and charge analysis overlaid, (d) altitude kernel density estimation (KDE) of positive and negative HLMA source counts. The charge analysis only examines the "big" flashes with at least 1000 VHF source points for this particular case. Positive sources are represented by black dots, while negative sources are represented by the blue dots. The black circle in (a) illustrates the 100-km radius of detection of the HLMA network, and Houston, Texas, the center of the HLMA network, is marked by the red dot. The dotted red vertical and horizontal lines in (a) show where the cross sections were drawn. The 0°C, -10°C, -20°C, -30°C, and -40°C isotherms were extracted from the sounding and overlaid onto (b) and (c) to gain more insight on the hydrometeor size, shape, and phase. The approximate altitudes of each of the charge layers are denoted by red plus signs and blue minus signs in (d).

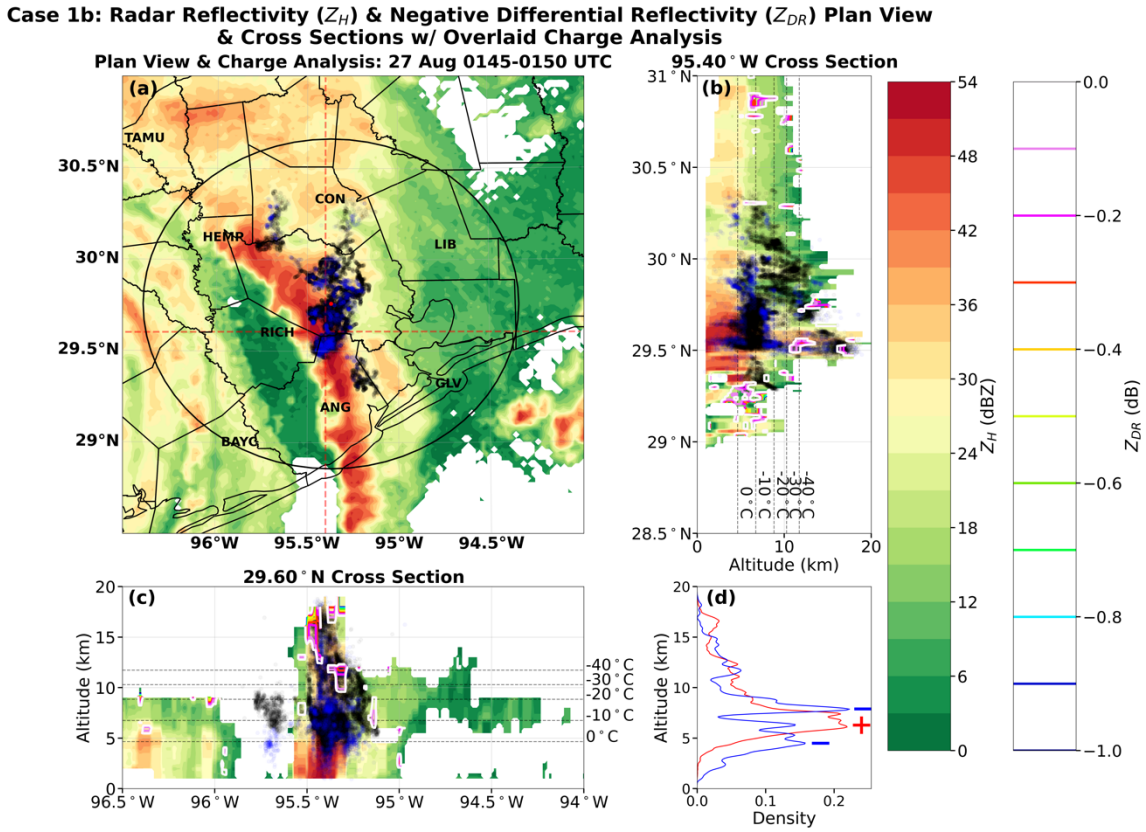

Figure 11: 0145-0150 UTC 27 August 2017 plots of (a) NEXRAD composite (column maximum) radar reflectivity (Z_H) plan view with overlaid charge analysis, (b) N-S 95.40°W longitude cross section with both negative Z_{DR} (colored contours) and charge analysis overlaid, (c) W-E 29.60°N latitude cross section with both negative Z_{DR} (colored contours) and charge analysis overlaid, (d) altitude kernel density estimation (KDE) of positive and negative HLMA source counts. The charge analysis only examines the "big" flashes with at least 1000 VHF source points for this particular case. Positive sources are represented by black dots, while negative sources are represented by the blue dots. The black circle in (a) illustrates the 100-km radius of detection of the HLMA network, and Houston, Texas, the center of the HLMA network, is marked by the red dot. The dotted red vertical and horizontal lines in (a) show where the cross sections were drawn. The 0°C, -10°C, -20°C, -30°C, and -40°C isotherms were extracted from the sounding and overlaid onto (b) and (c) to gain more insight on the hydrometeor size, shape, and phase. The approximate altitudes of each of the charge layers are denoted by red plus signs and blue minus signs in (d).

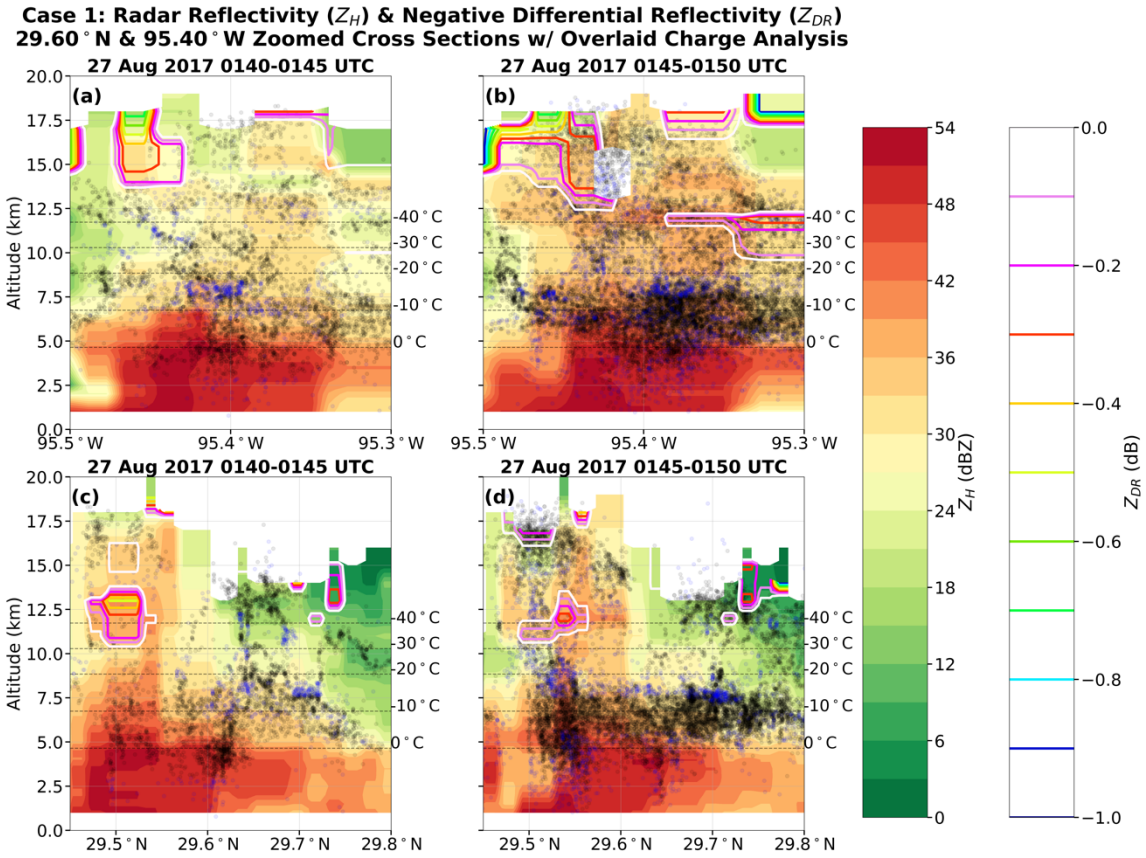

Figure 12: Case 1 (0140-0150 UTC 27 August 2017) zoomed vertical cross sections with both negative Z_{DR} (colored contours) and charge analysis overlaid at (a) W-E 29.60°N latitude from 0140-0145 UTC, (b) W-E 29.60°N latitude from 0145-0150 UTC, (c) N-S 95.40°W longitude from 0140-0145 UTC, (d) N-S 95.40°W longitude from 0145-0150 UTC. The charge analysis only examines the "big" flashes with at least 1000 VHF source points for this particular case. Positive sources are represented by black dots, while negative sources are represented by the blue dots. The 0°C, -10°C, -20°C, -30°C, and -40°C isotherms were extracted from the sounding and overlaid onto each subplot to gain more insight on the hydrometeor size, shape, and phase.

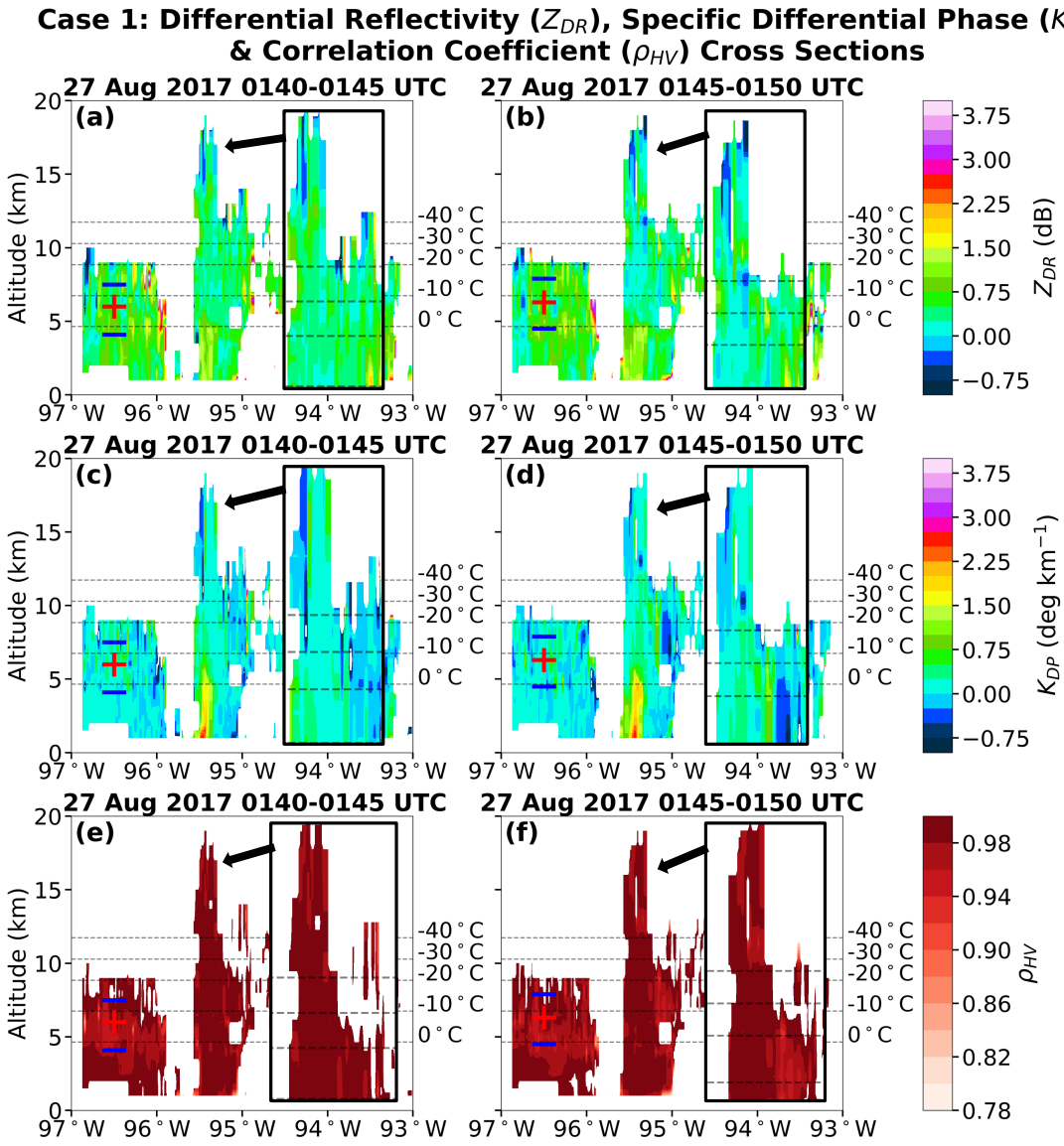

Figure 13: Case 1 (0140-0150 UTC 27 August 2017) vertical cross sections of (a) Z_{DR} at 0140-0145 UTC, (b) Z_{DR} at 0145-0150 UTC, (c) K_{DP} at 0140-0145 UTC, (d) K_{DP} at 0145-0150 UTC, (e) ρ_{HV} at 0140-0145 UTC, (f) ρ_{HV} at 0145-0150 UTC. Note that the same W-E oriented cross section as the three previous figures was used. The charge analysis only examines the "big" flashes with at least 1000 VHF source points for this particular case. The approximate altitudes of each of the charge layers are denoted by red plus signs and blue minus signs. The 0°C, -10°C, -20°C, -30°C, and -40°C isotherms were extracted from the soundings and overlaid onto each subplot to gain more insight on the hydrometeor size, shape, and phase.

3.1.4. Case 2: 0510-0545 UTC 27 August 2017

Given MUCAPE values of 1,637 J kg^{-1} and 0-1 km SRH values well above 100 m^2 s^{-2}, there was sufficient instability and shear in this supercell environment to support a powerful, rotating updraft (Figure 14). This signature of elevated VHF sources detected in regions aloft such as the overshooting top of supercells agrees with previous studies examining supercell lightning characteristics (Calhoun et al. 2013; DiGangi et al. 2016; Sharma et al. 2021; Wiens et al. 2005). However, an aspect that set Case 2 apart from Case 1 was the appearance of a distinct VHF source layer located at lower levels (Figure 7a). While higher-altitude lightning is classified as a dynamical process, lower-altitude lightning is likely related to the storm microphysics. From 0510 to 0550 UTC, both the lower and upper layers of enhanced VHF source density coexisted with the peak VHF source density layer at 10 km. The highest VHF source rate occurred around 0518 UTC with 108,270 src $(5\ min)^{-1}$. The three-layer VHF source density maxima model of Case 2 was highlighted in the charge-altitude normalized histogram with three peaks shown (Figure 7b). The mean altitude of the 710,000 VHF sources during this case was 9.9 km, yet roughly 25% of these sources were located below 7 km. The Hovmoeller diagram in Figure 7c showed that the highest Case 2 source densities occurred from 0500 to 0545 UTC while the peak Case 2 precipitation rate of 18.1 mm hr^{-1} occurred around 0600 UTC. Note that a slight temporal lag in the largest precipitation values from the largest source density values was also observed in Case 1, but that lag was only 10-20 minutes in contrast to the nearly 30-minute lag in Case 2. Despite this temporal offset, the peak VHF source density of roughly 1,764 src km^{-2} and peak GPM rain rate

of 40.6 mm hr^{-1} during Case 2 (not shown) were generally collocated spatially within the weaker convection of the feeder band.

Figure 15 presents the time series of NLDN flash rate of each type and polarity of lightning with the charge analysis performed for Case 2 overlaid. There was a total of 11,923 flashes accounted for by the NLDN, and 13% of these were +CGs while 13% were -ICs. Meanwhile, the charge analysis was carried out for a total of 155 "big" flashes, while the HLMA detected 7,984 flashes during the entirety of Case 2. Consistent with the results of Case 1, any uptick in flash rate was accompanied by higher-altitude lightning. It should be noted that the downticks in lightning flash rate were conversely associated with a lowering in charge altitude heights as well. Higher-altitude lightning seemed to be more prominent throughout the entirety of Case 2, suggesting that the updraft in the Case 2 supercell was more intense than that of the deep convective cell in Case 1. Even though the highest flash rate of 425 fl min^{-1} occurred around 0528 UTC, the 10-minute period of 0510 to 0520 UTC was further examined with polarimetric radar variables because of the larger amount of VHF sources and flashes observed during this time, as well as the largest +CG flash rate of the whole period within this 10-minute window.

The 5-minute timesteps of Z_H and negative Z_{DR} in both plan and cross-sectional views with the charge analysis overlaid during the 10-minute period from 0510 to 0520 UTC during Case 2 are shown in Figure 16 and Figure 17. The zoomed vertical cross sections in Figure 16 and Figure 17 are shown in Figure 18. The structure of the rainband containing the embedded supercell is discerned well with Z_H in the plan views

(Figure 16a; Figure 17a). The spatial extent of the Case 2 feeder band was considerably less than that of Case 1, which is likely the reason why Case 2 had overall less lightning and precipitation than Case 1 given its more centralized nature. Nevertheless, the cross sections show that the convection was more powerful in Case 2 with Z_H values exceeding 54 dBZ above the melting layer (Figure 16b,c; Figure 17b,c; Figure 18). Similar to Case 1, Case 2 also had negative Z_{DR} values well above the melting level, indicating the existence of vertically-oriented ice particles such as needles and columns required for charging mechanisms. The charge analysis executed for this supercell conveyed an inverted tripole charge structure with a positive layer located around 10 km sandwiched in between two negative layers located near 6 km and 15 km (Figure 16d; Figure 17d). While both Case 1 and Case 2 had this anomalous tripolar structure, the charge layers in Case 1 were situated appreciably lower than the charge layers in Case 2, which is likely a result of complex storm dynamics within the supercell. As time progressed, not only did all of the charge layers rise in altitude, but the lower negative layer and positive layer became less dense while the upper negative layer grew denser. Therefore, the robust updraft could have been lofting the ice particles and supercooled liquid water droplets upwards, subsequently creating lightning at higher altitudes and thus signifying storm intensification.

Figure 19 shows vertical cross sections of Z_{DR}, K_{DP}, and ρ_{HV} with the estimated altitudes of each charge layer overlaid from 0510 to 0520 UTC within Case 2. The largest Z_{DR} values (> 2 dB) and K_{DP} values (> 3 deg km^{-1}) remained typically below the melting layer at 4.97 km, yet Z_{DR} ranging from 1-2 dB and K_{DP} up to 2.75 deg km^{-1}

extended up to 7 km during each scan (Figure 19a,b,c,d). Recall that a lightning jump occurred during the second 5-minute time frame when these variables increased in value above the melting layer, a characteristic that was also seen in Z_{DR} column volume by Sharma et al. (2021). Compared to Case 1, Case 2 had greater Z_{DR} and K_{DP} values reaching higher heights, implying that the turbulent supercell updraft was able to produce a higher concentration of large hydrometeors and supercooled liquid water than the deep convective updraft in Case 1. The intensity of the rainfall is emphasized with lower ρ_{HV} values (Figure 19e,f) near the surface coinciding with the updraft marked by large values of Z_{DR} and K_{DP}, as heavier precipitation tends to have a wider drop size spectrum that slightly reduces ρ_{HV} (e.g., Didlake and Kumjian 2017). Above the convective core, negative values of Z_{DR} and K_{DP} were present and were collocated with areas of depressed ρ_{HV} values, inferring that mixed-phase hydrometeors coexisted here and likely participated in cloud electrification (Figure 19e,f). The distinct supercell dynamics active in Case 2 were further demonstrated by lower, more numerous ρ_{HV} values in the convective area than Case 1. Another "bright band" feature was observed in the surroundings regions of shallow convection with $\rho_{HV} < 0.90$ and $Z_{DR} > 2$ dB along the melting level deduced from the sounding in Figure 14. The lower negative layer resided between the 0°C and -10°C isotherms, the positive layer was found between the -20°C and -30°C levels, and the upper negative layer was located well above the -40°C altitude.

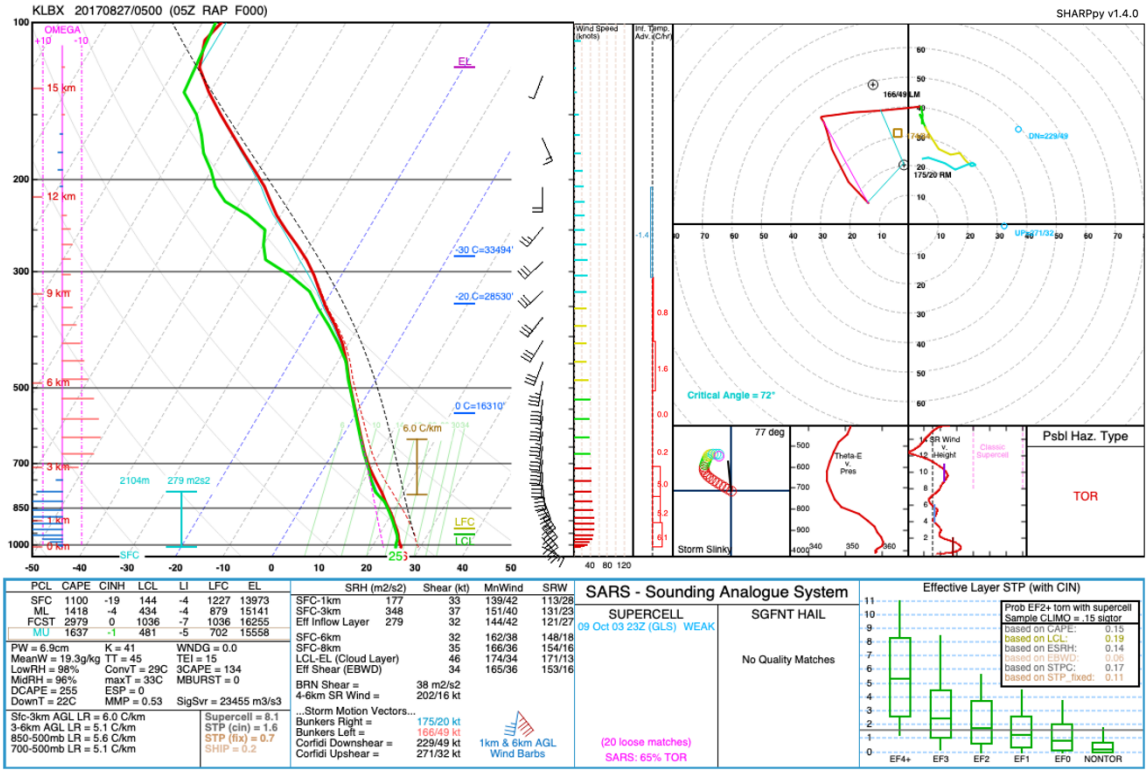

Figure 14: Forecast RAP sounding at 0500 UTC 27 August 2017 (initialized at 0500 UTC) at KLBX.

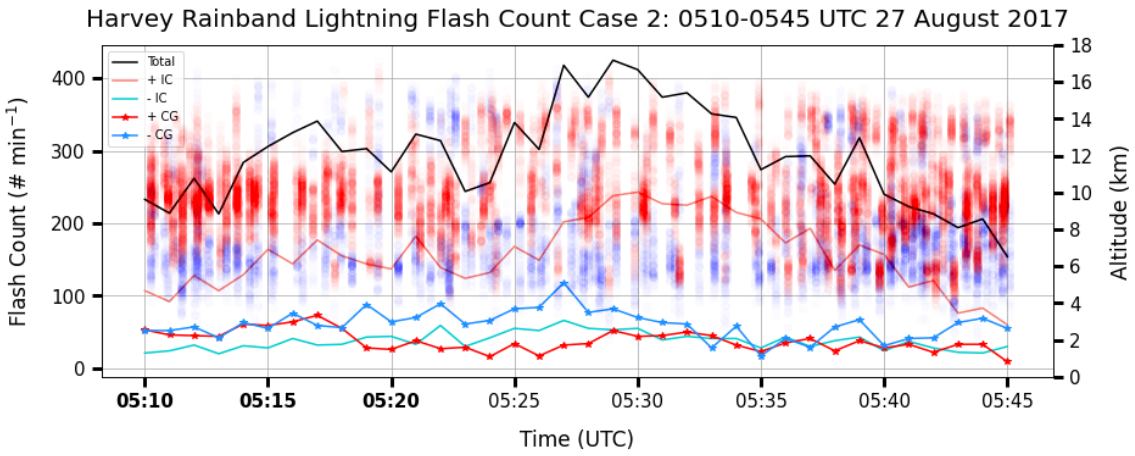

Figure 15: Hurricane Harvey Case 2 NLDN flash rate (# min^{-1}) time series with the corresponding charge analysis utilizing both HLMA and NLDN datasets overlaid. In addition to the total NLDN flash rate, the +IC, -IC, +CG, and -CG flash rates are displayed as well. The red dots represent the positive sources while the blue dots represent the negative sources within each lightning flash, and each source dot is plotted at the location of its respective altitude in km. Note that only the flashes and sources within the outer rainband of focus are included. The charge analysis only examines the "big" flashes with at least 250 VHF source points for this particular case. The times of the 10-minute period that will be analyzed further using polarimetric radar observations are in bold.

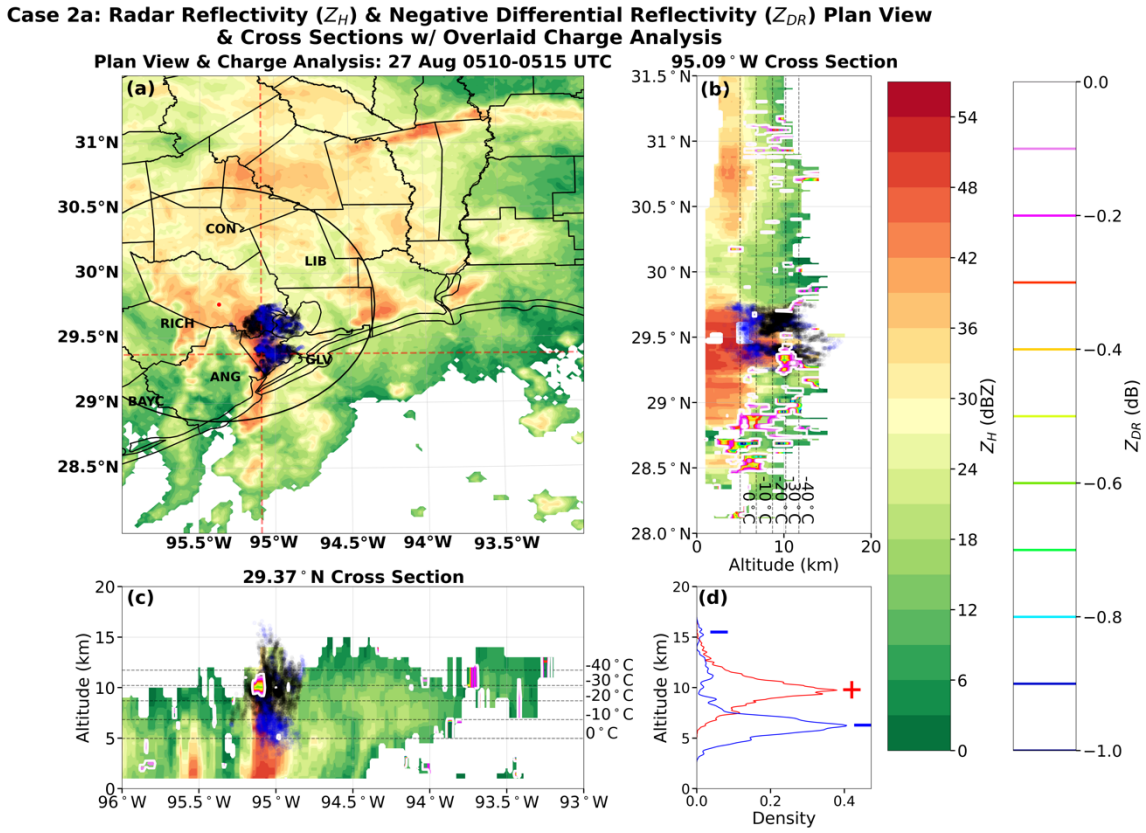

Figure 16: 0510-0515 UTC 27 August 2017 plots of (a) NEXRAD composite (column maximum) radar reflectivity (Z_H) plan view with overlaid charge analysis, (b) N-S 95.09°W longitude cross section with both negative Z_{DR} (colored contours) and charge analysis overlaid, (c) W-E 29.37°N latitude cross section with both negative Z_{DR} (colored contours) and charge analysis overlaid, (d) altitude kernel density estimation (KDE) of positive and negative HLMA source counts. The charge analysis only examines the "big" flashes with at least 250 VHF source points for this particular case. Positive sources are represented by black dots, while negative sources are represented by the blue dots. The black circle in (a) illustrates the 100-km radius of detection of the HLMA network, and Houston, Texas, the center of the HLMA network, is marked by the red dot. The dotted red vertical and horizontal lines in (a) show where the cross sections were drawn. The 0°C, -10°C, -20°C, -30°C, and -40°C isotherms were extracted from the sounding and overlaid onto (b) and (c) to gain more insight on the hydrometeor size, shape, and phase. The approximate altitudes of each of the charge layers are denoted by red plus signs and blue minus signs in (d).

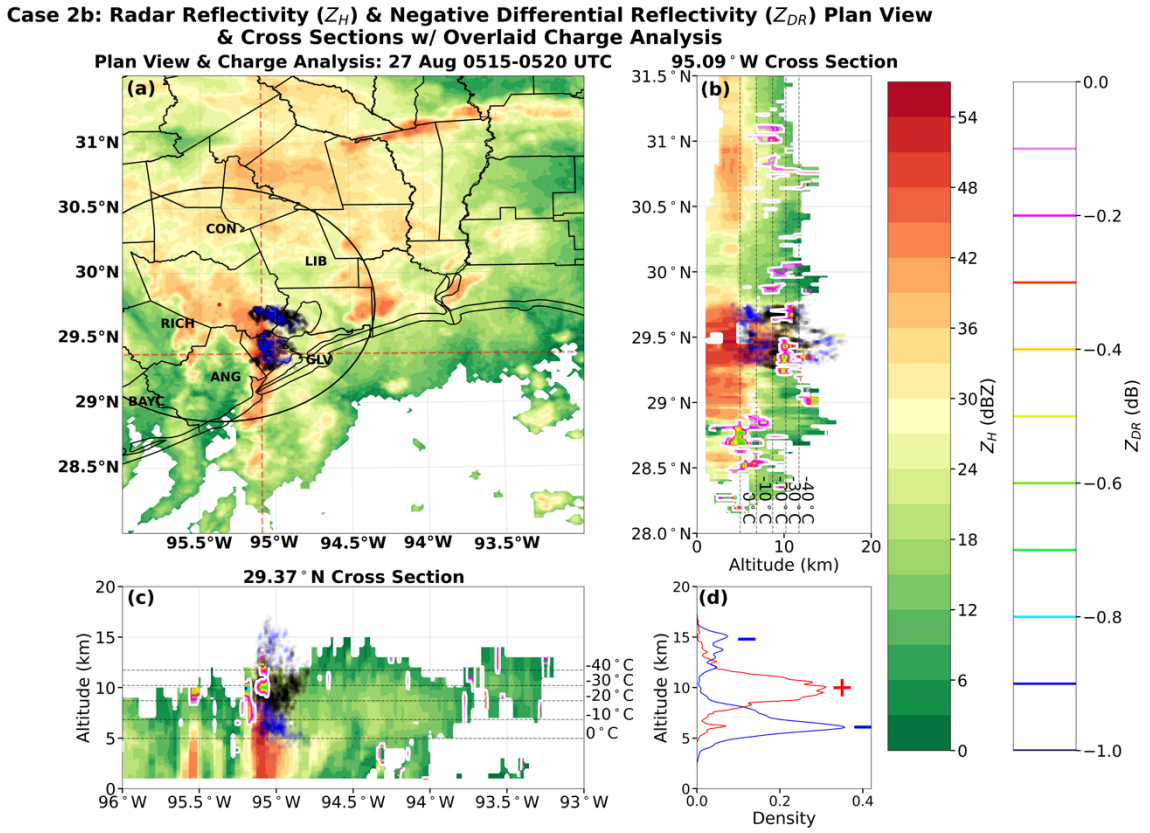

Figure 17: 0515-0520 UTC 27 August 2017 plots of (a) NEXRAD composite (column maximum) radar reflectivity (Z_H) plan view with overlaid charge analysis, (b) N-S 95.09°W longitude cross section with both negative Z_{DR} (colored contours) and charge analysis overlaid, (c) W-E 29.37°N latitude cross section with both negative Z_{DR} (colored contours) and charge analysis overlaid, (d) altitude kernel density estimation (KDE) of positive and negative HLMA source counts. The charge analysis only examines the "big" flashes with at least 250 VHF source points for this particular case. Positive sources are represented by black dots, while negative sources are represented by the blue dots. The black circle in (a) illustrates the 100-km radius of detection of the HLMA network, and Houston, Texas, the center of the HLMA network, is marked by the red dot. The dotted red vertical and horizontal lines in (a) show where the cross sections were drawn. The 0°C, -10°C, -20°C, -30°C, and -40°C isotherms were extracted from the sounding and overlaid onto (b) and (c) to gain more insight on the hydrometeor size, shape, and phase. The approximate altitudes of each of the charge layers are denoted by red plus signs and blue minus signs in (d).

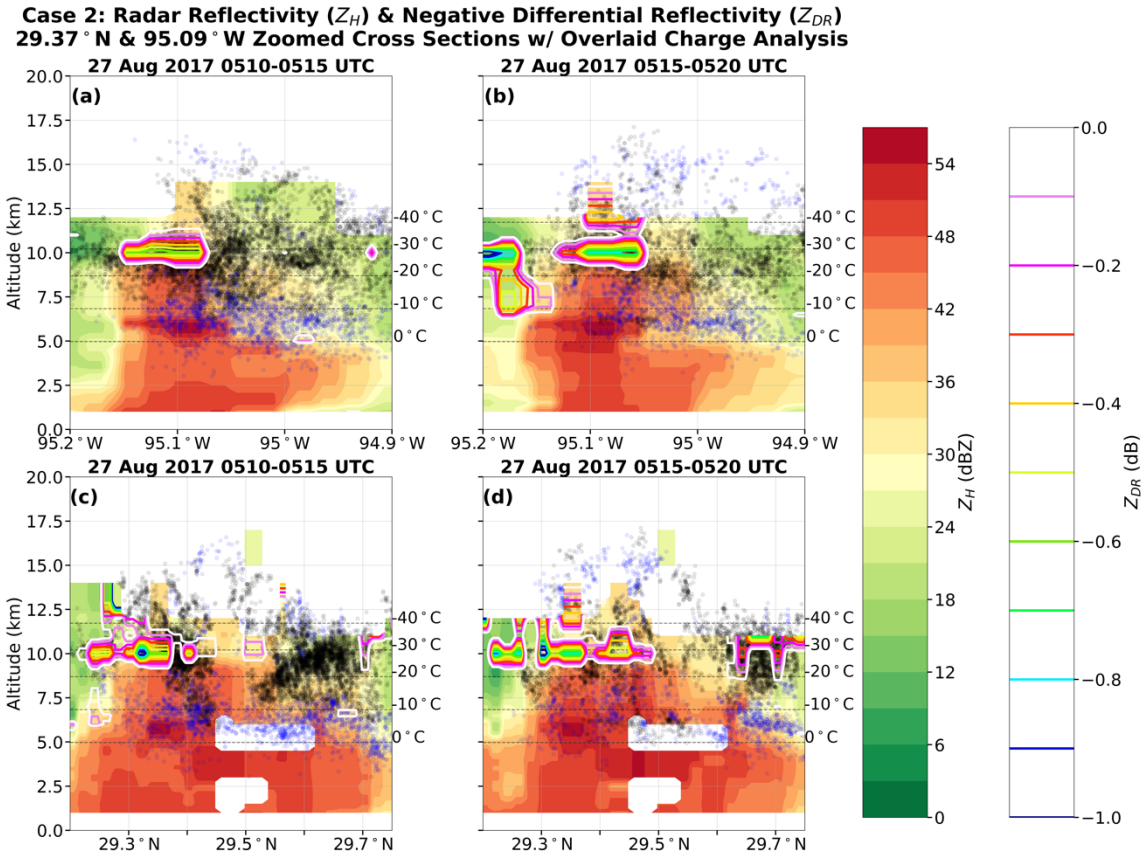

Figure 18: Case 2 (0510-0520 UTC 27 August 2017) zoomed vertical cross sections with both negative Z_{DR} (colored contours) and charge analysis overlaid at (a) W-E 29.37°N latitude from 0510-0515 UTC, (b) W-E 29.37°N latitude from 0515-0520 UTC, (c) N-S 95.09°W longitude from 0510-0515 UTC, (d) N-S 95.09°W longitude from 0515-0520 UTC. The charge analysis only examines the "big" flashes with at least 250 VHF source points for this particular case. Positive sources are represented by black dots, while negative sources are represented by the blue dots. The 0°C, -10°C, -20°C, -30°C, and -40°C isotherms were extracted from the sounding and overlaid onto each subplot to gain more insight on the hydrometeor size, shape, and phase.

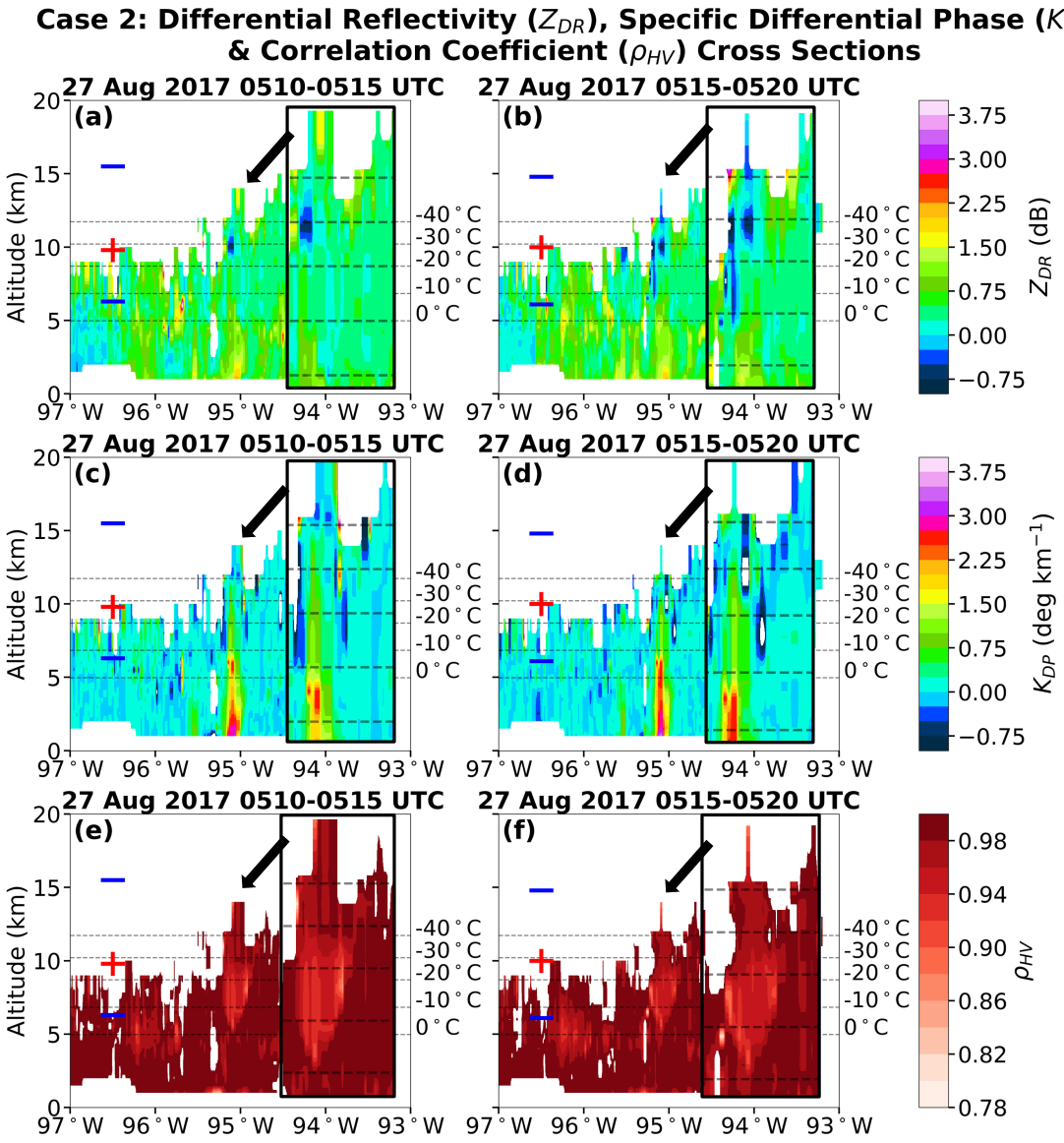

Figure 19: Case 2 (0510-0520 UTC 27 August 2017) vertical cross sections of (a) Z_{DR} at 0510-0515 UTC, (b) Z_{DR} at 0515-0520 UTC, (c) K_{DP} at 0510-0515 UTC, (d) K_{DP} at 0515-0520 UTC, (e) ρ_{HV} at 0510-0515 UTC, (f) ρ_{HV} at 0515-0520 UTC. Note that the same W-E oriented cross section as the three previous figures was used. The charge analysis only examines the "big" flashes with at least 250 VHF source points for this particular case. The approximate altitudes of each of the charge layers are denoted by red plus signs and blue minus signs. The 0°C, -10°C, -20°C, -30°C, and -40°C isotherms were extracted from the soundings and overlaid onto each subplot to gain more insight on the hydrometeor size, shape, and phase.

3.1.5. Case 3: 1100-1200 UTC 27 August 2017

The storm environment of Case 3 featured MUCAPE values of 725 J kg^{-1} and precipitable water measured at 6.5 cm thereby indicating a classic tropical profile of primarily shallow convection (Figure 20). The peak VHF source rate of 7,869 src $(5\ min)^{-1}$ as well as the peak VHF source density of 4.6 src km^{-1} $(5\ min)^{-1}$ during Case 3 occurred at around 1100 UTC (Figure 7a). The charge-altitude normalized histogram further communicates the shallow nature of the convection in Case 3 with greater than 75% of the VHF source points located below 9 km (Figure 7b). There was a total of 40,000 sources during this time (mean altitude near 8 km), which is in stark contrast to Case 1 and Case 2. The Hovmoeller diagram of VHF source density and GPM precipitation rate (Figure 7c) shows two regions of source activity extending from approximately 29.5°N to 30°N. The peak rain rate was 17.4 mm hr^{-1} and occurred at the same location and time as the VHF source density maximum at 30°N, which implies that this convection might have been deeper than the convection in the southernmost latitude of 29.5°N. During Case 3, the peak precipitation rate of 53.4 mm hr^{-1} was nearly spatially collocated with the VHF source density hotspot in the deeper convective cell to the north (not shown). Meanwhile, the southern cell had its largest lightning and precipitation regions notably more offset, concurrent with observations that lightning and precipitation tend to be less correlated for shallow convection.

The time series of NLDN flash rate for each type and polarity of flash specified with the overlaid charge analysis completed for Case 3 is displayed in Figure 21. The NLDN recorded a total of 172 flashes during this period, with 37% being +CGs and 5%

being -ICs. While the occurrence of +CG flashes seemed to be substantially higher in Case 3 compared to Case 1 and Case 2, it should be noted that the lightning activity and flash rates were much lower in Case 3. A charge analysis was performed for a total of 62 "big" flashes out of the 133 flashes detected by the HLMA for the whole hour. The largest flash rate reached 17 fl min^{-1}, which was an order of magnitude less than the flash rates calculated in Case 1 and Case 2. However, from 1140 to 1150 UTC, some VHF sources surpassed 12.5 km after a surge in both total and +CG flash rates, prompting a more intensive analysis of the lightning and precipitation microphysics during this 10-minute time frame through the use of polarimetric radar.

The 5-minute timesteps of Z_H and negative Z_{DR} in both plan and cross-sectional views are presented in Figure 22 and Figure 23 with the charge analysis overlaid during the 10-minute period from 1140 to 1150 UTC during Case 3. The zoomed vertical cross sections in Figure 22 and Figure 23 are shown in Figure 24. The plan views portray how widespread the tropical convection is at this time (Figure 22a; Figure 23a), rather than being more concentrated in a central rainband like Case 1 and Case 2. Indeed, the broad and shallow convective identity of Case 3 is reiterated in the vertical cross-sectional profiles with large Z_H values basically confined below the melting level at 0°C (Figure 22b,c; Figure 23b,c; Figure 24). In addition, the Z_H was observed to rapidly decrease with height above the melting level, a characteristic that was identified by Cecil et al. (2002) and Carr et al. (2017) to denote the absence of strong updrafts as there are limited quantities of supercooled water and large frozen hydrometeors. There was still some lightning detected within this stratiform cell, with VHF sources scattered around and

above the melting level near this weak updraft. Some negative Z_{DR} values were located aloft in this region as well as the surrounding areas, indicating there were some vertically-oriented ice crystals in the upper-levels of this environment. While there could be an underlying warm-cloud charging mechanism active here, it is proposed that these ice particles could have either been detrained from the updraft cores of nearby deep convection or produced through slight increases in updraft strength. The charge structure maintained its inverted tripole as seen previously with Case 1 and Case 2, with a lower negative layer initially near 4.8 km, a main positive layer at 8.7 km, and an upper negative layer at 10.8 km (Figure 22d). With time, the charge layers rose in altitude and the positive layer got notably denser, suggesting that the storm was undergoing intensification and lofting mixed-phase hydrometeors higher up in the cloud (Figure 23d). This claim is verified through an increase in magnitude of Z_H, and VHF sources increasing in quantity with time within the cell (Figure 22a,b,c; Figure 23a,b,c; Figure 24).

Vertical cross sections of Z_{DR}, K_{DP}, and ρ_{HV} with the estimated altitudes of each charge layer overlaid from 1140 to 1150 UTC within Case 3 are shown in Figure 25. In general, the highest Z_{DR} values did not exceed 2 dB and the highest K_{DP} values ranged from 0.75-1.75 deg km^{-1}, and these peak values did not surpass the melting level at 4.65 km (Figure 25a,b,c,d). Although the Z_{DR} and K_{DP} values were lower in both quantity and altitude compared to Case 1 and Case 2, these values were more extensive, which was likely the source of the tremendous rainfall accumulations throughout the spatial domain during this time. The spatial extent of negative values of Z_{DR} and K_{DP} aloft grew with

time and these regions coincided with decreased values of ρ_{HV} which was consistent with the growth in lightning activity measured during this 10-minute period (Figure 25e,f). Nevertheless, these regions of radar-indicated lightning occurrence were not exactly aligned with the shallow convective cell of focus near 94.5°W, so it is unclear whether these mixed-phase particles participated in the lightning activity nearby or if an independent electrification method was developing within this stratiform convection. All three of the charge layers resided within the mixed-phase region from 0°C to -40°C (i.e., 4.65 to 11.72 km). The "bright band" signature was most pronounced in this case with a near continuous trend of local maximum Z_{DR} and local minimum ρ_{HV} values within the melting layer characterized by the stratiform precipitation regime.

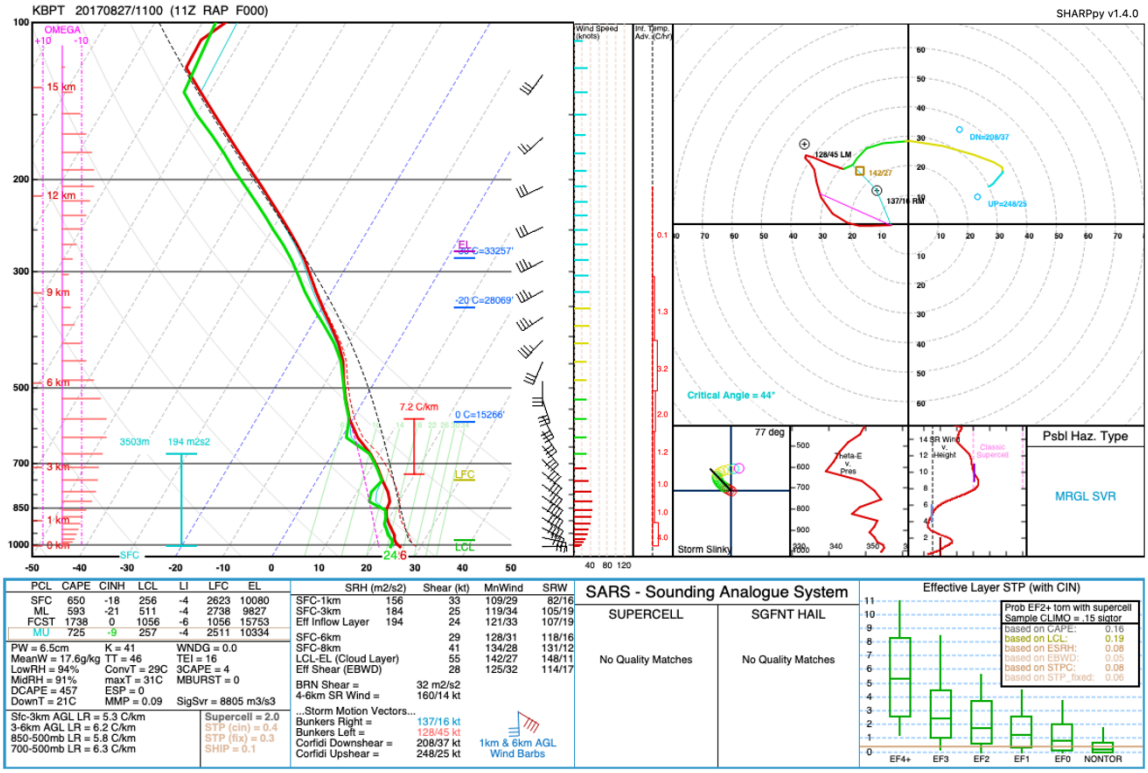

Figure 20: Forecast RAP sounding at 1100 UTC 27 August 2017 (initialized at 1100 UTC) at KBPT.

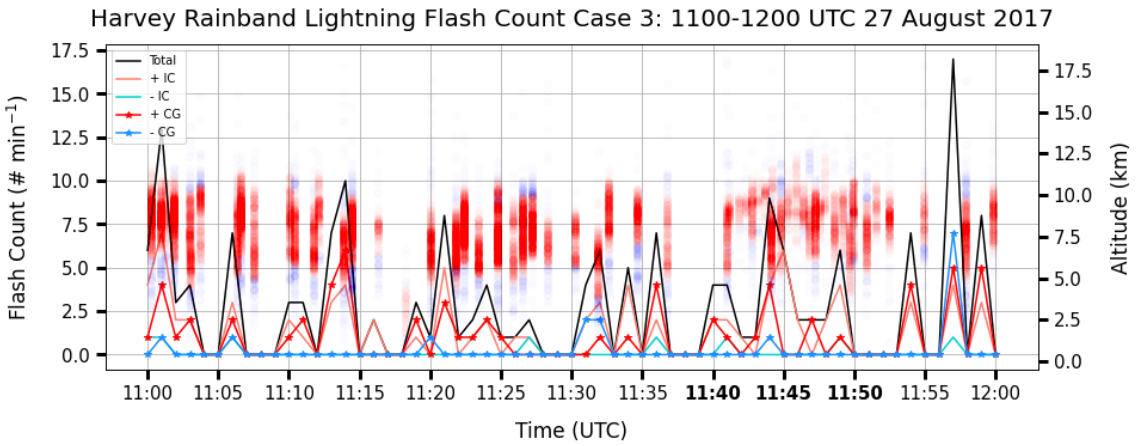

Figure 21: Hurricane Harvey Case 3 NLDN flash rate (# min^{-1}) time series with the corresponding charge analysis utilizing both HLMA and NLDN datasets overlaid. In addition to the total NLDN flash rate, the +IC, -IC, +CG, and -CG flash rates are displayed as well. The red dots represent the positive sources while the blue dots represent the negative sources within each lightning flash, and each source dot is plotted at the location of its respective altitude in km. Note that only the flashes and sources within the outer rainband of focus are included. The charge analysis only examines the "big" flashes with at least 75 VHF source points for this particular case. The times of the 10-minute period that will be analyzed further using polarimetric radar observations are in bold.

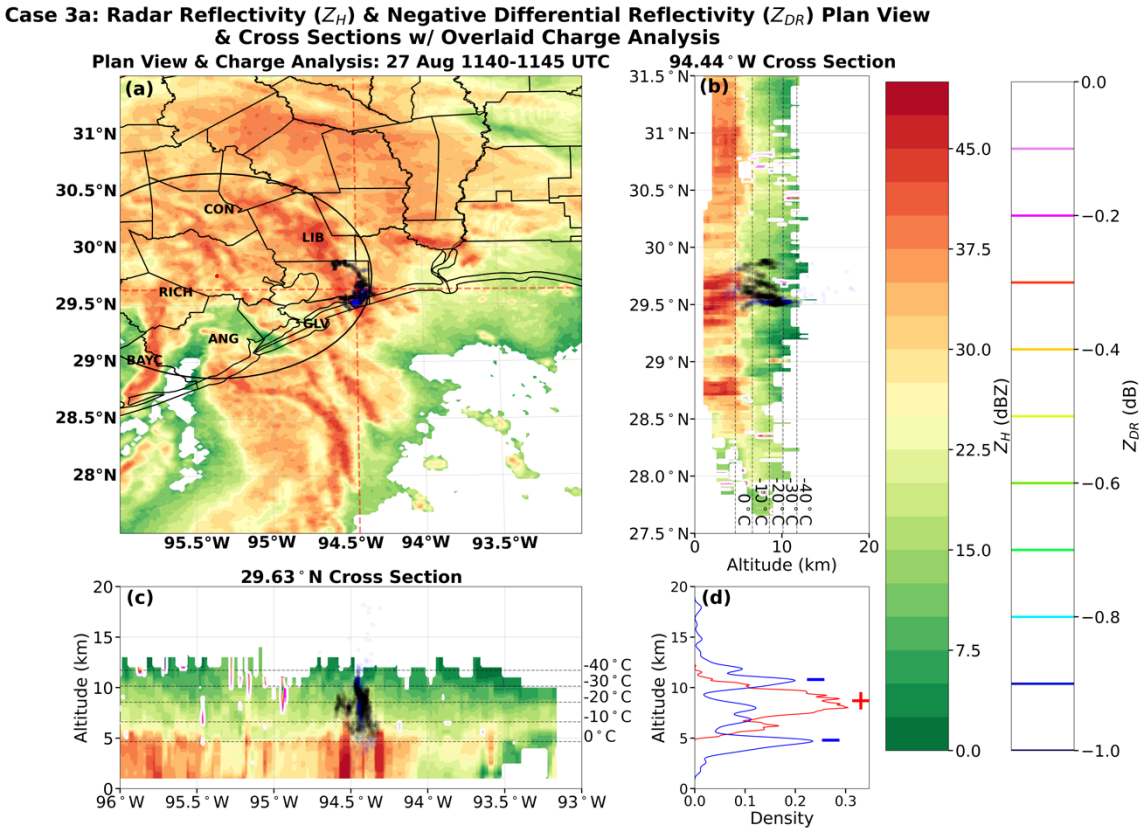

Figure 22: 1140-1145 UTC 27 August 2017 plots of (a) NEXRAD composite (column maximum) radar reflectivity (Z_H) plan view with overlaid charge analysis, (b) N-S 94.44°W longitude cross section with both negative Z_{DR} (colored contours) and charge analysis overlaid, (c) W-E 29.63°N latitude cross section with both negative Z_{DR} (colored contours) and charge analysis overlaid, (d) altitude kernel density estimation (KDE) of positive and negative HLMA source counts. The charge analysis only examines the "big" flashes with at least 75 VHF source points for this particular case. Positive sources are represented by black dots, while negative sources are represented by the blue dots. The black circle in (a) illustrates the 100-km radius of detection of the HLMA network, and Houston, Texas, the center of the HLMA network, is marked by the red dot. The dotted red vertical and horizontal lines in (a) show where the cross sections were drawn. The 0°C, -10°C, -20°C, -30°C, and -40°C isotherms were extracted from the sounding and overlaid onto (b) and (c) to gain more insight on the hydrometeor size, shape, and phase. The approximate altitudes of each of the charge layers are denoted by red plus signs and blue minus signs in (d).

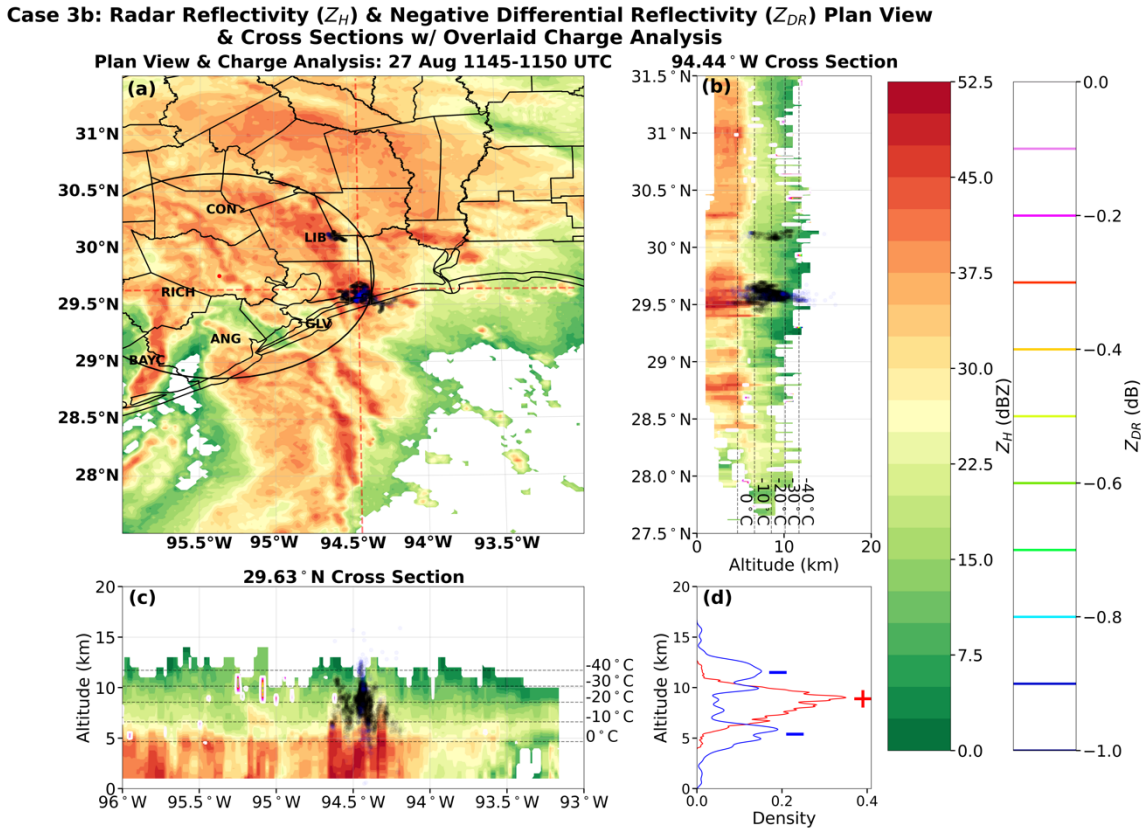

Figure 23: 1145-1150 UTC 27 August 2017 plots of (a) NEXRAD composite (column maximum) radar reflectivity (Z_H) plan view with overlaid charge analysis, (b) N-S 94.44°W longitude cross section with both negative Z_{DR} (colored contours) and charge analysis overlaid, (c) W-E 29.63°N latitude cross section with both negative Z_{DR} (colored contours) and charge analysis overlaid, (d) altitude kernel density estimation (KDE) of positive and negative HLMA source counts. The charge analysis only examines the "big" flashes with at least 75 VHF source points for this particular case. Positive sources are represented by black dots, while negative sources are represented by the blue dots. The black circle in (a) illustrates the 100-km radius of detection of the HLMA network, and Houston, Texas, the center of the HLMA network, is marked by the red dot. The dotted red vertical and horizontal lines in (a) show where the cross sections were drawn. The 0°C, -10°C, -20°C, -30°C, and -40°C isotherms were extracted from the sounding and overlaid onto (b) and (c) to gain more insight on the hydrometeor size, shape, and phase. The approximate altitudes of each of the charge layers are denoted by red plus signs and blue minus signs in (d).

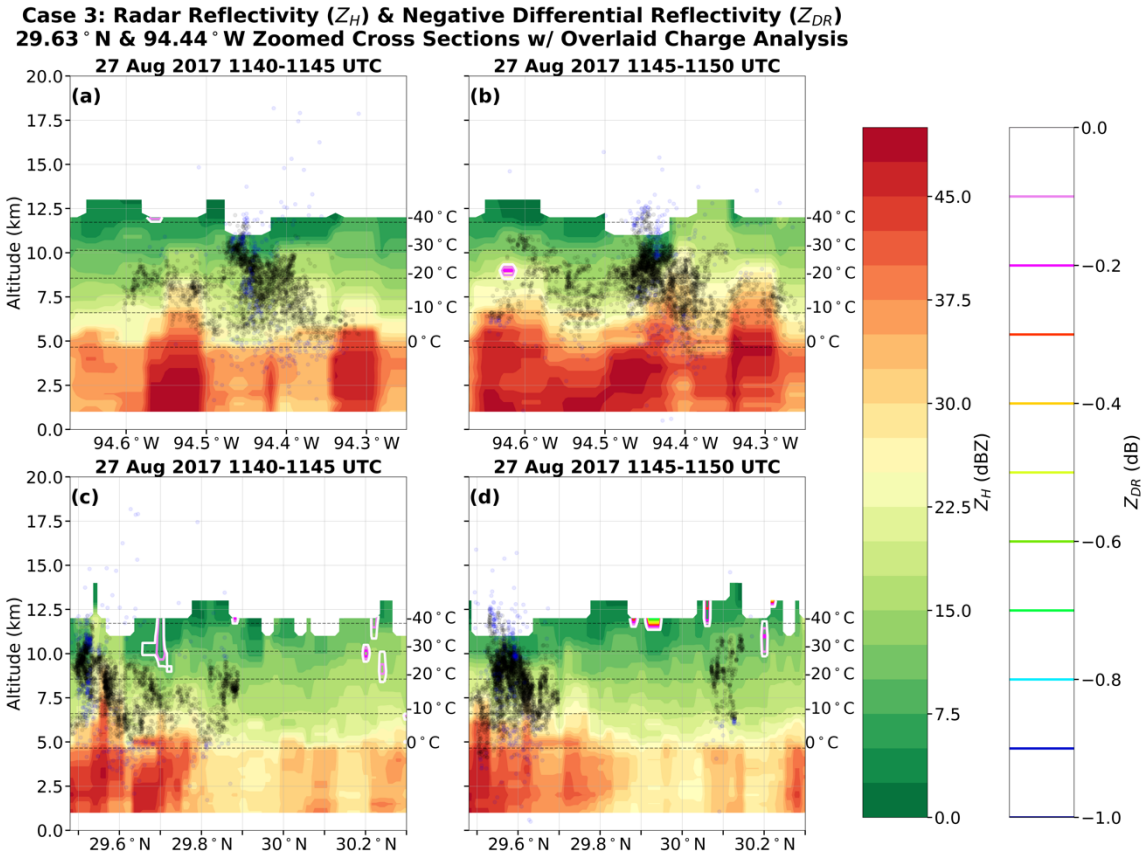

Figure 24: Case 3 (1140-1150 UTC 27 August 2017) zoomed vertical cross sections with both negative Z_{DR} (colored contours) and charge analysis overlaid at (a) W-E 29.63°N latitude from 1140-1145 UTC, (b) W-E 29.63°N latitude from 1145-1150 UTC, (c) N-S 94.44°W longitude from 1140-1145 UTC, (d) N-S 94.44°W longitude from 1145-1150 UTC. The charge analysis only examines the "big" flashes with at least 75 VHF source points for this particular case. Positive sources are represented by black dots, while negative sources are represented by the blue dots. The 0°C, -10°C, -20°C, -30°C, and -40°C isotherms were extracted from the sounding and overlaid onto each subplot to gain more insight on the hydrometeor size, shape, and phase.

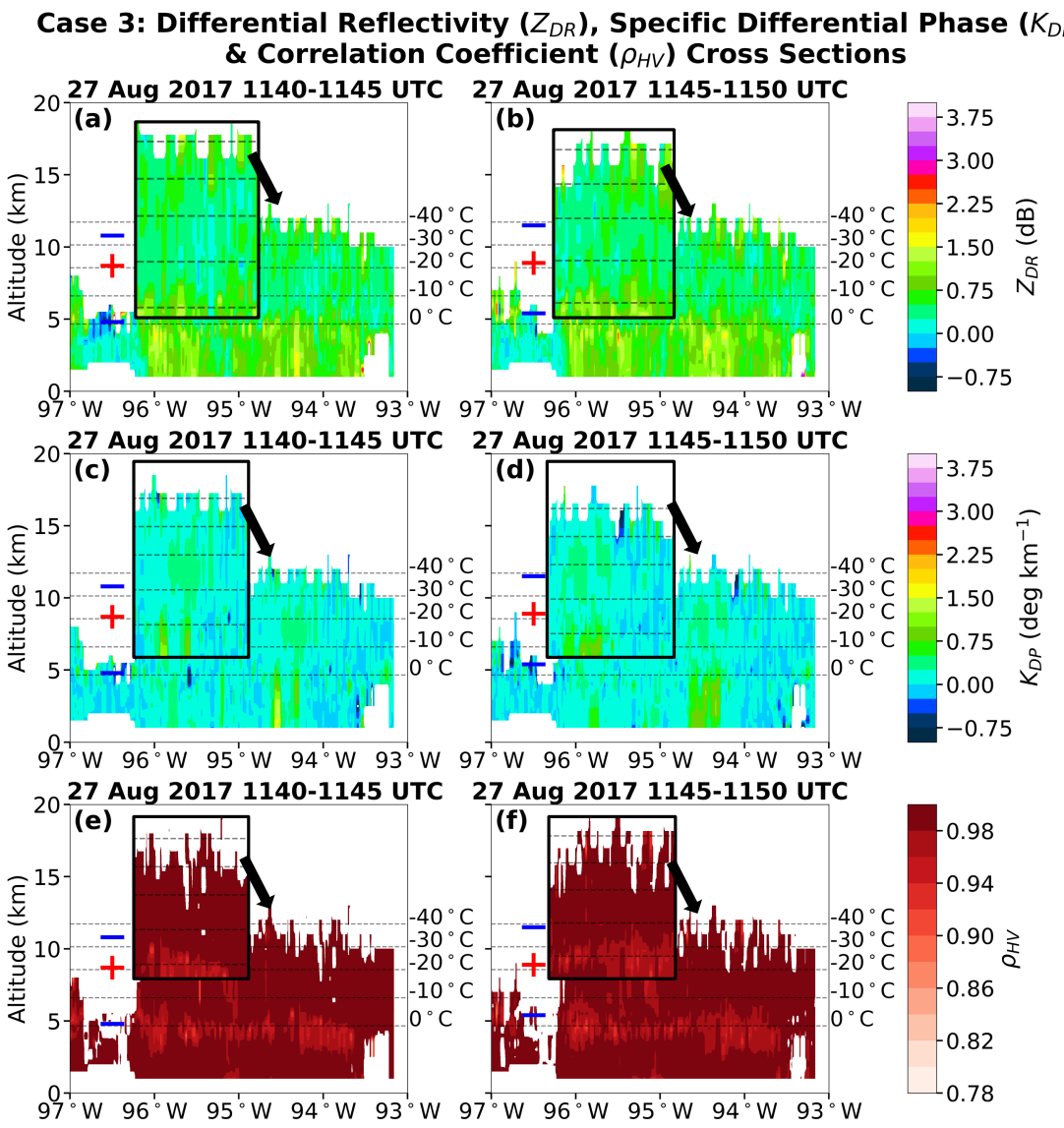

Figure 25: Case 3 (1140-1150 UTC 27 August 2017) vertical cross sections of (a) Z_{DR} at 1140-1145 UTC, (b) Z_{DR} at 1145-1150 UTC, (c) K_{DP} at 1140-1145 UTC, (d) K_{DP} at 1145-1150 UTC, (e) ρ_{HV} at 1140-1145 UTC, (f) ρ_{HV} at 1145-1150 UTC. Note that the same W-E oriented cross section as the three previous figures was used. The charge analysis only examines the "big" flashes with at least 75 VHF source points for this particular case. The approximate altitudes of each of the charge layers are denoted by red plus signs and blue minus signs. The 0°C, -10°C, -20°C, -30°C, and -40°C isotherms were extracted from the soundings and overlaid onto each subplot to gain more insight on the hydrometeor size, shape, and phase.

3.2. Hurricane Nicholas (2021)

3.2.1. Event Background and Environmental Conditions

Hurricane Nicholas originated as a tropical wave that emerged off the west coast of Africa on 28 August 2021 (Latto and Berg 2022). As the disturbance moved westward across the tropical North Atlantic basin and Caribbean Sea through 8 September, the associated convection remained disorganized. However, once the system traversed across Central America on 9 September, a trough developed over the western Caribbean Sea that would eventually travel northwestward into the Gulf of Mexico early on 12 September, generating a well-defined low-level circulation with more organized convection. By 1200 UTC 12 September, Nicholas reached tropical storm status and continued to move generally northwestward for the next 24 hours around a subtropical ridge located over the southeastern United States. Although the system became disorganized at times due to the presence of moderate vertical wind shear, Nicholas proceeded to strengthen within the moist and unstable environment in the warm Gulf waters. There were also a series of unexpected reformations of the cyclone center that preceded the period of rapid intensification of Nicholas, with the northward shifts in the system causing it to accelerate its track. Nicholas became a Category 1 hurricane at 0000 UTC 14 September and made landfall a few hours later at 0530 UTC in Matagorda County, Texas with maximum sustained winds of 33 m s^{-1} and a minimum central pressure of 991 mb.

As Hurricane Nicholas travelled inland, it weakened and was downgraded to a tropical storm by 1200 UTC 14 September as it approached southwestern Houston. In

contrast to Hurricane Harvey, there was not a stationary boundary in the vicinity of Nicholas that influenced its behavior (Figure 26; Figure 27), yet the forward motion of the system slowed around landfall as the steering flow surrounding the cyclone started to break down. Therefore, the heaviest rainfall in southeast Texas occurred after landfall with widespread rainfall amounts of 101.6 to 228.6 mm (4 to 9 in) throughout the region, but there were no direct deaths in Texas and damage was estimated at $1 billion in the United States from Nicholas. Nicholas quickly weakened over land as it gradually moved northeastward and became a remnant low by 1800 UTC 15 September. The full progression of the tropical cyclone track is shown in Figure 28.

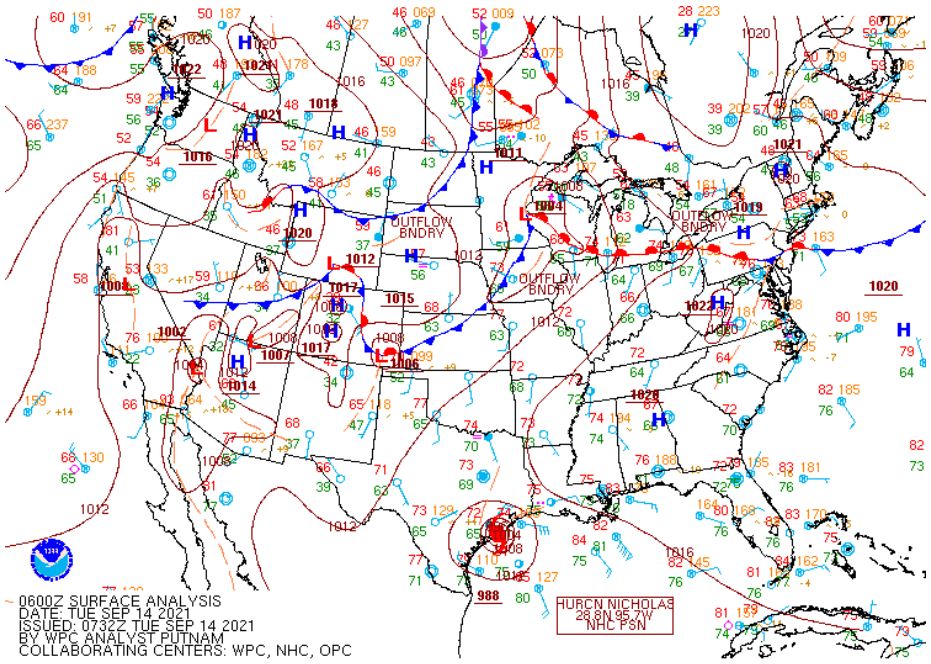

Figure 26: WPC surface analysis valid for 14 September 2021 at 0600 UTC.

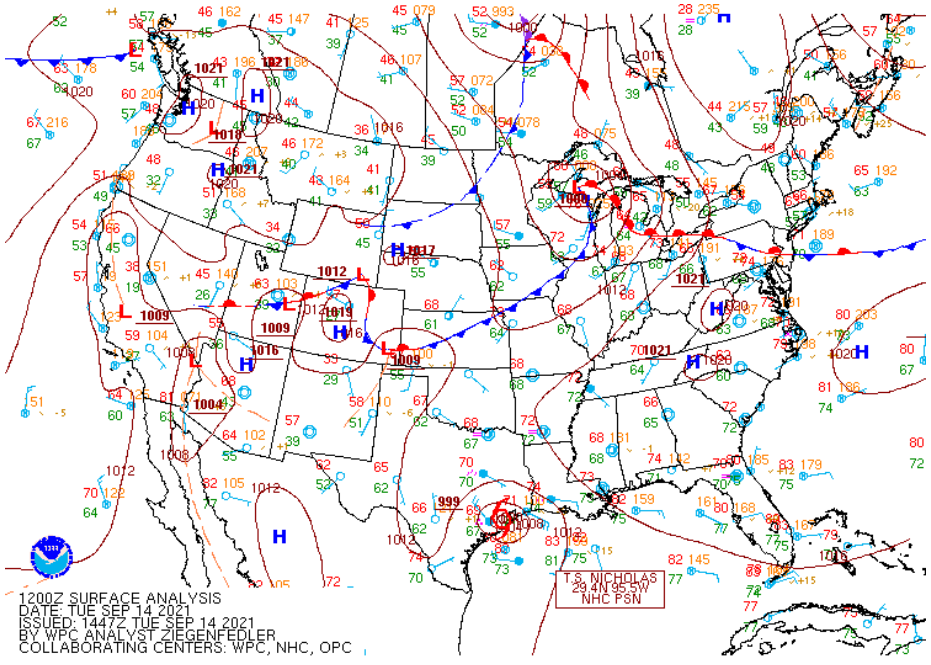

Figure 27: WPC surface analysis valid for 14 September 2021 at 1200 UTC.

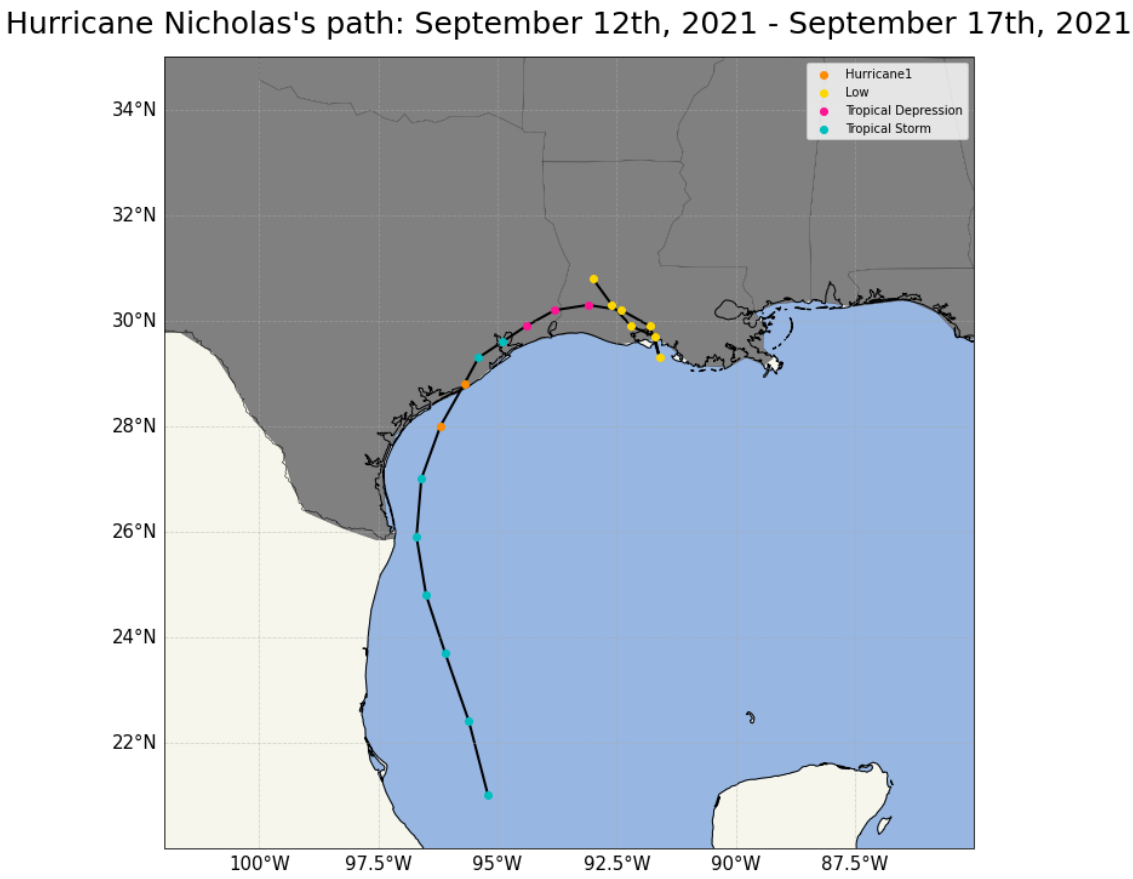

Figure 28: Hurricane database (HURDAT2) best track positions for Hurricane Nicholas from 12 September 2021 to 17 September 2021 showing the temporal and categorical evolution of the tropical cyclone. Note that points are spaced in 6-h time increments.

3.2.2. Lightning and Precipitation Overview

Figure 29 shows the plan view of flash extent density with contoured GPM precipitation rate for the outer rainbands during the nine-hour period from 0000 UTC 14 September 2021 to 0900 UTC 14 September 2021, which featured the landfall and journey of Nicholas into southeast Texas. Note that the remainder of the progression of the tropical cyclone over land was excluded from the period of focus in an effort to analyze only the oceanic feeder bands. The peak time-averaged flash extent density

measured during the period within the study domain was approximately 14 fl km^{-2} min^{-1}, while the peak time-averaged rain rate was 36.9 mm hr^{-1}. The two case studies were distinct in flash extent density maxima and were located offshore. Both case studies were noticeably spatially offset from the highest precipitation rate contours, yet Case 2 (the northernmost flash extent density hotspot located offshore between Chambers County and Jefferson County) had its maximum flash extent density and precipitation values exceptionally more offset than those of Case 1.

The time series of HLMA lightning flash rate and GPM precipitation rate for the outer rainbands during the nine-hour period of interest is displayed in Figure 30. It is apparent that the bulk of the lightning activity within the feeder bands occurred prior to landfall, especially from 0200 to 0300 UTC. The peak spatially-averaged flash rate of 28 fl min^{-1} occurred at 0250 UTC. Conversely, the peak spatially-averaged rain rate of roughly 6.5 mm hr^{-1} was observed at 0000 UTC, revealing that the highest rainfall rate preceded the strongest lightning activity by a few hours. In accordance with the lightning and precipitation characteristics associated with each case seen in Figure 29, Figure 30 also exhibited extreme lightning and rainfall rates for Case 1 but moderate lightning and weak rain rates in Case 2.

Figure 31 shows the spatiotemporal relationships between lightning and precipitation in the outer rainbands from 0000 to 0900 UTC 14 September 2021 during Hurricane Nicholas. From 0000 to 0215 UTC, the period affiliated with Case 1, lightning was active in the feeder bands (Figure 31a). The lightning ceased in the outer rainbands from 0215 to 0715 UTC, aside from some minor activity during 0500 to 0700

UTC once Nicholas made landfall. From 0715 to 0815 UTC, the feeder bands became electrically-active once again before moving onshore. Contrary to Case 2, Case 1 consisted of a small cluster of high-altitude source densities reaching 15 km, most notably from 0000 to 0100 UTC. However, the highest VHF source rate for the nine-hour period occurred during Case 2 around 0800 UTC with 3,250 src $(5\ min)^{-1}$. The largest VHF source density was 1.4 src km^{-1} $(5\ min)^{-1}$.

Figure 31b shows that the mean altitudes of both cases were similarly shallow with Case 1 only being 0.1 km higher than Case 2, despite the presence of its higher-altitude VHF sources. The peak rain rate was located near 28.9°N at 22.5 mm hr^{-1}, which occurred between 0700 and 0800 UTC during Case 2 (Figure 31c). The largest precipitation rates and VHF source densities shifted northward with time from 28.5°N to close to 29°N, which was representative of the transition between both case studies. The largest lightning and precipitation regions were more spatially aligned for Case 2 than Case 1 in Figure 31d (a key contrast with the plan view plot in Figure 29). Additional examination of the lightning-precipitation microphysics within both separate case studies is crucial to determine the true nature of these tropical convective feeder bands.

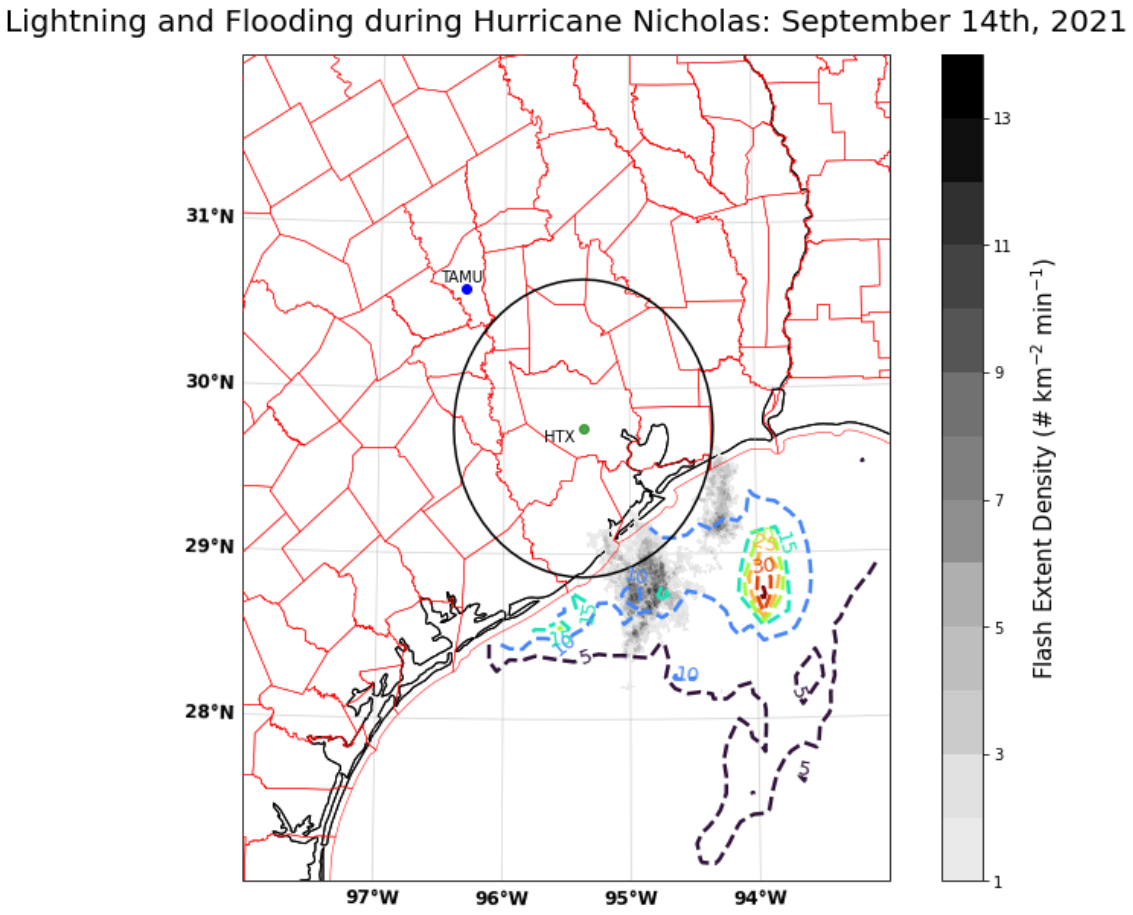

Figure 29: Plan view of flash extent density (black filled contours; # km^{-2} min^{-1}) with GPM precipitation rate (colored contours; mm hr^{-1}) overlaid for 0000 UTC 14 September 2021 to 0900 UTC 14 September 2021 during Hurricane Nicholas. Note that the ocean-only values for lightning and precipitation are exhibited in an effort to only examine the outer rainbands. The flash extent density and GPM rain rate are averaged through time for the nine-hour period. The black circle illustrates the 100-km radius of detection of the HLMA network. Houston (HTX) and Texas A&M University (TAMU) are represented by the green and blue dots, respectively.

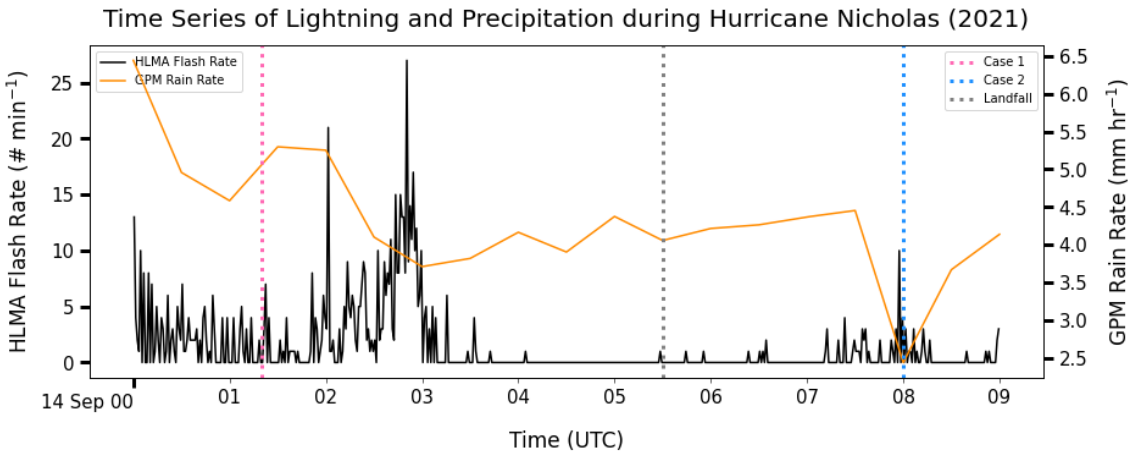

Figure 30: Time series of HLMA flash rate (# min^{-1}) denoted by the black line and GPM precipitation rate (mm hr^{-1}) denoted by the orange line from 0000 UTC 14 September 2021 to 0900 UTC 14 September 2021 during Hurricane Nicholas. The times of the selected 10-minute case studies and landfall are marked by the dotted vertical lines. Note that the ocean-only values for lightning and precipitation are exhibited in an effort to only examine the outer rainbands. All flashes, big or small, are included in the HLMA lightning flash rate dataset. The HLMA flash rate and GPM rain rate was calculated for the spatially-averaged rectangular domain of 98°W, 27°N, 93°W, 32°N.

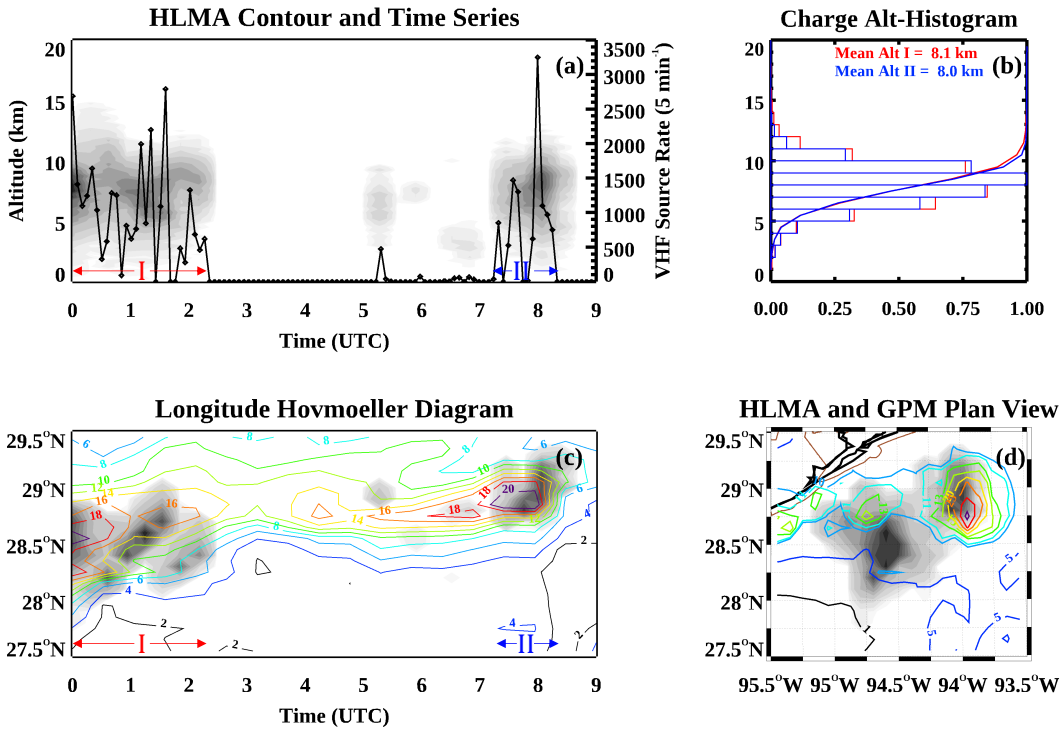

Figure 31: 0000 to 0900 UTC 14 September 2021 plots of (a) HLMA VHF source density (black filled contours) and VHF source rate (black line; # [5 min^{-1}]) time-altitude series, (b) charge altitude normalized histogram with mean altitude and cumulative distribution function line denoted for each case, (c) longitude-averaged Hovmoeller diagram of HLMA VHF source density (black filled contours) and GPM precipitation rate (colored contours; mm hr^{-1}), (d) plan view of HLMA VHF source density (black filled contours) and GPM precipitation rate (colored contours; mm hr^{-1}). Note that the ocean-only values for lightning and precipitation are exhibited in an effort to only examine the outer rainbands.

3.2.3. Case 1: 0000-0215 UTC 14 September 2021

High-altitude VHF sources persisted around 15 km, and as these source densities diminished aloft, a sharp spike in the VHF source rate was observed (Figure 31a). The 0100 UTC RAP forecast sounding showed MUCAPE values at 2,265 J kg^{-1} and precipitable water values at 6.9 cm (Figure 32). Therefore, the convection that initiated

in this environment had adequate instability and moisture to support a powerful updraft. Additionally, there was some evidence of a low-level VHF source layer around 6-7 km attempting to form between 0100 to 0200 UTC, implying there could be a secondary microphysical process such as rime splintering or fragmentation due to ice-ice collisions (e.g., Qu et al. 2022) present during this time. The largest VHF source rate of 2,790 src $(5\ min)^{-1}$ was at 0140 UTC when a lower-altitude charge layer developed, while the largest VHF source density of 1.4 src km^{-1} $(5\ min)^{-1}$ occurred at the beginning of the period. The total number of VHF sources detected was 27,629 in Case 1, with a mean altitude of 8.1 km (Figure 31b). With about 75% of these sources situated below 9 km, this tropical convection was relatively shallow. The Hovmoeller diagram revealed that VHF source density exhibited many hotspots through time that were generally centered around 28.5°N (Figure 31c). The highest precipitation rates were initially focused at 28.3°N and 28.5°N, but as time evolved, the heavy rainfall became concentrated solely at 28.5°N. The peak VHF source density was at around 0120 UTC and the peak rain rate was during the first 45 minutes of the time frame, revealing that the highest precipitation slightly preceded the highest lightning activity. An overall spatial collocation between lightning and precipitation for Case 1 was demonstrated with the maxima in VHF source density (13.3 src km^{-2}) and GPM rainfall rate (33.9 mm hr^{-1}) in the same region of embedded intense convection (not shown).

The NLDN observed a quantity of 553 flashes, which 35% were +CGs and 7% were -ICs (Figure 33). The charge analysis was completed for a total of 65 “big” flashes, a large fraction of the 162 flashes detected by the HLMA during this case study. The

highest total lightning flash rate was 24 fl min^{-1} at the beginning of the time frame when higher-altitude lightning activity was rampant, yet there were instances when flash rates increased later in the period. One of these notable occasions was from 0115 to 0125 UTC, when not only were the +CG flash rate quite energetic, but the highest -IC flash rate occurred during this time. This 10-minute period containing inverted polarity flash rates was analyzed further using polarimetric radar variables to better understand the lightning-precipitation microphysics of this oceanic feeder band.

The 5-minute timesteps of Z_H and negative Z_{DR} in both plan and cross-sectional views with the charge analysis overlaid during the 10-minute period from 0115 to 0125 UTC during Case 1 are shown in Figure 34 and Figure 35. The zoomed vertical cross sections in Figure 34 and Figure 35 are shown in Figure 36. The somewhat disorganized structure of the oceanic rainband is evident (Figure 34a; Figure 35a) with the outer rainband of focus intertwined within broad, shallow convection spanning throughout the Gulf waters. Some robust eyewall convection can also be viewed to the west of the convective feeder bands. The vigor of the oceanic rainband is verified in the vertical cross sections with the 30 dBZ Z_H echo extending up to 10 km (Figure 34b,c; Figure 35b,c; Figure 36). In addition, negative Z_{DR} values appeared frequently above the updraft core, signifying the presence of vertically-oriented ice particles. Note that negative Z_{DR} values can also be seen from 96.25°W to 95.25°W where the eyewall convection resided, implying that the eyewall may have been electrified as well. As time progressed, the convection seemed to intensify with Z_H increasing within the updraft, Z_{DR} becoming more negative in the upper-levels of the storm, and VHF sources

accumulating throughout the feeder band indicating an enhancement in cloud electrification. The charge analysis confirmed anomalous lightning activity with a charge structure resembling an inverted tripole (Figure 34d; Figure 35d). The lower negative layer was estimated to be located around 5 km, the middle positive layer was around 7 km, and the upper negative layer was near 10 km. With time, the upper negative layer grew denser, while the positive and negative layers below became less dense, so it is postulated that the cloud and precipitation particles were lofted upwards by the stronger updraft, building up the upper-levels of the cloud.

Figure 37 shows vertical cross sections of Z_{DR}, K_{DP}, and ρ_{HV} with the approximate altitudes of each charge layer overlaid from 0115 to 0125 UTC within Case 1. While the largest Z_{DR} values of 0.75-1.50 dB remained below the melting level at 4.8 km, there was an extension of these values past the 0°C isotherm with a pocket of elevated Z_{DR} values exceeding 1.5 dB located above the height of the -10°C isotherm that rose in altitude with time (Figure 37a,b). This result is consistent with the hypothesis that hydrometeors were being lofted to higher altitudes by an updraft (similar to Figure 34 and Figure 35). In conjunction with this region of heightened Z_{DR}, K_{DP} values close to 0 deg km^{-1} and ρ_{HV} values below 0.96 were observed (Figure 37c,d,e,f). A similar feature was observed by Didlake and Kumjian (2017) in the downshear right quadrant of tropical cyclones, which indicated that this represented a layer of pristine ice particles such as planar ice crystals that rapidly grow in moisture-rich environments involving convective precipitation. The vertical profile of K_{DP} noticeably increased with time below the melting layer from K_{DP} values up to 2 deg km^{-1} to $K_{DP} > 2.25$ deg km^{-1},

suggesting that heavy precipitation was indeed prevalent during this time. There were negative values of Z_{DR} and K_{DP} detected aloft within the charge layers, especially from -10°C to -30°C, and these negative values spread outwards to surrounding areas with time. Lower values of ρ_{HV} were found collocated with these areas of negative Z_{DR} and K_{DP}, and near the melting layer of nearby regions, which translates to potential cloud electrification processes and the existence of melting ice particles that were likely advected away from the convective updraft, respectively.

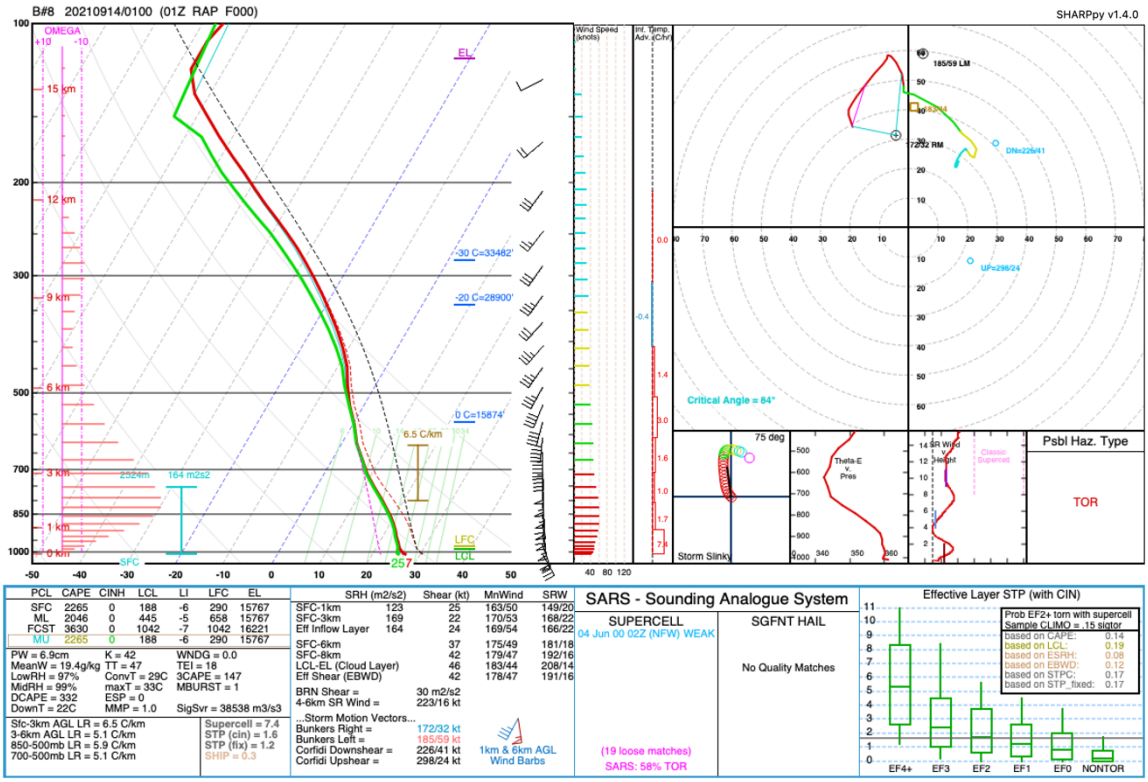

Figure 32: Forecast RAP sounding at 0100 UTC 14 September 2021 (initialized at 0100 UTC) at Buoy B#8.

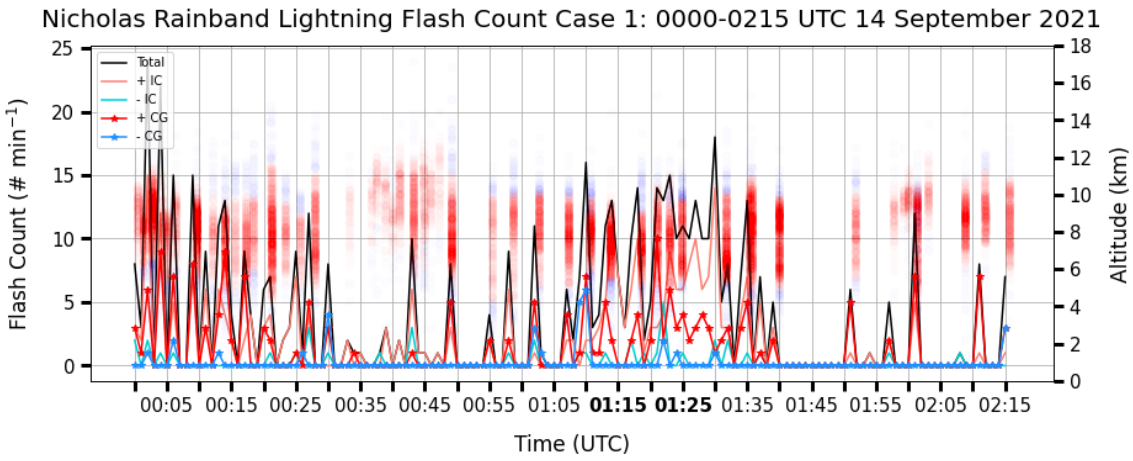

Figure 33: Hurricane Nicholas Case 1 NLDN flash rate (# min^{-1}) time series with the corresponding charge analysis utilizing both HLMA and NLDN datasets overlaid. In addition to the total NLDN flash rate, the +IC, -IC, +CG, and -CG flash rates are displayed as well. The red dots represent the positive sources while the blue dots represent the negative sources within each lightning flash, and each source dot is plotted at the location of its respective altitude in km. Note that only the flashes and sources within the outer rainband of focus are included. The charge analysis only examines the "big" flashes with at least 75 VHF source points for this particular case. The times of the 10-minute period that will be analyzed further using polarimetric radar observations are in bold.

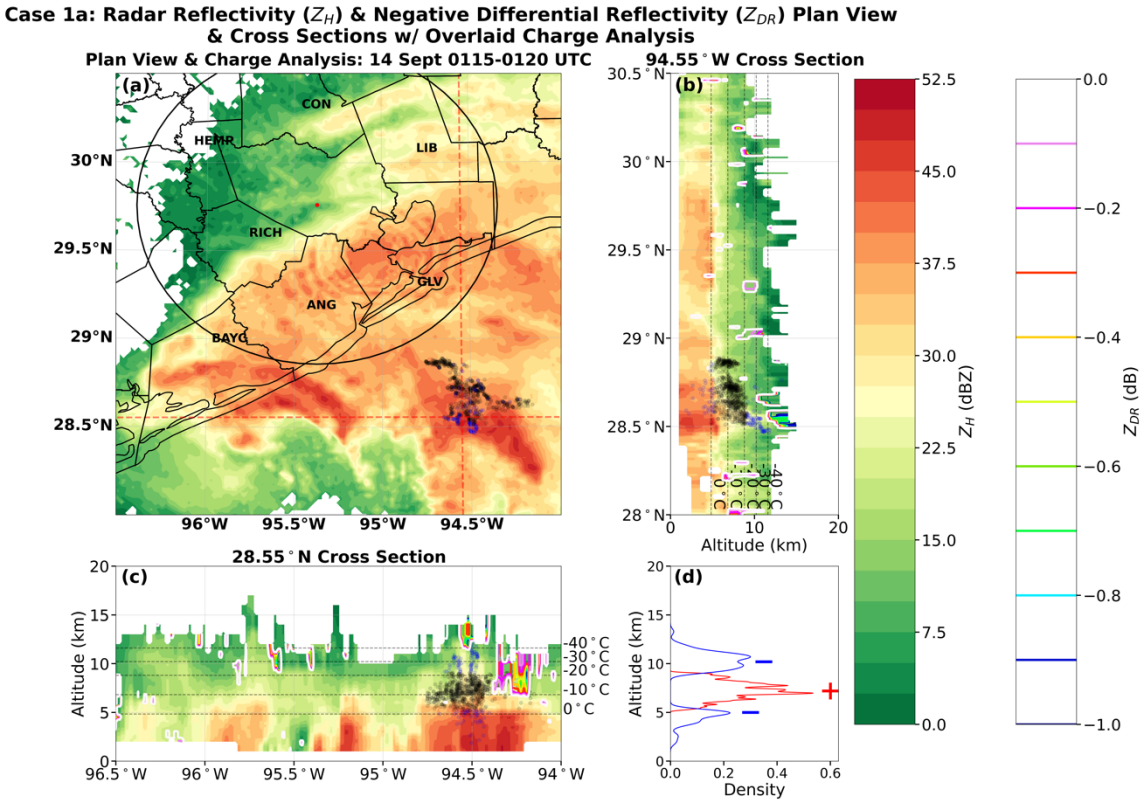

Figure 34: 0115-0120 UTC 14 September 2021 plots of (a) NEXRAD composite (column maximum) radar reflectivity (Z_H) plan view with overlaid charge analysis, (b) N-S 94.55°W longitude cross section with both negative Z_{DR} (colored contours) and charge analysis overlaid, (c) W-E 28.55°N latitude cross section with both negative Z_{DR} (colored contours) and charge analysis overlaid, (d) altitude kernel density estimation (KDE) of positive and negative HLMA source counts. The charge analysis only examines the "big" flashes with at least 75 VHF source points for this particular case. Positive sources are represented by black dots, while negative sources are represented by the blue dots. The black circle in (a) illustrates the 100-km radius of detection of the HLMA network, and Houston, Texas, the center of the HLMA network, is marked by the red dot. The dotted red vertical and horizontal lines in (a) show where the cross sections were drawn. The 0°C, -10°C, -20°C, -30°C, and -40°C isotherms were extracted from the sounding and overlaid onto (b) and (c) to gain more insight on the hydrometeor size, shape, and phase. The approximate altitudes of each of the charge layers are denoted by red plus signs and blue minus signs in (d).

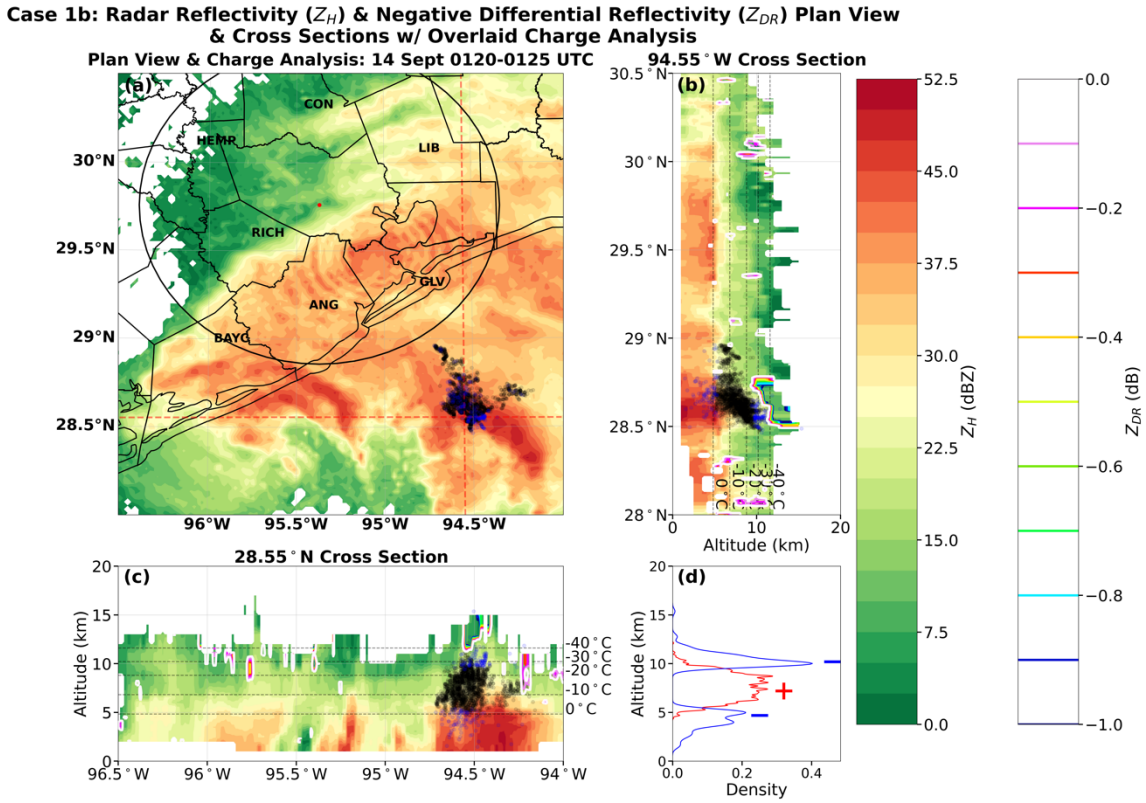

Figure 35: 0120-0125 UTC 14 September 2021 plots of (a) NEXRAD composite (column maximum) radar reflectivity (Z_H) plan view with overlaid charge analysis, (b) N-S 94.55°W longitude cross section with both negative Z_{DR} (colored contours) and charge analysis overlaid, (c) W-E 28.55°N latitude cross section with both negative Z_{DR} (colored contours) and charge analysis overlaid, (d) altitude kernel density estimation (KDE) of positive and negative HLMA source counts. The charge analysis only examines the "big" flashes with at least 75 VHF source points for this particular case. Positive sources are represented by black dots, while negative sources are represented by the blue dots. The black circle in (a) illustrates the 100-km radius of detection of the HLMA network, and Houston, Texas, the center of the HLMA network, is marked by the red dot. The dotted red vertical and horizontal lines in (a) show where the cross sections were drawn. The 0°C, -10°C, -20°C, -30°C, and -40°C isotherms were extracted from the sounding and overlaid onto (b) and (c) to gain more insight on the hydrometeor size, shape, and phase. The approximate altitudes of each of the charge layers are denoted by red plus signs and blue minus signs in (d).

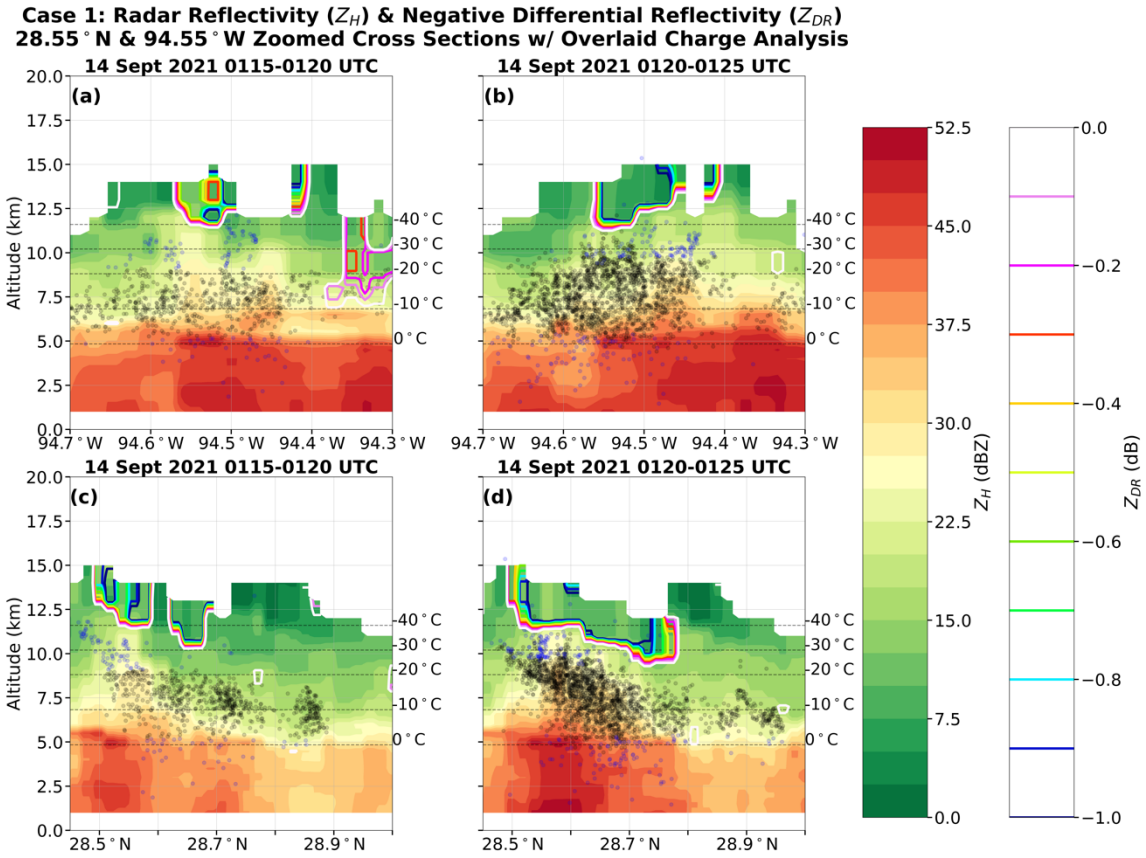

Figure 36: Case 1 (0115-0125 UTC 14 September 2021) zoomed vertical cross sections with both negative Z_{DR} (colored contours) and charge analysis overlaid at (a) W-E 28.55°N latitude from 0115-0120 UTC, (b) W-E 28.55°N latitude from 0120-0125 UTC, (c) N-S 94.55°W longitude from 0115-0120 UTC, (d) N-S 94.55°W longitude from 0120-0125 UTC. The charge analysis only examines the "big" flashes with at least 75 VHF source points for this particular case. Positive sources are represented by black dots, while negative sources are represented by the blue dots. The 0°C, -10°C, -20°C, -30°C, and -40°C isotherms were extracted from the sounding and overlaid onto each subplot to gain more insight on the hydrometeor size, shape, and phase.

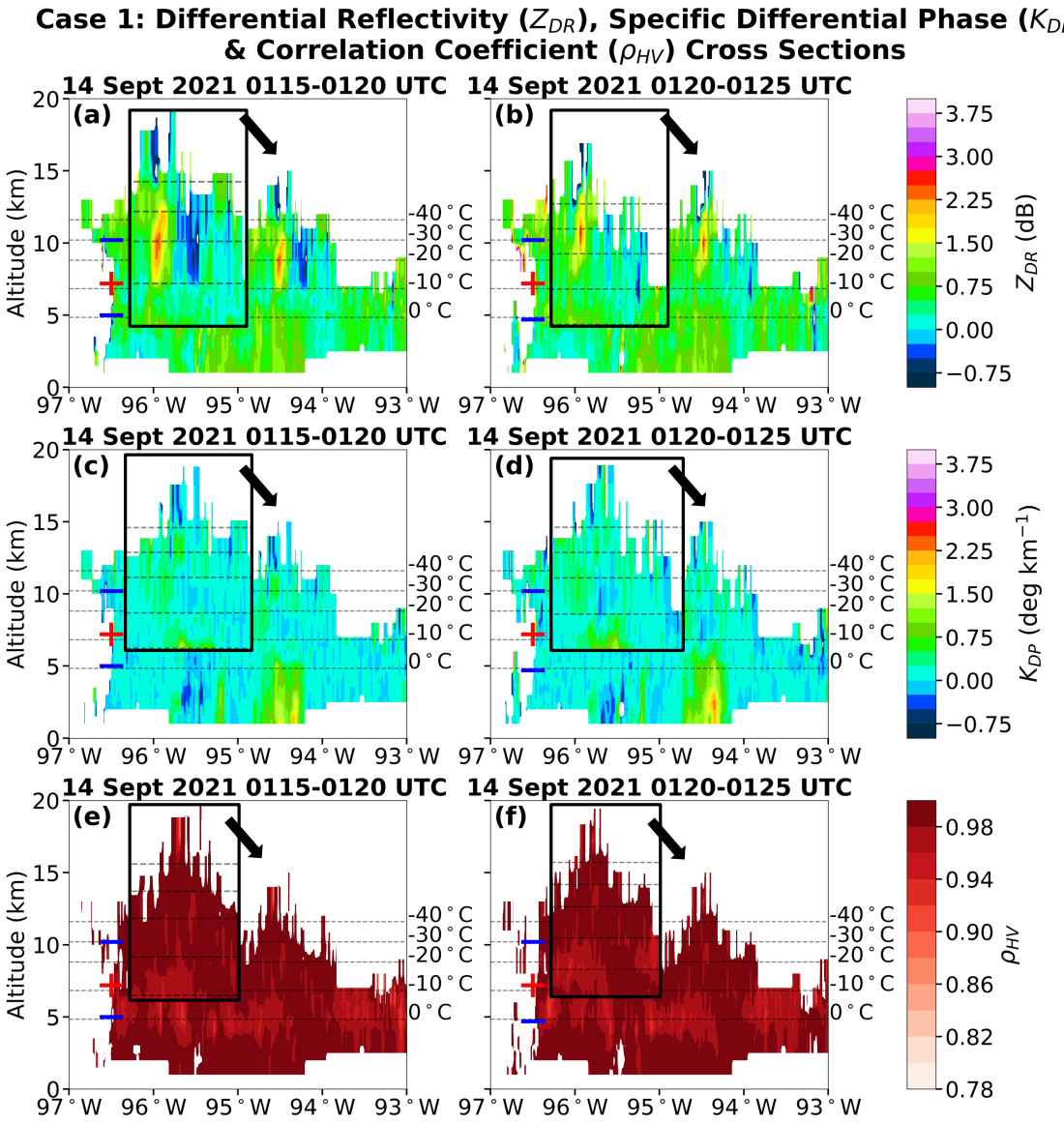

Figure 37: Case 1 (0115-0125 UTC 14 September 2021) vertical cross sections of (a) Z_{DR} at 0115-0120 UTC, (b) Z_{DR} at 0120-0125 UTC, (c) K_{DP} at 0115-0120 UTC, (d) K_{DP} at 0120-0125 UTC, (e) ρ_{HV} at 0115-0120 UTC, (f) ρ_{HV} at 0120-0125 UTC. Note that the same W-E oriented cross section as the three previous figures was used. The charge analysis only examines the "big" flashes with at least 75 VHF source points for this particular case. The approximate altitudes of each of the charge layers are denoted by red plus signs and blue minus signs. The 0°C, -10°C, -20°C, -30°C, and -40°C isotherms were extracted from the soundings and overlaid onto each subplot to gain more insight on the hydrometeor size, shape, and phase.

3.2.4. Case 2: 0715-0815 UTC 14 September 2021

In relation to Case 1, the time-altitude series demonstrated that high-altitude lightning was even more sparse in Case 2 with VHF source densities mainly concentrated below 10 km (Figure 31a), which was evidenced by lower MUCAPE values at 1,208 J kg^{-1} for the comparatively weaker updraft (Figure 38). Nonetheless, a lower layer of VHF sources appeared to form below 5 km around 0800 UTC during which the highest VHF source rate of 3250 src $(5\ min)^{-1}$ and largest Case 2 VHF source density of 1.1 src km^{-1} $(5\ min)^{-1}$ occurred (Figure 31a). The charge altitude normalized histogram revealed the mean altitude of the 10,897 VHF sources identified during the case study to be 8.0 km, which was similar to Case 1 with around 75% of the sources located below 9 km (Figure 31b). The Hovmoeller diagram depicted two relative maxima in VHF source density that shifted slightly northward with time to near 29°N (Figure 31c). In contrast, the peak GPM precipitation rate of 22.5 mm hr^{-1} was centered in between the two lightning hotspots and persisted for the whole case study. A high spatial correlation between lightning and precipitation during Case 2 was observed with the highest rain rate of 92.4 mm hr^{-1} and largest VHF source density of 11.9 src km^{-2} in the vicinity of each other (not shown). It is clear that Case 2 presented more centralized lightning and precipitation activity that was intense yet short-lived, while Case 1 displayed a broad area of lightning and rainfall that was more episodic over a long duration of time.

Figure 39 shows the time series of NLDN flash rate of each type and polarity of lightning with the charge analysis executed for Case 2 overlaid. During the hour-long

case study, the NLDN measured a total of 180 flashes with 21% being +CGs and 12% being -ICs. A charge analysis was performed for a total of 22 “big” flashes. The majority of the flashes were large during this case study, as the HLMA detected 35 flashes overall. Concurrent with the observations in the previous case studies, an increase in the flash rate was associated with increased VHF source detection at higher heights. For the first 30 minutes of the case study, only lightning flashes of positive polarity were observed. By 0745 UTC, both -IC and -CG flashes developed as well. From 0755 to 0805 UTC, flash rates of all type and polarity quickly escalated, and the highest total flash rate of the time period was recorded during this time at 14 fl min^{-1}. Thus, this 10-minute period highlighting storm intensification was examined more thoroughly using polarimetric radar.

Figure 40 and Figure 41 display 5-minute timesteps of Z_H and negative Z_{DR} in plan and cross-sectional views with the charge analysis during the 10-minute period from 0755 to 0805 UTC during Case 2. The zoomed vertical cross sections in Figure 40 and Figure 41 are shown in Figure 42. The layout of the oceanic feeder band is seen distinctly in Z_H contoured on the plan views (Figure 40a; Figure 41a) within widespread, stratiform convection. Again, the eyewall convection can be discerned over land to the west, yet it appeared particularly less intense now than it previously did in Case 1 prior to landfall. Convection was considerably turbulent during the first 5 minutes with Z_H surpassing 45 dBZ above the melting level at 0°C (roughly 5.2 km), negative Z_{DR} values located aloft within the convective region implying ice particles available for electrification, and extensive coverage of VHF sources throughout the horizontal and

vertical extent of the outer rainband (Figure40a,b,c; Figure 42a,c). However, the oceanic convection weakened as time evolved with Z_H values decreasing overall, shrinking negative Z_{DR} region aloft, and fewer VHF sources (Figure 41a,b,c; Figure 42b,d). This discovery is consistent with the results of Figure 39, as the second 5-minute timestep experienced a sharp downtick in flash rate signaling that the storm diminished in strength during this time. At this time, the updraft sufficiently weakened thereby enhancing gravitational sedimentation which caused the hydrometeors in the upper-levels of the cloud to subsequently fall through the cloud towards the melting layer. The anomalous inverted tripole present in Case 1 was still apparent during Case 2 with a lower negative layer near 5 km, a main positive layer near 9 km, and an upper negative layer around 11 km (Figure 40d; Figure 41d).

The vertical cross sections of Z_{DR}, K_{DP}, and ρ_{HV} along with the rough altitudes of each charge layer overlaid from 0755 to 0805 UTC within Case 2 are presented in Figure 43. The largest Z_{DR} values (0.75-1.75 dB) and K_{DP} values (0.75 to 1.5 deg km^{-1}) were confined below the melting level, but notable values of Z_{DR} near 1.5 dB and K_{DP} near 0.75 deg km^{-1} were located above the 0°C isotherm during the first 5-minute timestep when the updraft was more vigorous (Figure 43a,b,c,d). In general, the Z_{DR} and K_{DP} values were lower than those of Case 1, but K_{DP} appeared to increase with time below the melting layer indicating heavy rainfall. The intensity of the rainfall was verified with lower ρ_{HV} values (Figure 43e,f) near the surface coinciding with the updraft marked by large values of Z_{DR} and K_{DP}, indicating a wider drop size spectrum. Negative values of Z_{DR} and K_{DP} were examined above the updraft core, and the appearance of these

negative quantities decreased with time, hinting at the reduced electrification. There were some negative K_{DP} values evident at the lower levels in the cloud, which could be a signature of the ice particles falling to lower heights. While the decreased ρ_{HV} values still coincided with areas of negative Z_{DR} and K_{DP}, the feature was not as pronounced as the earlier case studies, likely owing to the moderate lightning activity present here (Figure 43e,f). The "bright band" illuminated the melting level with reduced ρ_{HV} values, but there was a noticeable break in this trend where the convective updraft was located, separating it from the shallow convection. Nevertheless, ρ_{HV} values were smaller near the melting layer during the second 5-minute timestep when the falling ice crystals were likely melting to raindrops and contributing to the surface precipitation.

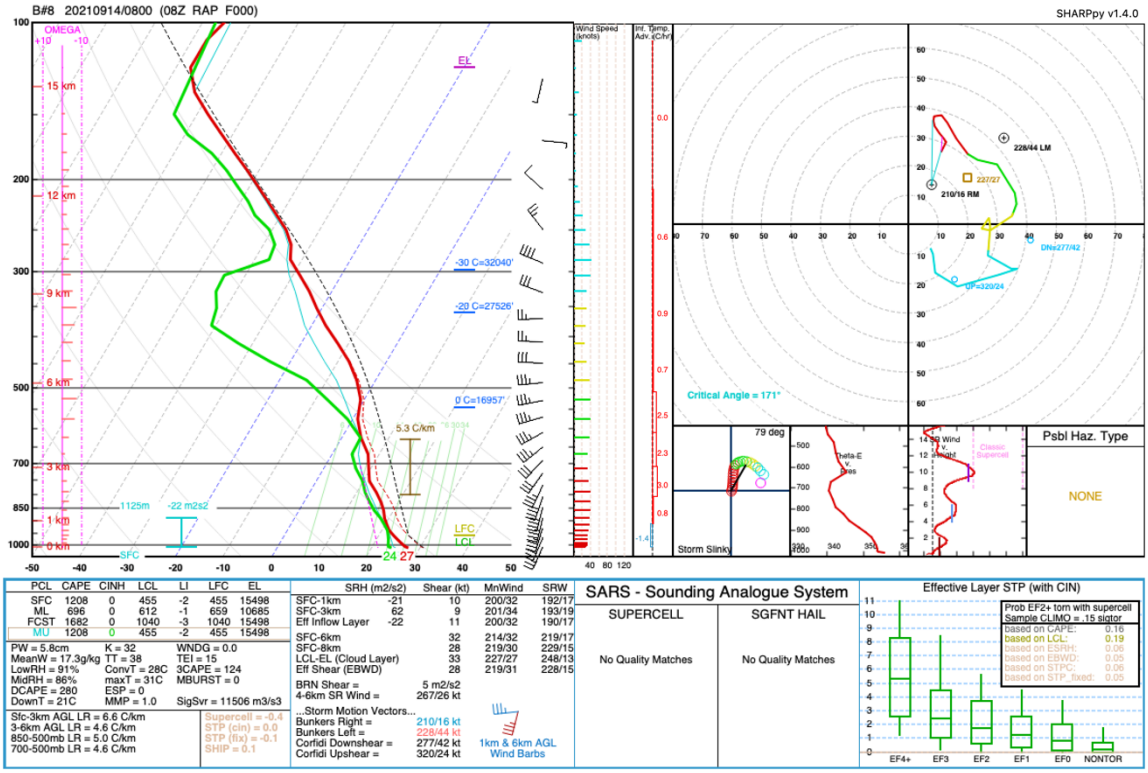

Figure 38: Forecast RAP sounding at 0800 UTC 14 September 2021 (initialized at 0800 UTC) at Buoy B#8.

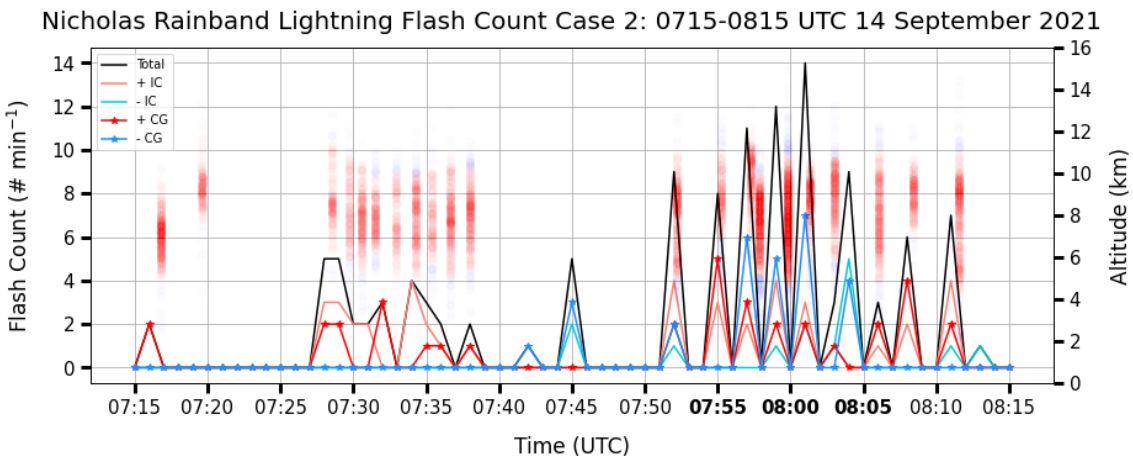

Figure 39: Hurricane Nicholas Case 2 NLDN flash rate (# min^{-1}) time series with the corresponding charge analysis utilizing both HLMA and NLDN datasets overlaid. In addition to the total NLDN flash rate, the +IC, -IC, +CG, and -CG flash rates are displayed as well. The red dots represent the positive sources while the blue dots represent the negative sources within each lightning flash, and each source dot is plotted at the location of its respective altitude in km. Note that only the flashes and sources within the outer rainband of focus are included. The charge analysis only examines the "big" flashes with at least 75 VHF source points for this particular case. The times of the 10-minute period that will be analyzed further using polarimetric radar observations are in bold.

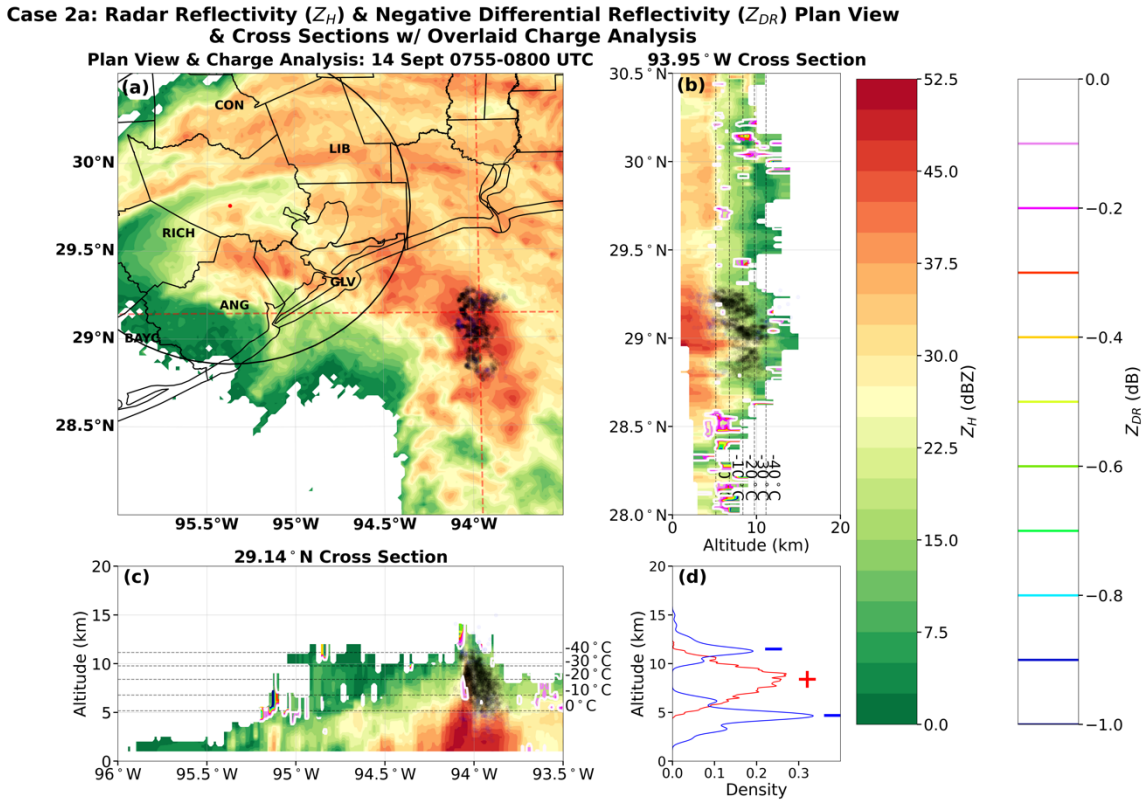

Figure 40: 0755-0800 UTC 14 September 2021 plots of (a) NEXRAD composite (column maximum) radar reflectivity (Z_H) plan view with overlaid charge analysis, (b) N-S 93.95°W longitude cross section with both negative Z_{DR} (colored contours) and charge analysis overlaid, (c) W-E 29.14°N latitude cross section with both negative Z_{DR} (colored contours) and charge analysis overlaid, (d) altitude kernel density estimation (KDE) of positive and negative HLMA source counts. The charge analysis only examines the "big" flashes with at least 75 VHF source points for this particular case. Positive sources are represented by black dots, while negative sources are represented by the blue dots. The black circle in (a) illustrates the 100-km radius of detection of the HLMA network, and Houston, Texas, the center of the HLMA network, is marked by the red dot. The dotted red vertical and horizontal lines in (a) show where the cross sections were drawn. The 0°C, -10°C, -20°C, -30°C, and -40°C isotherms were extracted from the sounding and overlaid onto (b) and (c) to gain more insight on the hydrometeor size, shape, and phase. The approximate altitudes of each of the charge layers are denoted by red plus signs and blue minus signs in (d).

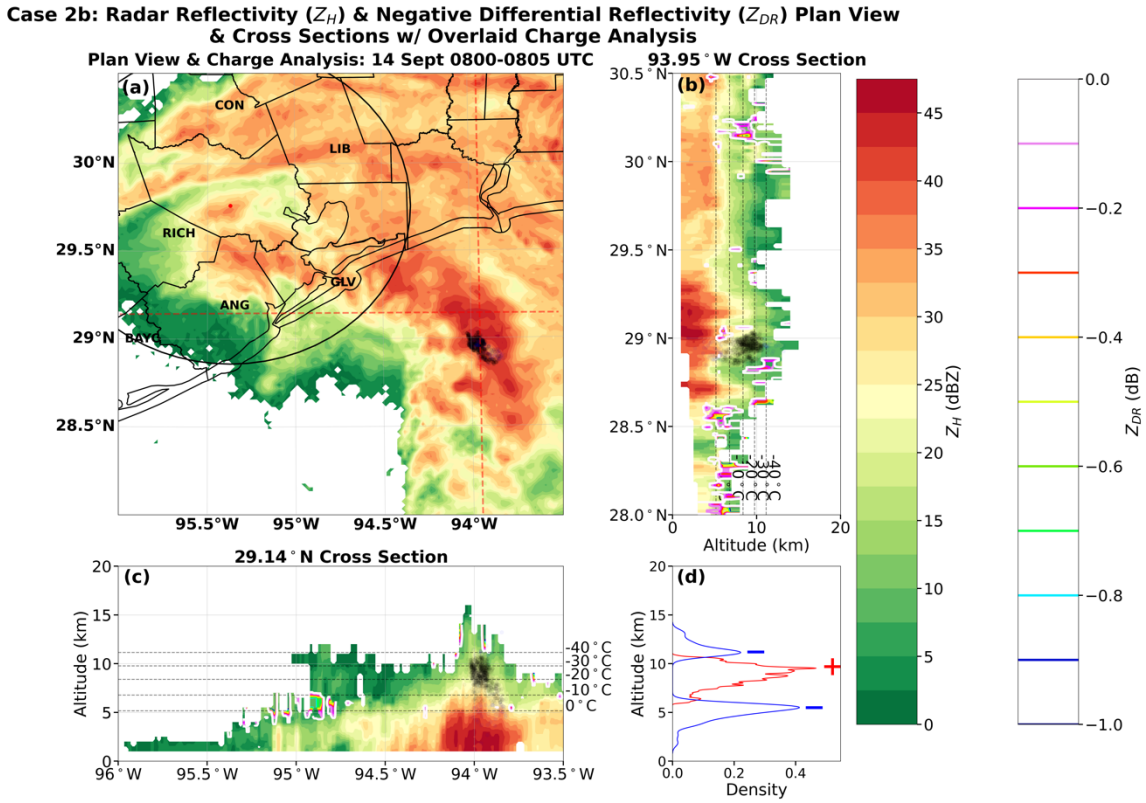

Figure 41: 0800-0805 UTC 14 September 2021 plots of (a) NEXRAD composite (column maximum) radar reflectivity (Z_H) plan view with overlaid charge analysis, (b) N-S 93.95°W longitude cross section with both negative Z_{DR} (colored contours) and charge analysis overlaid, (c) W-E 29.14°N latitude cross section with both negative Z_{DR} (colored contours) and charge analysis overlaid, (d) altitude kernel density estimation (KDE) of positive and negative HLMA source counts. The charge analysis only examines the "big" flashes with at least 75 VHF source points for this particular case. Positive sources are represented by black dots, while negative sources are represented by the blue dots. The black circle in (a) illustrates the 100-km radius of detection of the HLMA network, and Houston, Texas, the center of the HLMA network, is marked by the red dot. The dotted red vertical and horizontal lines in (a) show where the cross sections were drawn. The 0°C, -10°C, -20°C, -30°C, and -40°C isotherms were extracted from the sounding and overlaid onto (b) and (c) to gain more insight on the hydrometeor size, shape, and phase. The approximate altitudes of each of the charge layers are denoted by red plus signs and blue minus signs in (d).

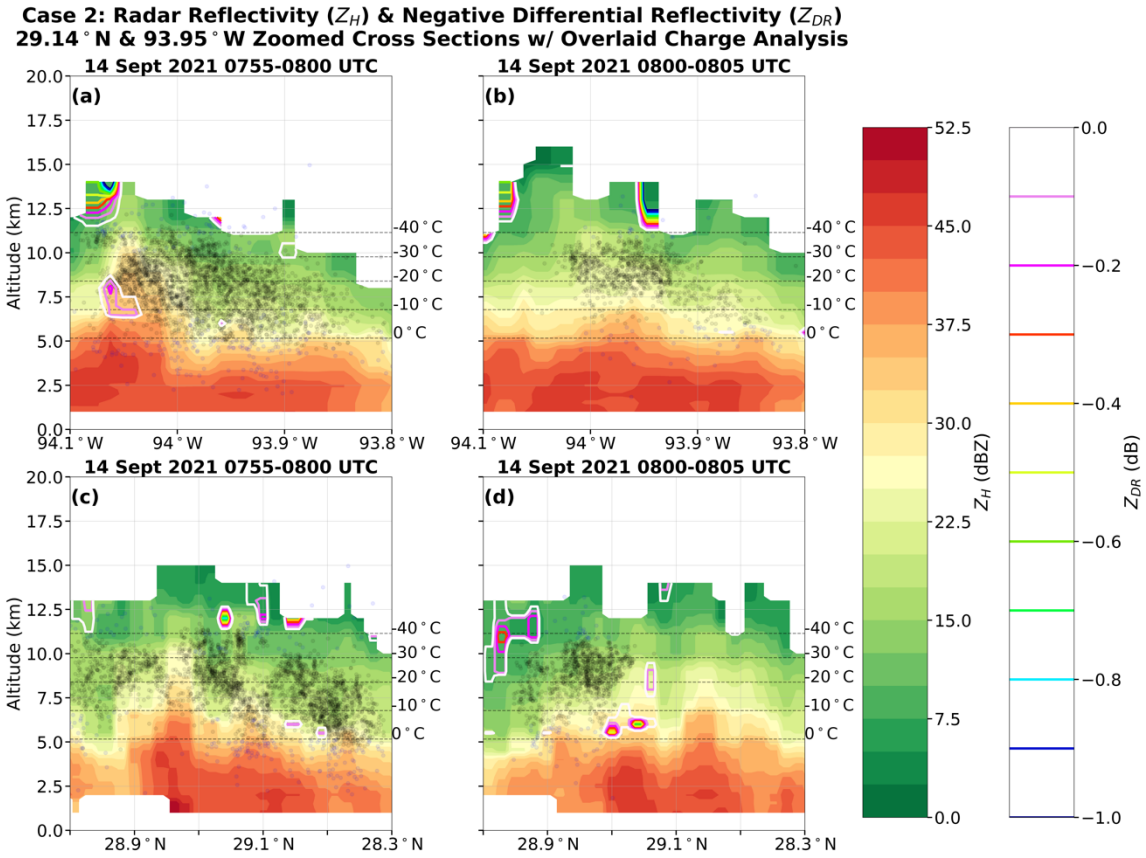

Figure 42: Case 2 (0755-0805 UTC 14 September 2021) zoomed vertical cross sections with both negative Z_{DR} (colored contours) and charge analysis overlaid at (a) W-E 29.14°N latitude from 0755-0800 UTC, (b) W-E 29.14°N latitude from 0800-0805 UTC, (c) N-S 93.95°W longitude from 0755-0800 UTC, (d) N-S 93.95°W longitude from 0800-0805 UTC. The charge analysis only examines the "big" flashes with at least 75 VHF source points for this particular case. Positive sources are represented by black dots, while negative sources are represented by the blue dots. The 0°C, -10°C, -20°C, -30°C, and -40°C isotherms were extracted from the sounding and overlaid onto each subplot to gain more insight on the hydrometeor size, shape, and phase.

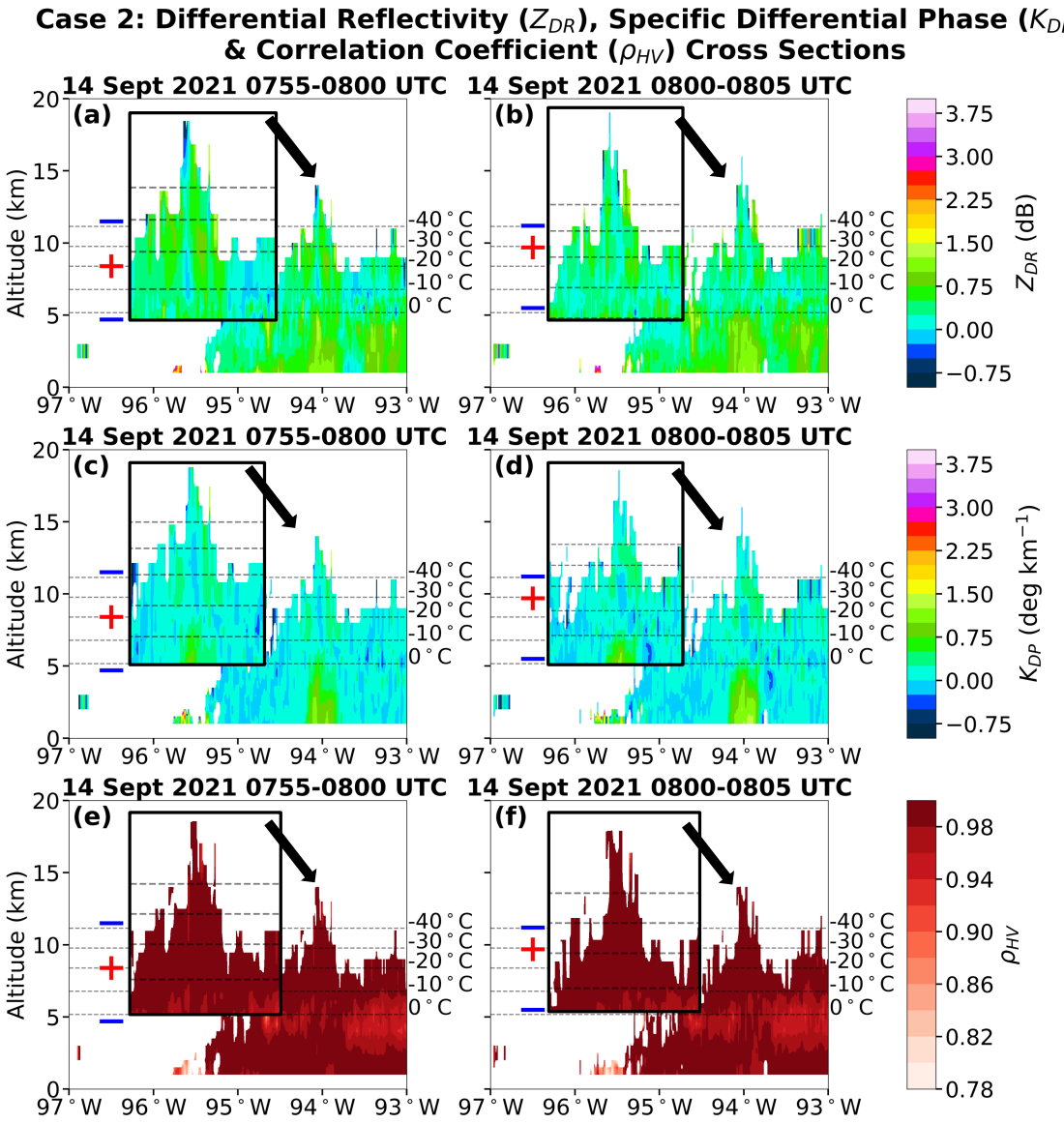

Figure 43: Case 2 (0755-0805 UTC 14 September 2021) vertical cross sections of (a) Z_{DR} at 0755-0800 UTC, (b) Z_{DR} at 0800-0805 UTC, (c) K_{DP} at 0755-0800 UTC, (d) K_{DP} at 0800-0805 UTC, (e) ρ_{HV} at 0755-0800 UTC, (f) ρ_{HV} at 0800-0805 UTC. Note that the same W-E oriented cross section as the three previous figures was used. The charge analysis only examines the "big" flashes with at least 75 VHF source points for this particular case. The approximate altitudes of each of the charge layers are denoted by red plus signs and blue minus signs. The 0°C, -10°C, -20°C, -30°C, and -40°C isotherms were extracted from the soundings and overlaid onto each subplot to gain more insight on the hydrometeor size, shape, and phase.

3.3. Intercomparison of lightning-precipitation behavior within the rainbands of Harvey and Nicholas

While Hurricane Harvey and Hurricane Nicholas both rapidly intensified ahead of making landfall in southeast Texas, the two tropical cyclones manifested varying behavior in terms of their lightning and precipitation. Figure 44 provides the spatial and temporal features of lightning and precipitation in the outer rainbands as well as the eyewall of Harvey on 26 August 2017. Figure 44a emphasizes the clear separation between the lightning activity of the eyewall and rainband regions. It should be noted that the eyewall VHF source rate was multiplied by 10,000 to enable its comparison between the VHF source rate with the outer rainbands. It is evident that the outer rainbands were significantly more electrically-active than the eyewall before and after Harvey's landfall, as the eyewall VHF source rate only exhibited small values below 5 src $(5\ \text{min})^{-1}$ from 0100 to 0400 UTC until its lightning activity essentially ceased for the remainder of the day. This tendency for lightning to be more common in the outer rainbands rather than the eyewall agrees with the findings of Cecil et al. (2002), Fierro et al. (2015), Hu et al. (2020), and Solorzano et al. (2018). Although lightning was active in the outer rainbands all day, the peak rainband VHF source rate occurred long after landfall around 1500 UTC at about 60,000 src $(5\ \text{min})^{-1}$. Figure 44b shows that the mean altitude of the eyewall VHF sources (9.6 km) appeared to be higher than that of the rainband (8.6 km). Given that the eyewall was located outside the HLMA centroid of 100% detection efficiency, fewer low-level eyewall sources could be detected, causing the mean altitude to be higher than it was in reality. In addition, this result likely

stemmed from the high spatial variability in the outer rainbands due to the mixture of deep and shallow convection present there. The Hovmoeller (Figure 44c) and plan view (Figure 44d) of VHF source density and GPM precipitation rate demonstrates the overall spatial collocation between the highest lightning and precipitation for the eyewall and outer rainbands, yet portions of the outer rainbands had the largest lightning and precipitation areas offset where stratiform convection was likely occurring. There was a northward shift in the locations of peak rain rate with time when the heavy rainfall became concentrated only within the outer rainbands (Figure 44c).

Figure 45 is similar to Figure 44 but shows the spatiotemporal relationships between lightning and precipitation in the outer rainbands and eyewall during Hurricane Nicholas's landfall on 0530 UTC 14 September 2021. In direct contrast to Hurricane Harvey, Hurricane Nicholas had the bulk of its lightning activity in the eyewall instead of the outer rainbands. The peak VHF source rate of the entire nine-hour period occurred in the eyewall a few hours prior to landfall around 0120 UTC at about 5,000 src $(5\ \text{min})^{-1}$, with upticks in eyewall source rate persisting until around 0400 UTC (Figure 45a). The mean altitude of the eyewall's VHF sources (9.6 km) was also higher than the mean altitude of the outer rainband's VHF sources (8.1 km), yet the mean source altitude of Nicholas's rainbands was lower than that of Harvey's rainbands, hinting that the oceanic feeder band convection was less intense than the continental feeder band convection (Figure 45b). Like Harvey, the Hovmoeller diagram (Figure 45c) and plan view (Figure 45d) display a considerable spatial correlation between the highest eyewall and rainband lightning and precipitation rates during Nicholas, with some low correlations in the outer

rainbands where shallow convection dominated. There were no notable spatial movements in the largest precipitation rates with time, as rain rates exceeding 9 mm hr^{-1} remain near 29°N for the full nine hours but became lower in spatial extent as time evolved (Figure 45c).

As anticipated, the oceanic tropical convection in the outer rainbands of Hurricane Nicholas had far less spatial and temporal coverage in terms of lightning and precipitation activity compared to the continental tropical convection in the outer rainbands of Hurricane Harvey. The peak time-averaged flash extent density during the time period of focus in which the tropical cyclones impacted southeast Texas was nearly two orders of magnitude larger for Harvey than Nicholas at about 900 fl km^{-2} min^{-1} versus 14 fl km^{-2} min^{-1} (Figure 5; Figure 29), a result consistent with Cecil et al. (2002) who claimed lightning flash densities were greatest in tropical continental convection. Despite Nicholas exhibiting time-averaged rain rates of up to 36.9 mm hr^{-1} throughout the whole time period, these large rainfall amounts were quite centralized in contrast to Harvey's widespread precipitation values reaching 6.5 mm hr^{-1}. The timing of the highest lightning activity of the two tropical events conflicted greatly, as Harvey had the majority of its lightning a day after landfall on 27 August 2017 while Nicholas had most of its lightning before landfall on 14 September 2021 (Figure 6; Figure 30). The largest spatially-averaged flash rate was around 300 fl min^{-1} for Harvey and about 28 fl min^{-1} for Nicholas during their respective strongest electrically-active time periods. The VHF source behavior also demonstrated Harvey's higher lightning activity with source rates at approximately 177,472 src $(5\ min)^{-1}$ and source densities reaching 56.7 src km^{-1} $(5\ min)^{-}$

^{1}, while Nicholas had source rates reaching only 3,250 src (5 min)$^{-1}$ and source densities maxed at 1.4 src km^{-1} (5 min)$^{-1}$ (Figure 7a; Figure 31a). The maximum spatially-averaged precipitation rates during these time frames were 9 mm hr^{-1} for Harvey and 6.5 mm hr^{-1} for Nicholas, and these large rain rates occurred a few hours after the peak lightning rate and before the peak lightning rate for Hurricane Harvey and Hurricane Nicholas, respectively.

The selected case studies continued to convey microphysical disparities in lightning and precipitation within the rainbands of Harvey and Nicholas. Hurricane Harvey had an abundance of higher-altitude lightning with VHF sources exceeding 15 km in Case 1 and Case 2, while Hurricane Nicholas had a limited number of elevated sources in both case studies (Figure 7a,b; Figure 31a,b). The mean source altitudes of Case 1 and Case 2 for Harvey were 9.3 km and 9.9 km, while the mean source altitudes for the two deep convective case studies for Nicholas were only 8.0 km and 8.1 km, which was close to the mean source altitude of 7.8 km in the shallow convective Case 3 for Harvey. The characteristics of deep convection were verified further with the peak longitude-averaged rain rate of 33.2 mm hr^{-1} in Harvey spatially collocated in time with the maxima in VHF source density for Case 1 and Case 2, while a similar result was seen with Nicholas with peak longitude-averaged rain rate of 22.5 mm hr^{-1} aligned with the locations of maximum VHF source density (Figure 7c; Figure 31c). It is interesting to acknowledge that Harvey's forecast sounding profiles had considerably less MUCAPE than Nicholas's forecast sounding profiles, indicating that less instability was needed for the continental convection to produce outstanding lightning and precipitation

rates (Figure 8; Figure 14; Figure 20; Figure 32; Figure 38). However, the stationary front in the vicinity of Harvey generated sufficient lifting of moist parcels that likely supplemented the convection within the less unstable environment.

Both Harvey and Nicholas's case studies featured surges in NLDN flash rates that were associated with general increases in the heights of the VHF sources from the corresponding charge analyses, yet the flash rates and source heights for Nicholas's case studies closely resembled the lower values present in Harvey's Case 3 stratiform convection (Figure 9; Figure 15; Figure 21; Figure 33; Figure 39). Regarding the type and polarity of flashes, Harvey's case studies had values ranging from 13-37% in +CG flashes and 5-13% in -IC flashes, while Nicholas's case studies had 21-35% in +CG flashes and 7-12% in -IC flashes. Nonetheless, these ratios are less impressive for Nicholas due to its lower lightning activity compared to Harvey. The presence of flash rates with anomalous polarities was exemplified by inverted tripole charge structures contained within all of Harvey and Nicholas's rainband case studies, yet Harvey's charge layers were situated at higher heights compared to those of Nicholas (Figure 10d; Figure 11d; Figure 16d; Figure 17d; Figure 22d; Figure 23d; Figure 34d; Figure 35d; Figure 40d; Figure 41d). Finally, the intensity of Harvey's continental convection in relation to Nicholas's oceanic convection was illustrated by the dual-pol radar products. Harvey's deep convective rainbands were not only more organized than Nicholas's, but they consisted of larger Z_H values up to 55-63 dBZ, more $-Z_{DR}$ aloft and thus more VHF sources affiliated with higher lightning activity, and greater Z_{DR} and K_{DP} values (> 1.5-2 dB; > 2.5-3 deg km^{-1}) extending further past the melting level (e.g., Figure 10; Figure

11; Figure 13; Figure 16; Figure 17; Figure 19; Figure 34; Figure 35; Figure 37; Figure 40; Figure 41; Figure 43).

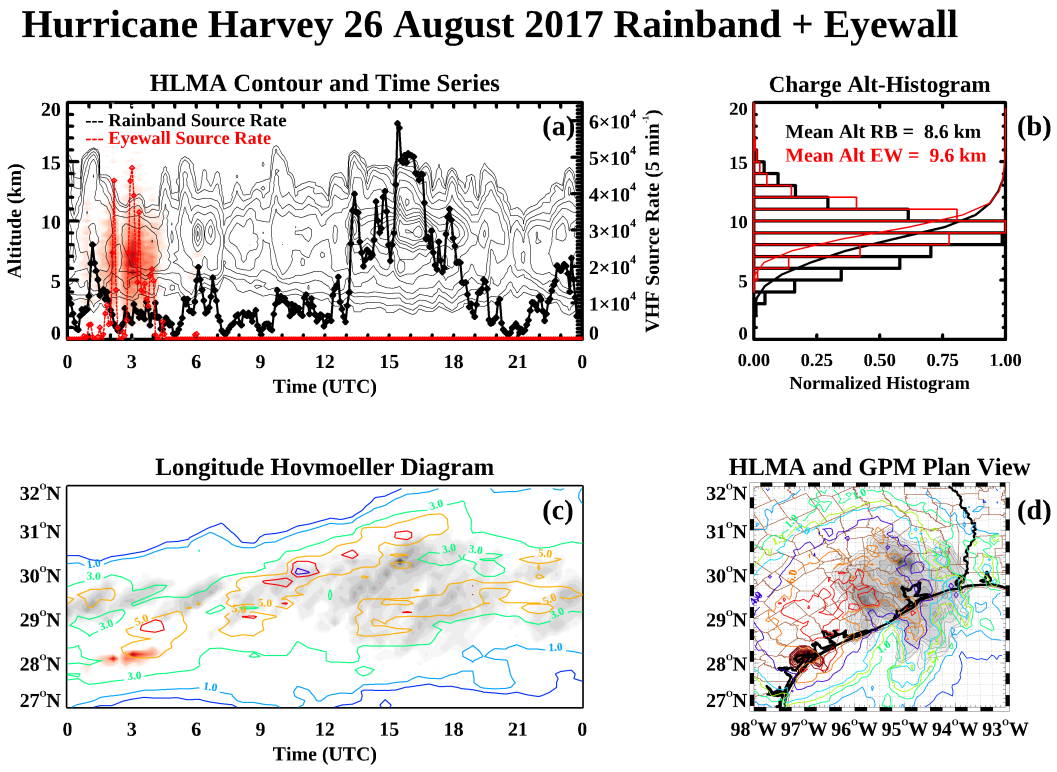

Figure 44: 26 August 2017 plots of (a) HLMA VHF outer rainband source density (black contours), VHF eyewall source density (red filled contours), VHF outer rainband source rate (black line; # [5 min^{-1}]), and VHF eyewall source rate (red line; # [5 min^{-1}]) time-altitude series, (b) charge altitude normalized histogram with mean altitude and cumulative distribution function line denoted for the outer rainbands and eyewall, (c) longitude-averaged Hovmoeller diagram of HLMA VHF outer rainband source density (black filled contours), VHF eyewall source density (red filled contours), and GPM precipitation rate (colored contours; mm hr^{-1}), (d) plan view of HLMA VHF outer rainband source density (black filled contours), VHF eyewall source density (red filled contours), and GPM precipitation rate (colored contours; mm hr^{-1}). Note that the eyewall VHF source rate was multiplied by 10,000 to allow for comparison between the outer rainband VHF source rate.

Hurricane Nicholas 0000-0900 UTC 14 September 2021

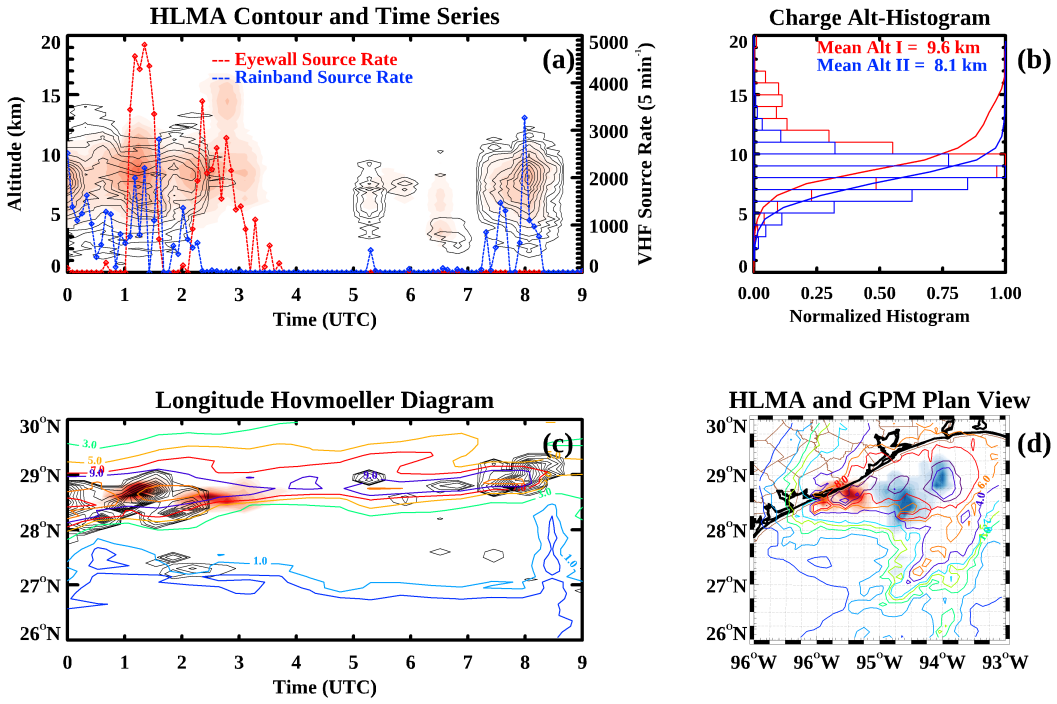

Figure 45: 0000 to 0900 UTC 14 September 2021 plots of (a) HLMA VHF outer rainband source density (black contours), VHF eyewall source density (red filled contours), VHF outer rainband source rate (blue line; # [5 min^{-1}]), and VHF eyewall source rate (red line; # [5 min^{-1}]) time-altitude series, (b) charge altitude normalized histogram with mean altitude and cumulative distribution function line denoted for the outer rainbands and eyewall, (c) longitude-averaged Hovmoeller diagram of HLMA VHF outer rainband source density (black contours), VHF eyewall source density (red filled contours), and GPM precipitation rate (colored contours; mm hr^{-1}), (d) plan view of HLMA VHF outer rainband source density (blue filled contours), VHF eyewall source density (red filled contours), and GPM precipitation rate (colored contours; mm hr^{-1}).

4. CONCLUSIONS

The lightning-precipitation microphysics within the outer rainbands of Hurricane Harvey and Hurricane Nicholas were studied using total lightning observations obtained from the HLMA synergistically with NEXRAD radar variables, GPM precipitation measurements, and environmental data. Within each tropical cyclone, case studies that exhibited significant electrical activity and rainfall yields in southeast Texas were examined for their convective tendencies. During each case study, 10-minute time windows that demonstrated remarkable lightning-precipitation behavior were further investigated for a more thorough assessment of their polarimetric radar signatures and electrical charge structures.

Trends in lightning within tropical convection can aid in determining the magnitude and evolution of a storm and thus deduce its potential for extreme precipitation, as the nature of the lightning activity allowed for the state of convection to be discerned. In general, moments that displayed more rampant lightning behavior with higher flash rates and larger VHF source densities resembled deeper convective environments, while lower lightning activity corresponded to weaker, stratiform convection. Additionally, the presence of higher-altitude lightning provided evidence that the updraft was vigorous, and surges in flash rates indicated that the storm was undergoing intensification. When deep convection is present, rainfall is observed to be intense yet shorter-lived. Conversely, shallow convection is prolonged with lower rain

rates. Therefore, the ability of lightning to infer the type of convection reveals how the precipitation will occur.

There were distinct spatial and temporal relationships between lightning and precipitation within both tropical events that affected southeast Texas. The deep convective case studies for Harvey and Nicholas had the largest lightning and precipitation regions spatially collocated overall, while the shallow case during Harvey had these lightning and rainfall maxima notably offset. The largest flash rates during Harvey occurred after landfall, which preceded the peak precipitation rates by about 6 hours. The results were opposite for Nicholas with the highest flash rates prior to landfall that lagged the maximum rainfall rate by a few hours.

As expected, the continental tropical convection within Harvey was more powerful than the oceanic tropical convection within Nicholas. Harvey exhibited greater amounts of lightning and precipitation which were widespread throughout southeast Texas, while Nicholas had lesser amounts partly due to its more centralized activity. The convection in Harvey was considerably more organized than that of the outer rainbands in Nicholas. Furthermore, the radar variables revealed the strength of Harvey's tropical convection with larger Z_H, Z_{DR}, and K_{DP} values reaching higher altitudes than Nicholas.

Although Harvey and Nicholas both underwent rapid intensification prior to landfall, there were discontinuities between these tropical systems that were illuminated through the supplemental use of total lightning information. The lightning during the tropical events was captured well by the HLMA, which enabled the electrified clouds to be analyzed in 3D space and time. However, future work should incorporate space-based

lightning detection platforms such as GLM as well for extra verification on the electrical behavior of storms. Ground-based precipitation products that have better spatial coverage than rain gauge networks should also be employed to provide an additional source of rainfall measurements. Additional tropical cyclones that contained heightened lightning and precipitation activity should be examined to verify the microphysical trends observed in this study. Moreover, the oceanic convection within Hurricane Harvey and the continental convection within Hurricane Nicholas could be studied to validate the weaker convective behavior of the oceanic outer rainbands. The aerosol-cloud interactions within anomalously-electrified clouds in the polluted environment of southeast Texas should be analyzed to gain a better understanding of the cause of inverted charge structures. More case studies involving electrified shallow convection should be examined to gain more insight on the charging mechanisms within warm clouds. Finally, 3D lightning data from LMAs can be incorporated into cell tracking and forecasting algorithms to enhance the detection of intense convection, especially within the tropical feeder bands in regions with poor radar and satellite coverage.

REFERENCES

Blake, E. S., and D. A. Zelinsky, 2018: National Hurricane Center Tropical Cyclone Report: Hurricane Harvey. *National Hurricane Center*. https://www.nhc.noaa.gov/data/tcr/AL092017_Harvey.pdf (Accessed September 30, 2022).

Blakeslee, R. J., and Coauthors, 2020: Three years of the Lightning Imaging Sensor onboard the International Space Station: Expanded global coverage and enhanced applications. *Journal of Geophysical Research: Atmospheres*, **125**, doi:10.1029/2020jd032918.

Borque, P., L. Vidal, M. Rugna, T. J. Lang, M. G. Nicora, and S. W. Nesbitt, 2020: Distinctive signals in 1-min observations of overshooting tops and lightning activity in a severe supercell thunderstorm. *Journal of Geophysical Research: Atmospheres*, **125**, doi:10.1029/2020jd032856.

Bowman, K. P., and C. R. Homeyer, 2017: Algorithm description document for Version 3.1 of the three-dimensional Gridded NEXRAD WSR-88D Radar (GridRad) dataset. *GridRad*. http://gridrad.org/pdf/GridRad-v4.2-Algorithm-Description.pdf (Accessed July 14, 2022).

Brauer, N. S., J. B. Basara, C. R. Homeyer, G. M. McFarquhar, and P. E. Kirstetter, 2020: Quantifying precipitation efficiency and drivers of excessive precipitation

in post-landfall Hurricane Harvey. *Journal of Hydrometeorology*, **21**, 433–452, doi:10.1175/jhm-d-19-0192.1.

Bruning, E. C., 2013: Streamed clustering of lightning mapping data in Python using sklearn. *Proceedings 12th Python in Science Conference (SciPy)*, Vol. 2, Austin, Texas.

Bruning, E. C., and Coauthors, 2019: Meteorological imagery for the Geostationary Lightning Mapper. *Journal of Geophysical Research: Atmospheres*, **124**, 14285–14309, doi:10.1029/2019jd030874.

Calhoun, K. M., D. R. MacGorman, C. L. Ziegler, and M. I. Biggerstaff, 2013: Evolution of lightning activity and storm charge relative to dual-doppler analysis of a high-precipitation supercell storm. *Monthly Weather Review*, **141**, 2199–2223, doi:10.1175/mwr-d-12-00258.1.

Carey, L. D., and S. A. Rutledge, 2000: The relationship between precipitation and lightning in tropical island convection: A C-band polarimetric radar study. *Monthly Weather Review*, **128**, 2687–2710, doi:10.1175/1520-0493(2000)128<2687:trbpal>2.0.co;2.

Carey, L. D., and S. A. Rutledge, 2003: Characteristics of cloud-to-ground lightning in severe and nonsevere storms over the central United States from 1989–1998. *Journal of Geophysical Research*, **108**, doi:10.1029/2002jd002951.

Carr, N., P. E. Kirstetter, J. J. Gourley, and Y. Hong, 2017: Polarimetric signatures of midlatitude warm-rain precipitation events. *Journal of Applied Meteorology and Climatology*, **56**, 697–711, doi:10.1175/jamc-d-16-0164.1.

Cecil, D. J., E. J. Zipser, and S. W. Nesbitt, 2002: Reflectivity, ice scattering, and lightning characteristics of hurricane eyewalls and rainbands. Part I: Quantitative description. *Monthly Weather Review*, **130**, 769–784, doi:10.1175/1520-0493(2002)130<0769:risalc>2.0.co;2.

Chen, S. S., J. A. Knaff, and F. D. Marks, 2006: Effects of vertical wind shear and storm motion on tropical cyclone rainfall asymmetries deduced from TRMM. *Monthly Weather Review*, **134**, 3190–3208, doi:10.1175/mwr3245.1.

Chmielewski, V. C., and E. C. Bruning, 2016: Lightning mapping array flash detection performance with variable receiver thresholds. *Journal of Geophysical Research: Atmospheres*, **121**, 8600–8614, doi:10.1002/2016jd025159.

Chmielewski, V. C., E. C. Bruning, and B. C. Ancell, 2018: Variations of thunderstorm charge structures in West Texas on 4 June 2012. *Journal of Geophysical Research: Atmospheres*, **123**, 9502–9523, doi:10.1029/2018jd029006.

Corbosiero, K. L., and J. Molinari, 2002: The effects of vertical wind shear on the distribution of convection in tropical cyclones. *Monthly Weather Review*, **130**, 2110–2123, doi:10.1175/1520-0493(2002)130<2110:teovws>2.0.co;2.

Corbosiero, K. L., and J. Molinari, 2003: The relationship between storm motion, vertical wind shear, and convective asymmetries in tropical cyclones. *Journal of the Atmospheric Sciences*, **60**, 366–376, doi:10.1175/1520-0469(2003)060<0366:trbsmv>2.0.co;2.

Crum, T. D., and R. L. Alberty, 1993: The WSR-88D and the WSR-88D Operational Support Facility. *Bulletin of the American Meteorological Society*, **74**, 1669–1687, doi:10.1175/1520-0477(1993)074<1669:twatwo>2.0.co;2.

Cullen, M. R., 2013: The Houston Lightning Mapping Array: Network installation and preliminary analysis. *Master's thesis*. Texas A&M University. Available electronically from https://oaktrust.library.tamu.edu/handle/1969.1/151109.

Cummins, K. L., and M. J. Murphy, 2009: An overview of lightning locating systems: History, techniques, and data uses, with an in-depth look at the U.S. NLDN. *IEEE Transactions on Electromagnetic Compatibility*, **51**, 499–518, doi:10.1109/temc.2009.2023450.

DeHart, J. C., and M. M. Bell, 2020: A comparison of the polarimetric radar characteristics of heavy rainfall from Hurricanes Harvey (2017) and Florence (2018). *Journal of Geophysical Research: Atmospheres*, **125**, doi:10.1029/2019jd032212.

DeMaria, M., R. T. DeMaria, J. A. Knaff, and D. Molenar, 2012: Tropical cyclone lightning and rapid intensity change. *Monthly Weather Review*, **140**, 1828–1842, doi:10.1175/mwr-d-11-00236.1.

Didlake, A. C., and M. R. Kumjian, 2017: Examining polarimetric radar observations of bulk microphysical structures and their relation to vortex kinematics in Hurricane Arthur (2014). *Monthly Weather Review*, **145**, 4521–4541, doi:10.1175/mwr-d-17-0035.1.

DiGangi, E. A., D. R. MacGorman, C. L. Ziegler, D. Betten, M. Biggerstaff, M. Bowlan, and C. K. Potvin, 2016: An overview of the 29 May 2012 Kingfisher supercell during DC3. *Journal of Geophysical Research: Atmospheres*, **121**, doi:10.1002/2016jd025690.

DiGangi, E., J. Lapierre, M. Stock, M. Hoekzema, and B. Cunha, 2022: Analyzing lightning characteristics in central and southern South America. *Electric Power Systems Research*, **213**, 108704, doi:10.1016/j.epsr.2022.108704.

Fierro, A. O., E. R. Mansell, C. L. Ziegler, and D. R. MacGorman, 2015: Explicitly simulated electrification and lightning within a tropical cyclone based on the environment of Hurricane Isaac (2012). *Journal of the Atmospheric Sciences*, **72**, 4167–4193, doi:10.1175/jas-d-14-0374.1.

Fridlind, A. M., and Coauthors, 2019: Use of polarimetric radar measurements to constrain simulated convective cell evolution: A pilot study with lagrangian tracking. *Atmospheric Measurement Techniques*, **12**, 2979–3000, doi:10.5194/amt-12-2979-2019.

Fuchs, B. R., and S. A. Rutledge, 2018: Investigation of lightning flash locations in isolated convection using LMA observations. *Journal of Geophysical Research: Atmospheres*, **123**, 6158–6174, doi:10.1002/2017jd027569.

Fuchs, B. R., and Coauthors, 2015: Environmental controls on storm intensity and charge structure in multiple regions of the continental United States. *Journal of Geophysical Research: Atmospheres*, **120**, 6575–6596, doi:10.1002/2015jd023271.

Fuchs, B. R., E. C. Bruning, S. A. Rutledge, L. D. Carey, P. R. Krehbiel, and W. Rison, 2016: Climatological analyses of LMA data with an open-source lightning flash-clustering algorithm. *Journal of Geophysical Research: Atmospheres*, **121**, 8625–8648, doi:10.1002/2015jd024663.

Habibi, H., R. Awal, A. Fares, and M. Temimi, 2021: Performance of Multi-Radar Multi-Sensor (MRMS) product in monitoring precipitation under extreme events in Harris County, Texas. *Journal of Hydrology*, **598**, 126385, doi:10.1016/j.jhydrol.2021.126385.

Homeyer, C. R., and Coauthors, 2021: Polarimetric signatures in landfalling tropical cyclones. *Monthly Weather Review*, **149**, 131–154, doi:10.1175/mwr-d-20-0111.1.

Hu, J., D. Rosenfeld, A. Ryzhkov, and P. Zhang, 2020: Synergetic use of the WSR-88D radars, GOES-R satellites, and lightning networks to study microphysical characteristics of hurricanes. *Journal of Applied Meteorology and Climatology*, **59**, 1051–1068, doi:10.1175/jamc-d-19-0122.1.

Kasemir, H. W., 1960: A contribution to the electrostatic theory of a lightning discharge. *Journal of Geophysical Research*, **65**, 1873–1878, doi:10.1029/jz065i007p01873.

Koshak, W. J., E. P. Krider, N. Murray, and D. J. Boccippio, 2007: Lightning charge retrievals: Dimensional reduction, LDAR constraints, and a first comparison with LIS satellite data. *Journal of Atmospheric and Oceanic Technology*, **24**, 1817–1838, doi:10.1175/jtech2089.1.

Kumjian, M., 2013: Principles and applications of dual-polarization weather radar part I: Description of the polarimetric radar variables. *Journal of Operational Meteorology*, **1**, 226–242, doi:10.15191/nwajom.2013.0119.

Landsea, C. W., and J. L. Franklin, 2013: Atlantic hurricane database uncertainty and presentation of a new database format. *Monthly Weather Review*, **141**, 3576–3592, doi:10.1175/mwr-d-12-00254.1.

Latto, A. S., and R. Berg, 2022: National Hurricane Center Tropical Cyclone Report: Hurricane Nicholas. *National Hurricane Center*. https://www.nhc.noaa.gov/data/tcr/AL142021_Nicholas.pdf (Accessed October 5, 2022).

Logan, T., 2018: Anomalous lightning behavior during the 26–27 August 2007 northern Great Plains severe weather event. *Journal of Geophysical Research: Atmospheres*, **123**, 1771–1784, doi:10.1002/2017jd027750.

Logan, T., 2021: An analysis of the performance of the Houston Lightning Mapping Array during an intense period of convection during Tropical Storm Harvey. *Journal of Geophysical Research: Atmospheres*, **126**, doi:10.1029/2020jd033270.

MacGorman, D. R., W. D. Rust, P. Krehbiel, W. Rison, E. Bruning, and K. Wiens, 2005: The electrical structure of two supercell storms during STEPS. *Monthly Weather Review*, **133**, 2583–2607, doi:10.1175/mwr2994.1.

Martinaitis, S. M., S. B. Cocks, A. P. Osborne, M. J. Simpson, L. Tang, J. Zhang, and K. W. Howard, 2021: The historic rainfalls of Hurricanes Harvey and Florence: A perspective from the Multi-Radar Multi-Sensor system. *Journal of Hydrometeorology*, **22**, 721–738, doi:10.1175/jhm-d-20-0199.1.

Mazur, V., and L. H. Ruhnke, 1993: Common physical processes in natural and artificially triggered lightning. *Journal of Geophysical Research*, **98**, 12913, doi:10.1029/93jd00626.

Medina, B. L., L. D. Carey, T. J. Lang, P. M. Bitzer, W. Deierling, and Y. Zhu, 2021: Characterizing charge structure in central Argentina thunderstorms during RELAMPAGO utilizing a new charge layer polarity identification method. *Earth and Space Science*, **8**, doi:10.1029/2021ea001803.

Orville, R. E., and Coauthors, 2001: Enhancement of cloud-to-ground lightning over Houston, Texas. *Geophysical Research Letters*, **28**, 2597–2600, doi:10.1029/2001gl012990.

Pan, B., Y. Wang, T. Logan, J. S. Hsieh, J. H. Jiang, Y. Li, and R. Zhang, 2020: Determinant role of aerosols from industrial sources in Hurricane Harvey's catastrophe. *Geophysical Research Letters*, **47**, doi:10.1029/2020gl090014.

Petersen, W. A., and S. A. Rutledge, 2001: Regional variability in tropical convection: Observations from TRMM. *Journal of Climate*, **14**, 3566–3586, doi:10.1175/1520-0442(2001)014<3566:rvitco>2.0.co;2.

Qu, Z., and Coauthors, 2022: The impacts of secondary ice production on microphysics and dynamics in tropical convection. *Atmospheric Chemistry and Physics*, **22**, 12287–12310, doi:10.5194/acp-22-12287-2022.

Rakov, V. A., and M. A. Uman, 2003: Chapter 5: Positive and bipolar lightning discharges to ground. *Lightning: Physics and Effects*, Cambridge University Press, Cambridge, New York, 214–234.

Ren, T., A. D. Rapp, S. L. Nasiri, J. R. Mecikalski, and J. Apke, 2018: Is the awareness of the aerosol state useful in predicting enhanced lightning for lightning-producing storms over northern Alabama? *Journal of Applied Meteorology and Climatology*, **57**, 1663–1681, doi:10.1175/jamc-d-17-0182.1.

Rison, W., R. J. Thomas, P. R. Krehbiel, T. Hamlin, and J. Harlin, 1999: A GPS-based three-dimensional lightning mapping system: Initial observations in central New Mexico. *Geophysical Research Letters*, **26**, 3573–3576, doi:10.1029/1999gl010856.

Rogers, R., S. Chen, J. Tenerelli, and H. Willoughby, 2003: A numerical study of the impact of vertical shear on the distribution of rainfall in Hurricane Bonnie (1998). *Monthly Weather Review*, **131**, 1577–1599, doi:10.1175//2546.1.

Rudlosky, S. D., M. J. Peterson, and D. T. Kahn, 2017: GLD360 performance relative to TRMM LIS. *Journal of Atmospheric and Oceanic Technology*, **34**, 1307–1322, doi:10.1175/jtech-d-16-0243.1.

Saunders, C. P., 1993: A review of thunderstorm electrification processes. *Journal of Applied Meteorology*, **32**, 642–655, doi:10.1175/1520-0450(1993)032<0642:arotep>2.0.co;2.

Schultz, C. J., W. A. Petersen, and L. D. Carey, 2009: Preliminary development and evaluation of lightning jump algorithms for the real-time detection of severe weather. *Journal of Applied Meteorology and Climatology*, **48**, 2543–2563, doi:10.1175/2009jamc2237.1.

Schultz, C. J., L. D. Carey, E. V. Schultz, and R. J. Blakeslee, 2015: Insight into the kinematic and microphysical processes that control lightning jumps. *Weather and Forecasting*, **30**, 1591–1621, doi:10.1175/waf-d-14-00147.1.

Sharma, M., R. L. Tanamachi, E. C. Bruning, and K. M. Calhoun, 2021: Polarimetric and electrical structure of the 19 May 2013 Edmond–Carney, Oklahoma, tornadic supercell. *Monthly Weather Review*, **149**, 2049–2078, doi:10.1175/mwr-d-20-0280.1.

Skofronick-Jackson, G., D. Kirschbaum, W. Petersen, G. Huffman, C. Kidd, E. Stocker, and R. Kakar, 2018: The Global Precipitation Measurement (GPM) mission's scientific achievements and societal contributions: Reviewing four years of

advanced rain and snow observations. *Quarterly Journal of the Royal Meteorological Society*, **144**, 27–48, doi:10.1002/qj.3313.

Solimine, S. L., L. Zhou, A. Raghavendra, and Y. Cai, 2022: Relationships between intense convection, lightning, and rainfall over the interior Congo Basin using TRMM data. *Atmospheric Research*, **273**, 106164, doi:10.1016/j.atmosres.2022.106164.

Solorzano, N., J. Thomas, and C. Bracy, 2018: Monitoring tropical cyclones with lightning and satellite data. *Eos*, **99**, doi:10.1029/2018eo092439.

Stano, G., C. Schultz, L. Carey, D. MacGorman, and K. Calhoun, 2014: Total lightning observations and tools for the 20 May 2013 Moore, Oklahoma, tornadic supercell. *Journal of Operational Meteorology*, **2**, 71–88, doi:10.15191/nwajom.2014.0207.

Stevenson, S. N., K. L. Corbosiero, and J. Molinari, 2014: The convective evolution and rapid intensification of Hurricane Earl (2010). *Monthly Weather Review*, **142**, 4364–4380, doi:10.1175/mwr-d-14-00078.1.

Stevenson, S. N., K. L. Corbosiero, and S. F. Abarca, 2015: Lightning in eastern North Pacific tropical cyclones: A comparison to the North Atlantic. *Monthly Weather Review*, **144**, 225–239, doi:10.1175/mwr-d-15-0276.1.

Stolz, D. C., S. Businger, and A. Terpstra, 2014: Refining the relationship between lightning and convective rainfall over the ocean. *Journal of Geophysical Research: Atmospheres*, **119**, 964–981, doi:10.1002/2012jd018819.

Stolzenburg, M., and T. C. Marshall, 2008: Charge structure and dynamics in thunderstorms. *Space Science Reviews*, **137**, 355–372, doi:10.1007/s11214-008-9338-z.

Takahashi, T., 1978: Riming electrification as a charge generation mechanism in thunderstorms. *Journal of the Atmospheric Sciences*, **35**, 1536–1548, doi:10.1175/1520-0469(1978)035<1536:reaacg>2.0.co;2.

Tapia, A., J. A. Smith, and M. Dixon, 1998: Estimation of convective rainfall from lightning observations. *Journal of Applied Meteorology*, **37**, 1497–1509, doi:10.1175/1520-0450(1998)037<1497:eocrfl>2.0.co;2.

Thomas, R. J., P. R. Krehbiel, W. Rison, S. J. Hunyady, W. P. Winn, T. Hamlin, and J. Harlin, 2004: Accuracy of the Lightning Mapping Array. *Journal of Geophysical Research*, **109**, doi:10.1029/2004jd004549.

Tian, J., X. Dong, B. Xi, and Z. Feng, 2020: Characteristics of ice cloud–precipitation of warm season mesoscale convective systems over the Great Plains. *Journal of Hydrometeorology*, **21**, 317–334, doi:10.1175/jhm-d-19-0176.1.

van Lier-Walqui, M., and Coauthors, 2016: On polarimetric radar signatures of deep convection for model evaluation: Columns of specific differential phase observed

during MC3E*. *Monthly Weather Review*, **144**, 737–758, doi:10.1175/mwr-d-15-0100.1.

Wiens, K. C., S. A. Rutledge, and S. A. Tessendorf, 2005: The 29 June 2000 supercell observed during STEPS part II: Lightning and charge structure. *Journal of the Atmospheric Sciences*, **62**, 4151–4177, doi:10.1175/jas3615.1.

Williams, E. R., 1985: Large-scale charge separation in thunderclouds. *Journal of Geophysical Research*, **90**, 6013, doi:10.1029/jd090id04p06013.

Williams, E. R., R. Zhang, and J. Rydock, 1991: Mixed-phase microphysics and cloud electrification. *Journal of the Atmospheric Sciences*, **48**, 2195–2203, doi:10.1175/1520-0469(1991)048<2195:mpmace>2.0.co;2.

Williams, E., and Coauthors, 1999: The behavior of total lightning activity in severe Florida thunderstorms. *Atmospheric Research*, **51**, 245–265, doi:10.1016/s0169-8095(99)00011-3.

Xu, W., R. F. Adler, and N.-Y. Wang, 2013: Improving geostationary satellite rainfall estimates using lightning observations: Underlying lightning–rainfall–cloud relationships. *Journal of Applied Meteorology and Climatology*, **52**, 213–229, doi:10.1175/jamc-d-12-040.1.

Xu, W., S. A. Rutledge, and W. Zhang, 2017: Relationships between total lightning, deep convection, and tropical cyclone intensity change. *Journal of Geophysical Research: Atmospheres*, **122**, 7047–7063, doi:10.1002/2017jd027072.

Yang, L., J. Smith, M. Liu, and M. L. Baeck, 2019: Extreme rainfall from Hurricane Harvey (2017): Empirical intercomparisons of WRF simulations and polarimetric radar fields. *Atmospheric Research*, **223**, 114–131, doi:10.1016/j.atmosres.2019.03.004.

Zheng, D., D. Wang, Y. Zhang, T. Wu, and N. Takagi, 2019: Charge regions indicated by LMA lightning flashes in Hokuriku's winter thunderstorms. *Journal of Geophysical Research: Atmospheres*, **124**, 7179–7206, doi:10.1029/2018jd030060.

APPENDIX A:

PERFORMANCE OF THE GPM IMERG PRODUCT COMPARED TO THE HCFCD RAIN GAUGES DURING HURRICANE HARVEY

The precipitation measurements collected by the GPM IMERG product and the HCFCD rain gauges during Hurricane Harvey were compared spatially and temporally. Figure 46 shows the plan view of Harris County with the total rainfall accumulation (mm) contoured from both the GPM and HCFCD datasets from 0000 UTC 25 August 2017 to 0000 UTC 30 August 2017. The GPM and HCFCD observations generally agreed spatially with the largest precipitation values located in the southeast region of Harris County. However, the HCFCD rain gauges measured higher rainfall accumulations than the GPM IMERG product.

Figure 47 shows the time series of GPM and HCFCD rain gauge precipitation rate (mm hr^{-1}) in Harris County for the five-day period during Hurricane Harvey with the associated linear regression model for the GPM and HCFCD datasets during this period plotted to the side. The HCFCD data were averaged spatially and interpolated to have a 30-min temporal resolution to allow for the direct comparison to the spatially-averaged GPM data. Note that the HCFCD observations were also converted from inches of accumulation (per 15 minutes) to precipitation rate in mm hr^{-1} by multiplying each measurement by 25.4 and 4. The spikes in rain rate for both datasets appeared to agree temporally with the HCFCD rain gauges exhibiting higher peak rain rates overall approaching 40 mm hr^{-1} (Figure 47a). Indeed, the linear regression model depicts a strong positive correlation between the GPM and HCFCD precipitation rates (Figure

47b). Nonetheless, the HCFCD rain gauge data was biased towards higher rain rates while the GPM data captured all rainfall intensities well. This result likely stems from the finding that tipping bucket rain gauges suffer from measurement issues such as wind undercatch that cause underestimations in light precipitation, as the smaller drop-size distributions in tropical warm-rain processes are more prone to wind undercatch (Habibi et al. 2021; Martinaitis et al. 2021).

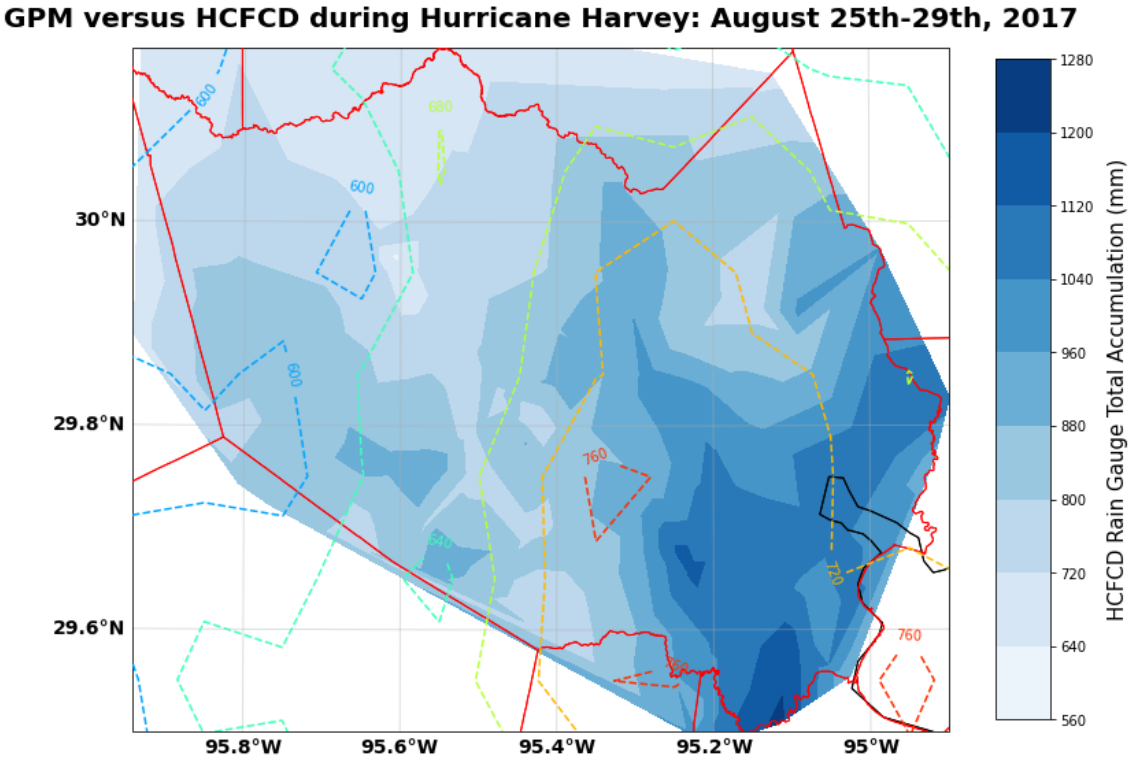

Figure 46: Plan view of Harris County with GPM accumulated map product (colored contours; mm) and HCFCD rain gauge total accumulation (blue filled contours; mm) for 0000 UTC 25 August 2017 to 0000 UTC 30 August 2017 during Hurricane Harvey. The HCFCD measurements were converted from inches to millimeters by multiplying each observation by 25.4. The GPM data were confined to Harris County by using the minimum and maximum latitude/longitude values of the HCFCD rain gauges as the spatial domain box. The gaps in the HCFCD rain gauge data were eliminated by interpolation through the use of a triangulation function.

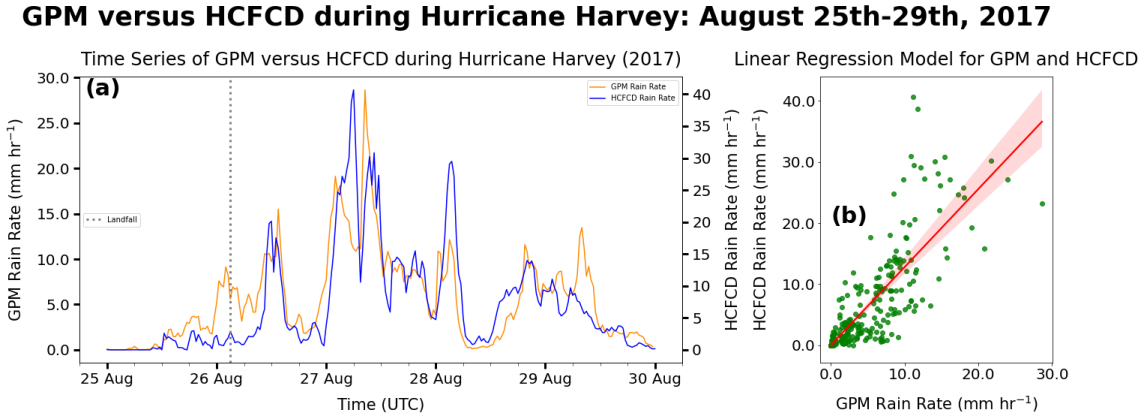

Figure 47: (a) Time series of GPM precipitation rate (mm hr^{-1}) denoted by the orange line and HCFCD rain gauge precipitation rate (mm hr^{-1}) denoted by the blue line from 0000 UTC 25 August 2017 to 0000 UTC 30 August 2017 during Hurricane Harvey, (b) linear regression model (y~x) for GPM and HCFCD precipitation rate during the five-day period with the associated regression line (red line) and 95% confidence interval (red shading) shown. The time of landfall is denoted on (a) with the dotted vertical gray line. The HCFCD data were averaged spatially, interpolated to have a 30-min temporal resolution, and converted from an accumulation (in) to a rain rate (mm hr^{-1}) through multiplication to allow for the direct comparison to the GPM data.